博士論文

濃厚シリケート溶液から出発する
ゼオライト合成法の開発と
新規ゼオライト合成

(Development of synthetic method starting from concentrated silicate solution and synthesis of novel zeolite)

横浜国立大学大学院
工学府

中澤 直人
Nakazawa Naoto

2019年・3月

Objective

Objective in this work is to synthesize novel zeolites by utilizing microscopic structural similarities between starting materials and aimed products. In addition, the new synthesis route via concentrated silicate solution is proposed as an efficient way to withdraw the potentials of organic structure-directing agents (OSDAs). Although crystallization kinetics of zeolites still remain unveiled, these novel synthesis techniques should enable to take shortcuts to obtain novel zeolites with desired framework structures and compositions.

Chapter 1 introduces an overview of zeolite science and backgrounds of this study. Although there are various factors that determine adsorptive and catalytic properties of zeolites, it is generally difficult to control them as freely as possible by the simple hydrothermal synthesis method with tedious try and error. Many attempts and successful examples that have contributed to develop a variety of zeolite syntheses are reviewed.

Chapter 2 shows the hydrothermal syntheses of novel ***STO**-type zeolites (YNU-4) by using ***BEA**- or **CON**-type zeolites as seed crystals. The OSDA is the same as that for the synthesis of borosilicate **CON**-type zeolite (CIT-1). The structural similarities were clearly observed between seeds and products. ***STO**-type zeolites did not crystalize without any seeds, which indicated the crystallization was promoted by the presence of seed crystals. The nucleation and crystal growth rates were successfully changed by controlling the sizes of seed crystals, which means the crystal size control of ***STO**-type zeolites is possible.

Chapter 3 presents high-silica SSZ-39 nanocrystals obtained by direct hydrothermal synthesis using piperidine-derivated OSDA which is readily available. The novel synthesis technique includes the preparation of highly concentrated silicate solution and the subsequent manual mixing of **FAU**-type zeolites which are aluminum sources. As a result, high-silica SSZ-39 with Si/Al as high as 16 is directly synthesized. This novel small-pore zeolite material is a promising catalyst for selective catalytic reduction (SCR) of NOx. In addition, fault-free **GME**-type zeolites are also obtained by using the same OSDA, so the synthesis boundary and the possible utility of **GME** are also discussed.

Chapter 4 shows the hydrothermal synthesis of an novel **AFX**-type zeolite. The combination of **FAU**-type zeolites with a bulky and hydrophobic organic structure-directing agent (OSDA) enabled the crystallization of the **AFX**-type zeolite with Si/Al molar ratios in the range between 6 to 9, where conventional techniques have never achieved. More interestingly, the particles possess clearly dihexahedral topology, indicating high crystallinity. Crystallization kinetics were also examined by XRD and FE-SEM and the role of the **FAU**-type zeolite as a precursor for **AFX** is unveiled.

Chapter 5 describes the synthesis of a novel large-pore aluminosilicate zeolite with new framework structure, named YNU-5. The OSDA is dimethyldipropylammonium which is commercially available. The framework Si/Al composition is around 8, but it is flexibly tuned by post acid-treatment

between 9 and ca. 300. YNU-5 synthesis utilizes the method starting from concentrated silicate solution, which is introduced in Chapter 3. Interestingly, SiO_2/H_2O ratios in the syntheses mixtures drastically affect the final product, indicating that the concentration of dissolved silicate species determines the degree of hydrophobic interaction between OSDAs and silicates. Unlike the synthesis of SSZ-39 using rigid piperidine-derivated OSDA, YNU-5 crystallize in the presence of flexible Me_2-Pr_2N^+. The relatively poor fitting between the OSDA and the zeolite results in so many completing phases and narrow synthesis window.

Contents

Chapter One

Introduction of zeolite science

1.1 What is zeolite?

Zeolites are crystalline microporous aluminosilicates consisting corner sharing TO_4 tetrahedra, where T is Si or Al atom (Figure 1). There are tremendous applications in separation, adsorption and catalysis fields. Si, Al and O elements that construct zeolites are highly abundant on earth, and there is no fear of shortages of the source materials. Besides, zeolites can be synthesized in inexpensive ways since they usually do not require expensive source materials such as rare earth. Therefore they are highly important materials in terms of green chemistry.

To date, there are various kinds of zeolites and they are often categorized in terms of framework types, compositions and particle sizes. The framework types which determine dimensions and diameters of pores are important to understand microscopic and macroscopic properties of the zeolites. There are a growing number of zeolite frameworks and 239 different zeolite framework type codes (FTCs) have been approved by International Zeolite Association (IZA) until December in 2018.[1)]

Micropores of zeolites are often described as the least number of oxygen atoms surrounding the pore, e.g. 8-ring (8R), 10-ring (10R) and 12-ring (12R) (Figure 2). Generally, "small pore zeolites" have 8-ring channels with approximately 0.30−0.40 nm in diameter, "medium pore zeolites" have 10-ring channels with roughly 0.40−0.55 nm in diameter, and "large pore zeolites" have 12-ring channels with 0.55−0.80 nm in diameter[2)]. In addition, the pores often intersect each other, forming multidimensional channel system. Zeolites possessing 2-dimensional and 3-dimensional channel system take advantage of fewer diffusion limitations of molecules inside the pores. On the other hand, 1-dimensional zeolites with no channel intersection are expected to show excellent shape-selectivity in catalytic reactions.

Aluminum atoms in zeolite frameworks have quite important roles in the industrial applications. Figure 1.3 showed the chemical structure around an Al atom in a zeolite framework. The colored area schematically represents where the anionic charge exists. Although the center of the anionic charge is the Al atom, the charge actually exists on the neighbor 4 oxygen atoms, which is explained by the difference of electronegativity between Al and O atoms. A counter cation always exists near an anionic Al site and a series of counter cations gave a variety of applications of zeolites. For example, the H^+-type zeolites show extremely strong acidity and are mainly used to produce industrially important hydrocarbons as solid acid catalysts. For example, fluid catalytic cracking (FCC)[3−9)], reforming of naphtha[10−13)] and methanol or dimethyl ether-to-olefin (MTO or DTO) reaction.[14−16)] In the case of alkaline cation such as Na^+ and K^+, the zeolites are applied as adsorbents, ion exchange materials, molecular sieves and so on. Cu^{2+} and Fe^{2+}-type zeolites have recently been of great interest due to the

utilizations for emission controls of diesel engines.[17−19)]

1.2 Synthesis of zeolites

Zeolites syntheses historically started from conditions with high temperature and high pressure by mimicking the natural conditions where zeolites were produced. Hydrothermal synthesis is conventional but well-established and important method until today. Gas phase or solid phase syntheses were also historically investigated.[20)]

In 1961 the hydrothermal synthesis using tetramethylammonium (TMA) was reported.[21)] Until now many kinds of OSDAs were used and a variety of synthetic new zeolites were discovered. Due to their low charge density, the use of OSDA successfully produced high-silica materials which is not available from natural products. The increasing proportion of SiO_4 tetrahedra in framework resulted in increasing thermal stability, which pioneered the utilization of zeolites as solid-acid catalysts around 600°C. Relatively mild conditions were needed to prevent the decomposition of OSDA in alkaline conditions. The fact that the use of OSDAs was limited in mild hydrothermal syntheses at lower than 200℃ increased the significant importance of hydrothermal syntheses.

Recently some of the studies attempted the deviation from conventional hydrothermal syntheses to obtain novel zeolites. “Dry-gel conversion (DGC)” techniques are carried out in almost solid-phase in the presence of water vapor. It is interesting that the dry-gel often contains OSDAs unlike conventional solid-state reaction. The DGC often accompanies with decomposition of a part of OSDAs. One of the successful example of DGC is the synthesis of pure-silica **MSE**-type zeolite (YNU-2).[23)] YNU-2 did not crystalize in hydrothermal conditions and has a well-crystalline but defect-rich structure. Some of other novel synthesis techniques using organic solvent[24)] or ionic liquid[25)] are also reported.

Now we focuses on the hydrothermal synthesis technique. Aluminosilicate is generally soluble in alkaline aqueous solution and hydrofluoric acid. Synthesis of zeolites is composed of two parts. The first is dissolution of silica and alumina to achieve supersaturation. The second is crystallization of a zeolite under hydrothermal conditions.

Figure 1.4 shows scheme of the typical zeolite synthesis. First, alkaline aqueous solution is prepared with desired composition. In addition to typical alkaline sources such as NaOH and KOH, quaternary ammonium hydroxide is widely used to crystallize the aimed zeolite. This organic is referred to “organic structure-directing agent (OSDA)” and the major role of OSDAs is to template the micropores of zeolites. Second, silica and alumina sources are dissolved into the solution and the whole mixture is stirred for several hours at room temperature, resulting white suspension. The mixture is transferred into an autoclave, and hydrothermally treated at high temperature above 100 °C for several days. Finally, the solid product is recovered by filtration or centrifugation.

Zeolite synthesis is often complicated because there are many factors which determine the final

product such as concentration of alkali, types of silica and alumina sources, crystallization temperature and crystallization period. To predict the final product is extremely difficult since crystallization mechanisms of zeolites are not fully understood to date mainly because zeolites have both ionic and covalent characters. Various recipes to obtain zeolites with desired framework, composition and particle sizes are therefore highly in demand for industrial utilizations.

Typical silica sources are amorphous silica (fumed silica, precipitated silica and colloidal silica), dissoluted silicate (sodium silicate, potassium silicate and tetramethylammonium silicate) and tetraalkoxysilane (tetraethoxysilane). Typical aluminum sources are alumina, aluminum hydroxide (crystalline or amorphous), aluminum hydroxide oxide (boehmite), aluminum nitrate hydrate and aluminum sulfate.

Longer aging period generally gives higher yield, shorter crystallization period and higher purity. Dissolution of silica into alkaline solution is a chemical process rather than a physical process. Hydrolysis from oxide surface, dissolution of simple silicate species such as $Si(OH)_4$ and polymerization of such species in homogeneous liquid phase to form precursors of a zeolite. To achieve homogeneity of suspension (although suspension is not homogeneous system) is quite important for the successful zeolite synthesis. For example, the prolonged aging period was reported to improve product yield in the synthesis of zeolite Y.[26)]

A content of Al in reaction mixtures is also often a determining factor for the successful synthesis. Aluminum incorporation into silicate or aluminosilicate species generally makes them more hydrophilic since $Al(OSi)_4$ tetrahedral units have anionic charges. This tendency is not limited to zeolites but also amorphous solids and polymeric aluminosilicate anions present in the reaction mixture. Al-rich aluminosilicate generally favors hydrophilic (high charge density) counter cations such as Na^+ and K^+. On the other hand, aluminosilicate with relatively low Al contents favors hydrophobic (low charge density) counter cations such as Me_4N^+, Et_4N^+ and many other quaternary ammonium. This tendency of favored cations results in the difference in crystallized phases. For example, the synthetic system using 1,1,3,5-tetramethylpiperidinium is known to give SSZ-39 (**AEI**) in a mixture with input Si/Al = 15, ZSM-5/11 (**MFI/MEL**) in a mixture with input Si/Al = 35 and ZSM-12 (**MTW**) with input Si/Al > 150.[27)] Generally zeolite phases which crystallize in high-silica conditions tend to possess 5-rings.

High synthetic temperature above 100 °C is generally required to promote spontaneous nucleation. On the other hand, crystallization of impurities occurs at too high temperature. Especially when using OSDAs, too high temperature often leads to crystallize undesirable products. For example, synthesis of MCM-68 (**MSE**), for example, required thermal conditions lower than 160 °C. High temperature conditions led to the formation of an impurity (ZSM-12).[28)] Another disadvantage of the high-tem-

perature conditions is that the degradation of OSDA cations often occurs at high temperature. Quaternary ammonium is generally unstable in alkaline conditions although its stability is not so problematic since the dissolved silicates generally make pH of a synthesis system much lower than 14 (approximately 9−11). For example, crystallization of the faulted gmelinite was only achieved at temperature lower than 100 °C in the presence of a polymeric OSDA because the OSDA is especially unstable compared to other monomeric OSDAs.[29)]

1.3 Intergrowth of zeolitic materials

Zeolites sometimes consist of several crystalline polymorphs. Highly complicated intergrowth structures of zeolites often make it difficult to identify correct microstructures and to discuss from the microscopic points of view. Three of the most famous examples are ABC-6 family, **FAU**/**EMT** and Beta although other intergrowth systems such as **AEI**/**CHA**, SSZ-26/33 family, ***STO** family and **MER**/**PHI** are also important.

Zeolites belonging to ABC-6 family can be freely mixed each other without the introduction of defect sites.[30)] Two of the most famous intergrown structures belonging to ABC-6 family are **GME**/**CHA** and **OFF**/**ERI** shown in Figure 1.5.[30)] Although there are many theoretical intergrowth structures in ABC-6 family, an actual intergrowth structure is limited and complicatedly depend on the synthetic conditions. Direct imaging of minor intergrowth structures in **CHA**, **ERI**, **GME**, and **OFF**-type zeolites was carried out by high-resolution transmission electron microscope (HRTEM).[31)] Introduction of intergrowth sometimes changes the porous structure drastically. For example, **GME** (AABB…) has 12−8−8R channel system but its intergrown structure with **CHA** (AABBCC…) has 8−8−8R channel system because the straight 12R channel is blocked by the fault planes (C).[32)] Recently a new zeolite belonging ABC-6 family was discovered, called to SSZ-52 (**SFW**).[33,34)] Its structure is features by the highly elongated cages.

FAU/**EMT** is also classical intergrowth system and widely investigated by several research groups.[35−46)] Although faujasite is a much more classical zeolite mineral already known in 1950s,[47,48)] the discovery of **EMT**-type zeolite as intergrowth with **FAU**[36)] motivated the detailed structural analyses of this kind of materials and the development for the synthetic techniques for **FAU**/**EMT** with desired polymorph ratios. The structural difference between **FAU** and **EMT** can be explained by simple stacking disorder along with ***c*** axis as shown in Figure 1.6.[49)] This disorder does not require formation of defects and does not change 12−12−12R channel system significantly. Although low-silica **FAU**-type zeolites with Si/Al lower than 3 have been widely synthesized in simple SiO_2−Al_2O_3−Na_2O−H_2O hydrothermal systems, the high-silica versions with Si/Al > 3 were established by using 15-crown and/or 18-crown ether as an OSDA.[36)] At the same time, the remarkable hexagonal **FAU** crystal intergrown with **EMT** was discovered.[36)] Soon after the discovery of **EMT**,

almost pure **EMT**-type zeolite was prepared by optimizing synthetic conditions.[37] More detailed synthetic investigation and structural consideration were carried out later.[38] Direct observations of the intergrowth structures was carried out by HRTEM.[39,40] More systematic description of **FAU**/**EMT** intergrowths was proposed by using DIFFaX program which is Fortran 77 computer program to simulate diffraction from layered crystals that contain stacking faults.[41] Another route to prepare **FAU**/**EMT** intergrowth zeolites was reported, where treatment of the high-silica **EMT**-type zeolite with sodium potassium aluminate aqueous solution introduced intergrowth with **FAU** accompanying with Al incorporation.[42] The synthesis of low-silica **EMT**-type zeolites in organic-free conditions was reported recently.[46] Although the report did not referred to possibility for the obtained zeolite to contain intergrowth with **FAU**, the material probably contained the intergrowth, judging from significant broadening and extinction of the diffraction peaks, compared to those of typical **EMT**-type zeolites.

Zeolite Beta has 12−12−12R channel system and is the industrially important material as a multi-dimensional large-pore zeolite which can be prepared by relatively inexpensive OSDA (Et_4N^+). Beta is firstly synthesized by Mobil researchers in 1967.[50] After 21 years, the structure characterization was carried out by two independent research groups in 1988.[51,52] The reason why the structure had not been determined for two decades is the complicatedly intergrown structure of beta. Beta is composed of two polymorphs (A and B) and the ratio is 45:55 in most cases. Unlike one dimensional disorder observed in **FAU**/**EMT** and ABC-6 family, the disorder of beta is multi-dimensional, which make it difficult to determine its precise structure. More complicatedly, the multi-dimensional disorder often accompanies with defects. Actually, growth defects were observed in pure-silica beta by HRTEM.[53] Polymorph A is especially of great interest because of its chiral porous system, but the control of polymorph composition is extremely difficult and beta almost always crystallizes with A:B nearly 1:1. Another polymorph, named as C, was discovered in 2001 using germanium containing system.[54] ITQ-16 contained the three polymorphs and ITQ-17 consists of only polymorph C.[54] Beta polymorph C was synthesized in germanium-free conditions and more interestingly, polymorph B enriched beta was firstly synthesized by optimizing synthetic conditions.[56] In this reports, the use of potassium led the formation of polymorph C and the absence of alkali led the formation of polymorph B enriched beta.[55] Synthesis of these zeolites were reinvestigated in detail.[56] Another polymorph B enriched beta, called to NCL-7, was synthesized in $HClO_4$ containing gel.[57] Novel beta slightly enriched of polymorph A is very recently synthesized in extremely concentrated fluoride media.[58]

AEI/**CHA** intergrowth has been recently of great interest. SAPO-34 (silicoaluminophosphate with **CHA** topology) is a quite important catalyst for methanol-to-olefin (MTO) reaction and selective catalytic reduction (SCR).[59,60] SAPO-18 (**AEI**) is, on the other hand, not widely used as catalysts probably due to the difficulty to prepare it. However, SAPO-18 can be crystallize in very similar

synthetic conditions to that of SAPO-34. In other word, SAPO-34 can be easily intergrown with SAPO-18 and this **AEI**/**CHA** intergrowth materials would exhibit novel catalytic properties which SAPO-34 and SAPO-18 do not possess. To my best knowledge, the **AEI**/**CHA** intergrowth was firstly mentioned in 2002.[61] Several patents have reported the **AEI**/**CHA** intergrowth until 2011.[62–66] One of the patents showed good consistent between experimental and simulated powder XRD patterns of **AEI**/**CHA** intergrowth zeolites.[65] Recently, several academic approaches to investigate **AEI**/**CHA** was carried out,[67–70] although the precise **AEI**/**CHA** intergrowth structure is not still unveiled. It is important to distinguish **AEI**/**CHA** intergrowth from simple mixture of **AEI** and **CHA**.

Another noteworthy intergrowth structures will be introduced in the following sections.

1.4 Organic structure-directing agent for zeolite syntheses

To date, a number of zeolites have been synthesized using organic structure-directing agents (OSDAs) and the discoveries of new zeolites are often closely related to the use of new OSDAs. The OSDAs typically used in zeolite syntheses are shown in Figure 1.8. They are typically tetraalkylammonium cations without other functional groups. Templating is one of the major roles of the OSDAs and there are many examples where clear relationship can be seen between guest OSDAs and host zeolite frameworks.

SSZ-26, SSZ-33 and CIT-1 are large pore zeolites with 12−12−10R channel system, being composed of two closely related polymorphs (A and B).[71–74] SSZ-26 is an aluminosilicate zeolite synthesized by OSDA **I** shown in Figure 1.8. It has 15% of polymorph A and 85% of B. SSZ-33 is a borosilicate zeolite obtained by OSDA **II** and has 30% of polymorph A. Interestingly, intermediate phase between SSZ-26 and SSZ-33 was prepared in mixed OSDA system. CIT-1 is borosilicate and essentially pure polymorph B synthesized by OSDA **III**. This study revealed the possibility to control polymorph compositions of zeolites by choosing optimum OSDAs. One of the roles of the OSDAs in this system is to template the channel intersections where the large voids to occlude bulky OSDA cations.

Cage-type zeolites often have simple geometrical relationship between the pore architectures and the shape of OSDAs occluding inside micropores. As shown in Figure 1.9, the cage structure of **CHA**-type zeolites are clearly templated by 1-Trimethylammonioadamantane or benzyltrimethylammonium cations, which are actually two of the most famous OSDAs to obtain **CHA**-type zeolites.[75–77]

N,*N*,*N*',*N*'-Tetraethylbicyclo[2.2.2]oct-7-ene-2,3:5,6-dipyrrolidinium, denoted as $TEBOP^{2+}$, is an OSDA cation for **MSE**-type zeolties.[78] Major role of this OSDA is templating both the **MSE** cavitiy and straight 12R channel.[79] Actually, the structural analyses using powder XRD showed the $TEBOP^{2+}$ cation sitting in both the two sites.[79]

OSDA cations sometimes assembled with each other to template large cavities in zeolites. ITQ-

29, an aluminum-free **LTA**-type zeolite, is synthesized by supramolecular self-assembled cations.[80] The OSDA is *N*-methyljulolidinium which has planar structure. It is noteworthy that this is rare example to use anilinium as an OSDA. Tetraethylammonium, which is a relatively simple OSDA, is also considered to assemble with each other to template beta zeolites.[81] Although the size of one TEA^+ is smaller than the cavity of beta zeolites, an assembly of approximately 3−5 TEA^+ probably templates the ***BEA** framework.[81]

Another role of OSDA cations is to control the silicate building units and form the zeolite precursor in the gel. In the case of the synthesis of beta in highly concentrated system, *D3R* building units were elucidated as the precursor for beta zeolites.[82]

1.5 Usage of zeolites as starting materials for another zeolites

The utilization of zeolites as starting materials for another zeolites is widely applied in zeolite syntheses. Zeolite starting materials are of great interest since some structural similarities are often observed between starting materials and products. These zeolite materials possibly play a role as precursors for another zeolites.

We can categorize syntheses using zeolite as starting materials into 3 types according to the proportion of zeolites over conventional amorphous materials in initial synthesis mixtures. In the case of no conventional starting materials, that is referred to "zeolite hydrothermal conversion". In the case of low proportion of zeolite starting materials lower than 10%, that is referred to "seed-assisted crystallization technique". In the medium range from 10% to 100%, there is actually no special referred name but this region is significantly interesting because cooperation between zeolites and conventional starting materials is important.

The uses of zeolites as starting materials were actually carried out in 20th century. SSZ-13, which is one of the most famous zeolites as the NOx-SCR catalysts today, was firstly synthesized from zeolite P (**GIS**).[75,83] SSZ-16, which is also an important small-pore zeolite, was synthesized from **FAU**-type zeolites.[84] [B]-SSZ-24, [B]-SSZ-26, [B]-SSZ-33 and [B]-CIT-1 was synthesized by using [B]-beta zeolites as seed crystals.[72,85,86] Although these researches pioneered the potentials for utilization of zeolite materials for other novel zeolites, microscopic speculations such as role of zeolite materials, structural similarity between seeds and products and crystallization kinetics were not discussed so much at that period.

In 21st century, considerable efforts have been devoted to obtain the new zeolites with desired framework, particle size and Si/Al composition. Hydrothermal conversion of **FAU**-type zeolites into beta was carried out in 2006.[87] After this, **RUT**[88], **CHA**[89], **MSE**[90] and many other zeolites synthesized by hydrothermal conversion of **FAU**-type zeolites. **FAU**-type zeolites are special in 3 points, that are availability, variety of Si/Al composition and low framework density. Another recent major

study using zeolite starting materials is OSDA-free synthesis.[91] **BEA**[92,93], **MTW**[94,95], **MSE**[93], **CHA**[96] and **NES**-type zeolites[97] were synthesized without using OSDAs by seed-assisted crystallization technique. Similar approach was adapted for the synthesis of zeolites with simpler OSDAs. Seed-assisted crystallization of a **CON**-type zeolite was established by tetraethylammonium which is much simpler than conventional trimethyl((-)-*cis*-myrtanyl)ammonium.[98] Using **FAU**-type zeolites as aluminum sources in fluoride media combining other amorphous silica source, high-silica **LTA**, **ITW**, **CHA**, ***BEA** and **STT**-type zeolites were synthesized directly with high-silica compositions.[99]

The use of zeolites as starting materials is still developing method, so this work explored the role of zeolite starting materials on the crystallization of other zeolites by using a variety of OSDA cations.

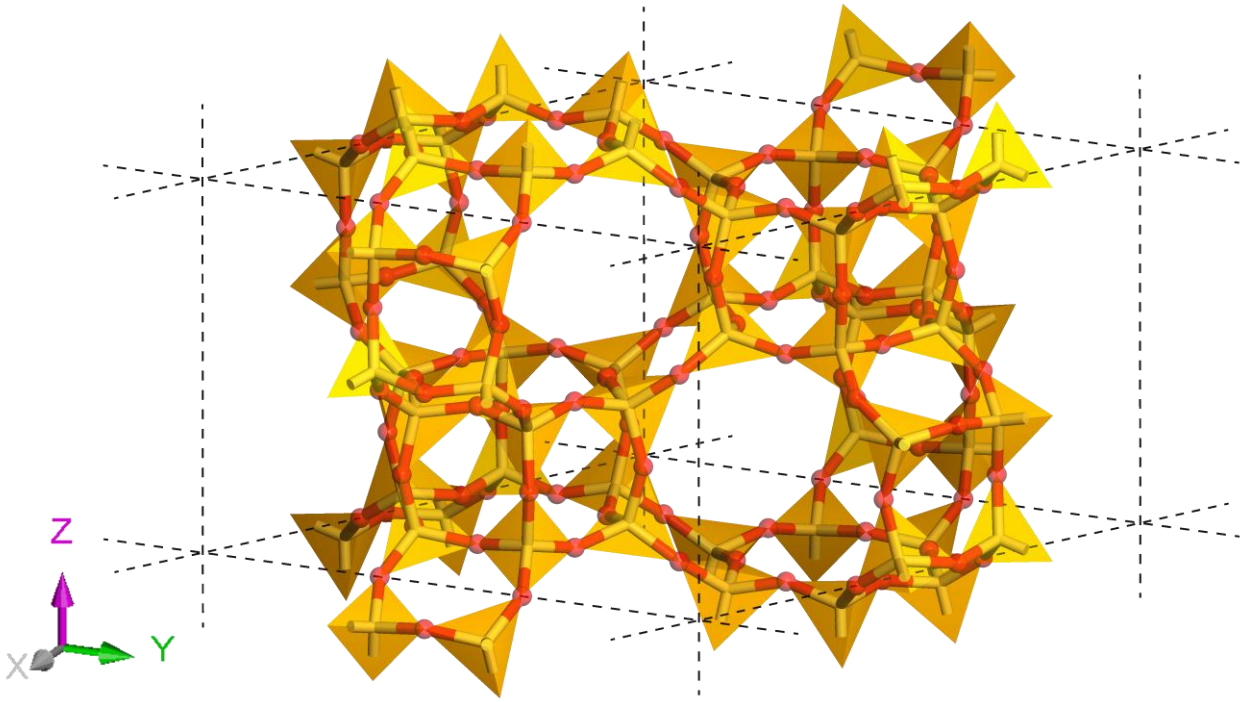

Figure 1.1. A zeolite framework (**GME**) comprises of TO_4 tetrahedra.

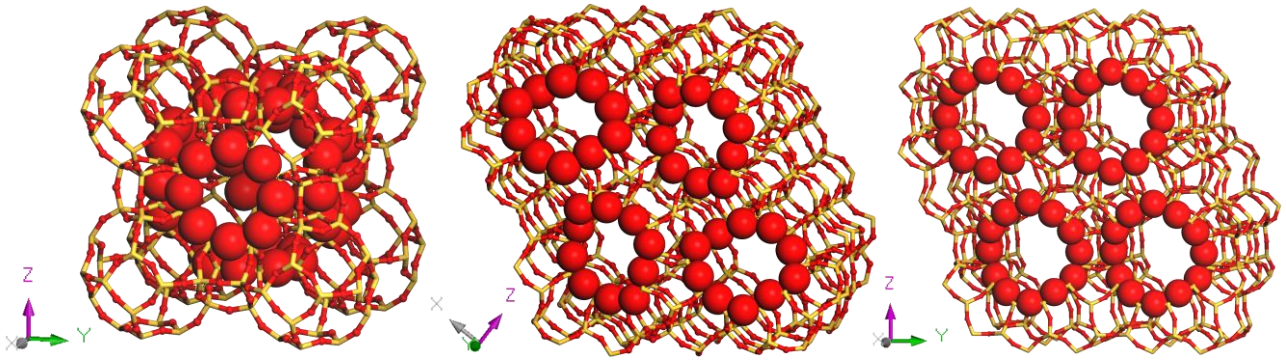

Figure 1.2. Examples of zeolites possessing (a) 8R (**LTA**), (b) 10R (**MFI**) and (c) 12R (beta) channels

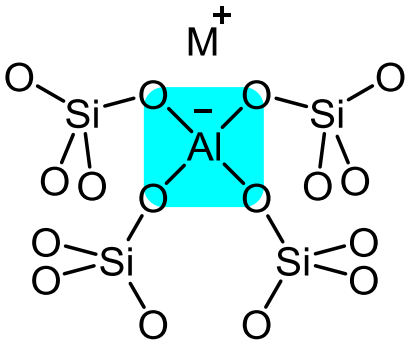

Figure 1.3. Chemical structure around an aluminum atom in a zeolite framework. The colored area represents where the anionic charge exists.

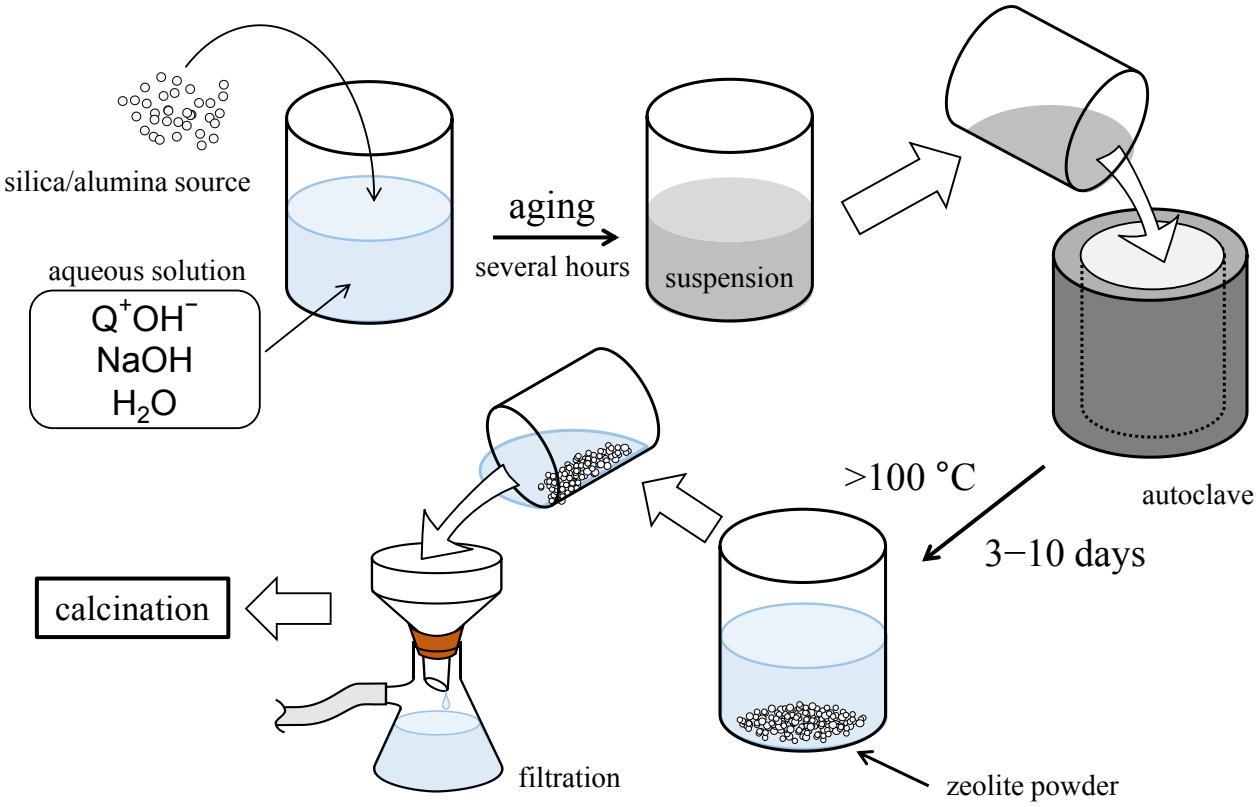

Figure 1.4. Scheme of typical zeolite synthesis. Q^+OH^- represents an organic structure-directing agent, typically quaternary ammonium hydroxide.

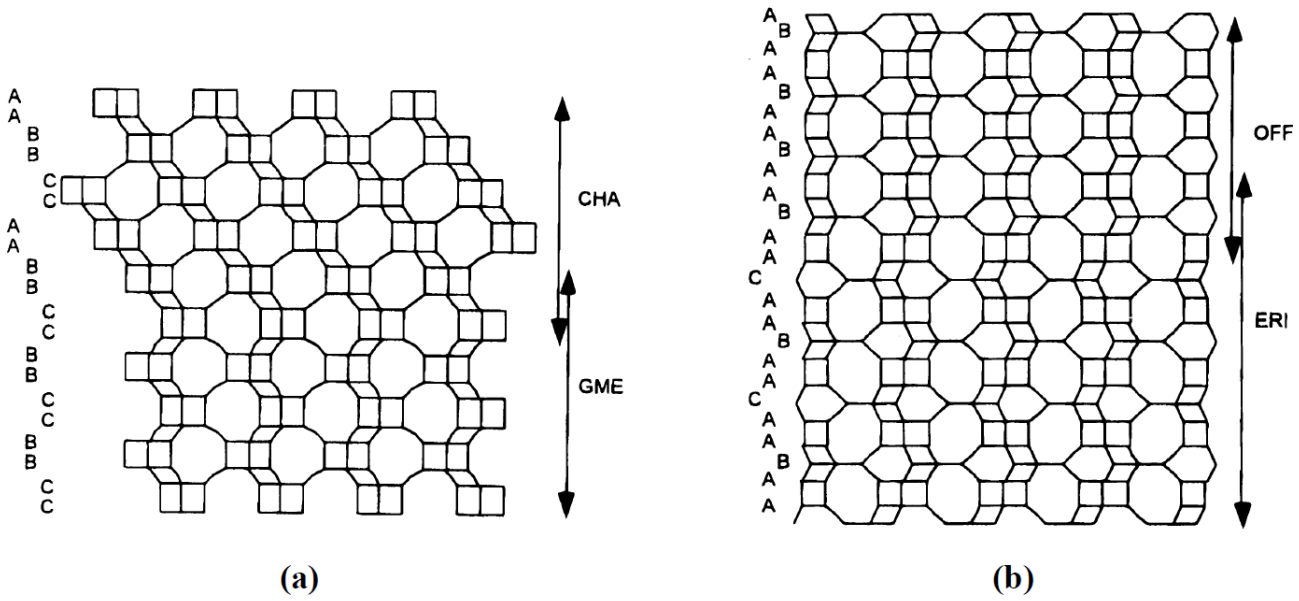

Figure 1.5. Examples of stacking disorder with (a) **CHA**/**GME** and (b) **OFF**/**ERI** (b) sequences.[22)]

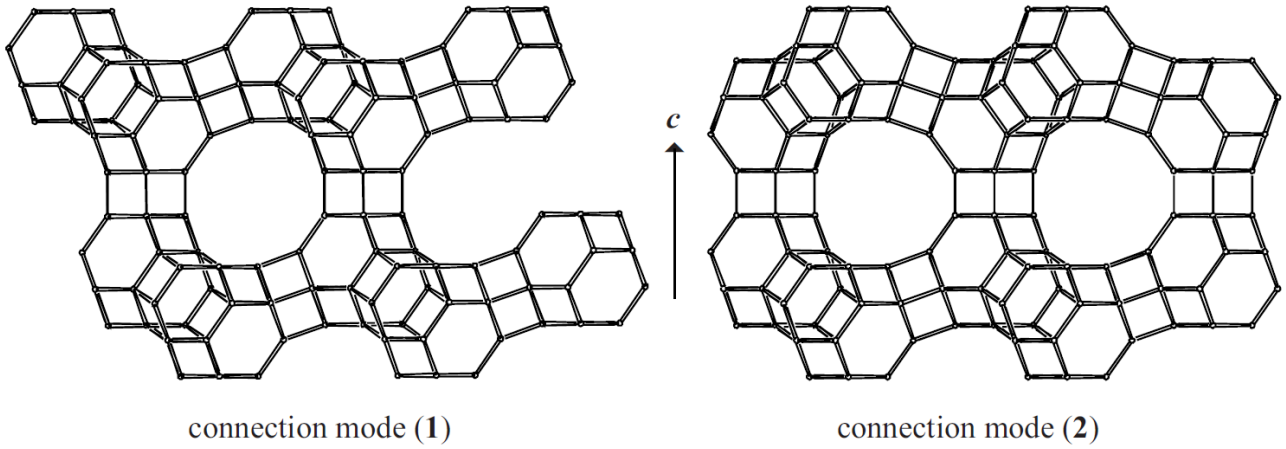

Figure 1.6. Connection mode (**1**) in **FAU** (left) and connection mode (**2**) in **EMT** (right).[41)]

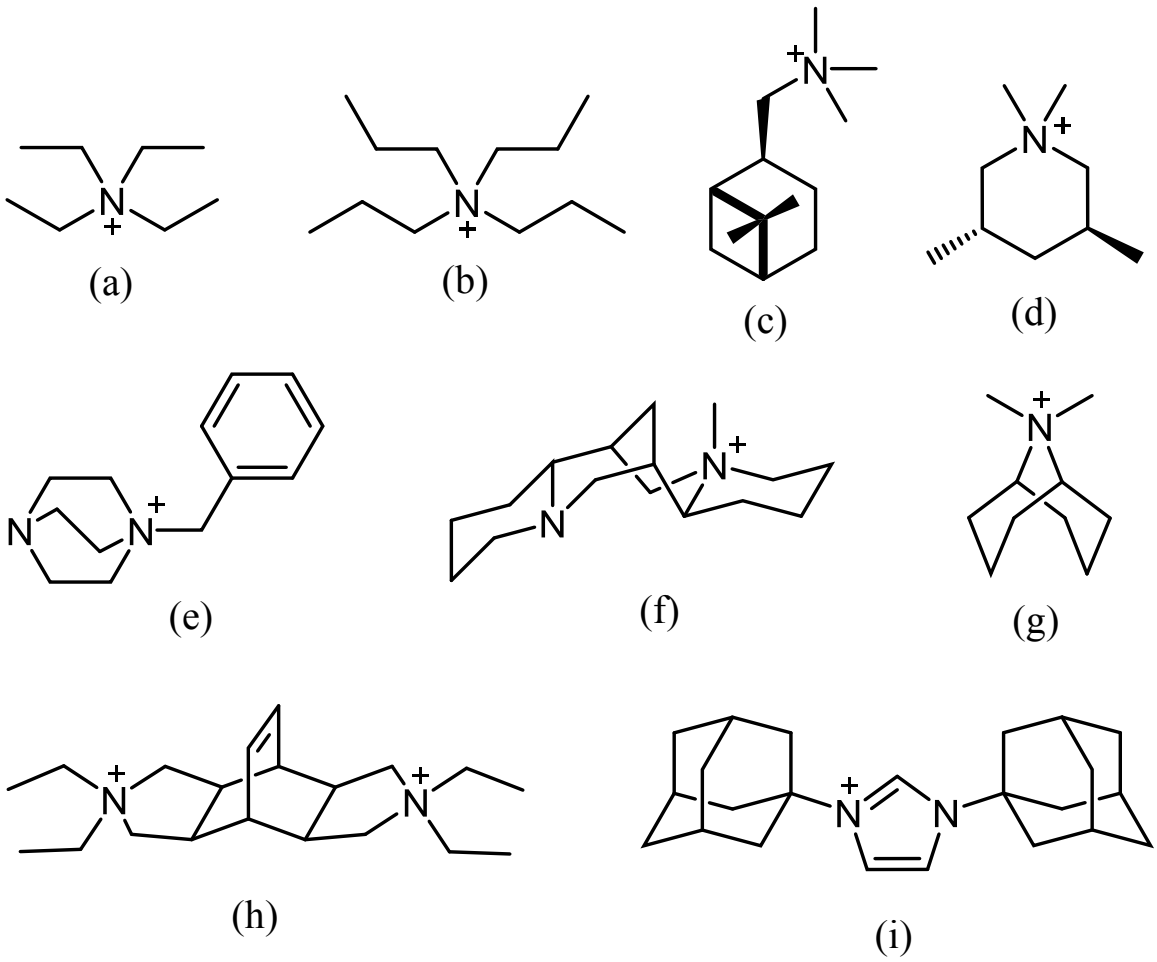

Figure 1.7. Several organic structure directing agents (OSDAs) typically used in zeolite syntheses. (a) tetraethylammonium, (b) tetrapropylammonium, (c) (1*R*, 2*R*, 5*R*)-trimethylammoniopinane, (d) *trans*-1,1,3,5-tetramethylpiperidinium, (e) 1-benzyl(1-azonia-4-azabicyclo[2.2.2]octane), (f) *N*(16)-methylsparteinium, (g) *9,9*-dimethyl-9-azoniabicyclo[3.3.1]nonane, (h) *N*,*N*,*N*',*N*'-tetraethylbicyclo[2.2.2]oct-7-ene-2,3:5,6-dipyrrolidinium and (i) bis(1-adamantyl)imidazolium.

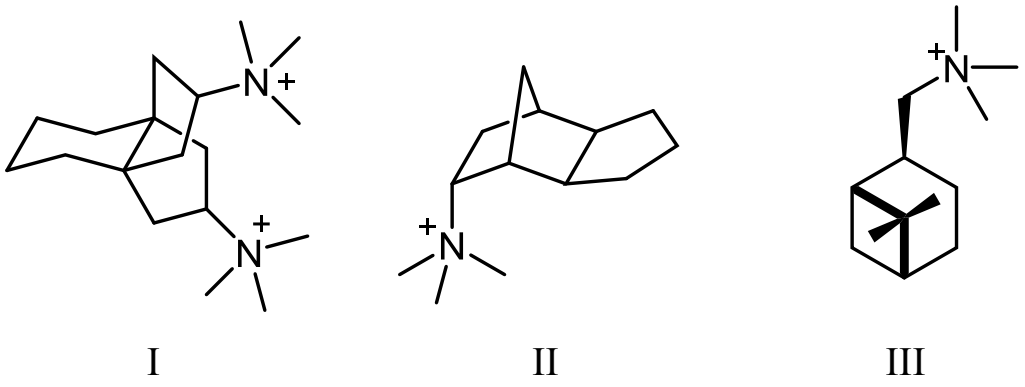

Figure 1.8. Organic structure-directing agents for (I) SSZ-26, (II) SSZ-33 and (III) CIT-1.

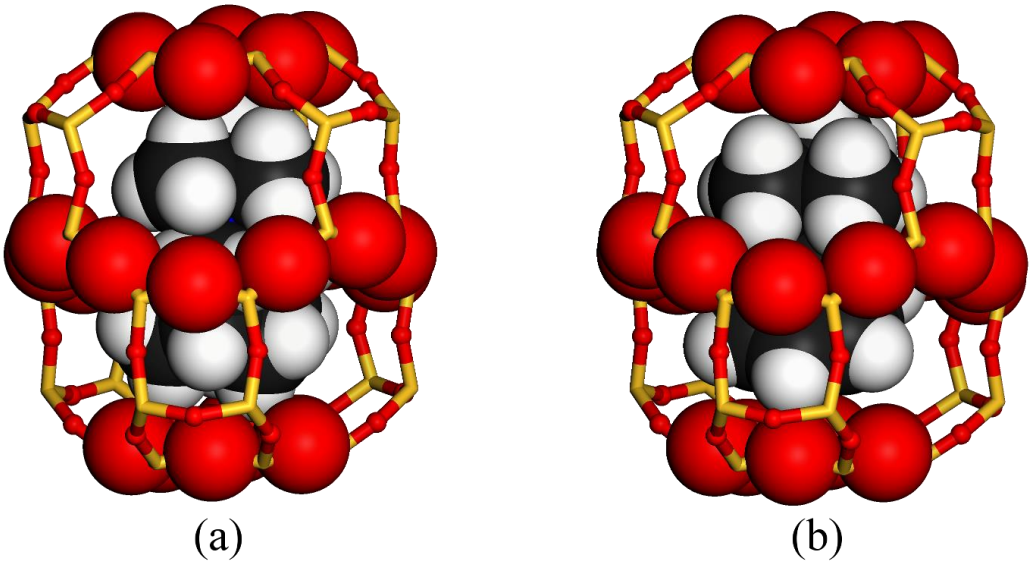

Figure 1.9. **CHA** cages occluding (a) 1-trimethylammonioadamantane and (b) benzyltrimethylammonium.

1.5 References

1 International Zeolite Association (IZA), http://www.iza-structure.org/databases/.

2 M.E. Davis, R.F. Lobo, *Chem. Mater.*, 4, 756 (1992).

3 M.S. Rana, V. Samano, J. Ancheyta, J.A.I. Diaz, *Fuel*, **86**, 1216 (2007).

4 J.-E. Otterstedt, Y.-M. Zhu, J. Sterte, *Appl. Catal.*, **38**, 143 (1988).

5 J. Dwyer, D.J. Rawlence, *Catal. Today*, **18**, 487 (1993).

6 W. Vermeiren, J.-P. Gilson, *Top. Catal.*, **52**, 1131 (2009).

7 R.H. Harding, A.W. Peters, J.R.D. Nee, *Appl. Catal. A*, **221**, 389 (2001).

8 Y.-M. Chen, *Powder Technol.*, **163**, 2 (2006).

9 J. Biswas, I.E. Maxwell, *Appl. Catal.*, **63**, 197 (1990).

10 A Corma, J Mengual, P.J. Miguel, *Appl. Catal. A*, **421**, 121 (2012).

11 Y. Kubota, S. Inagaki, Y. Nishita, K. Itabashi, Y. Tsuboi, T. Syahylah, T. Okubo, *Catal. Today,* **243**, 85 (2015)

12 S. Inagaki, K. Sato, S. Hayashi, J. Tatami, Y. Kubota, T. Wakihara, *ACS Appl. Mater. Interfaces*, **7**, 4488 (2015).

13 Y. Kubota, S. Inagaki, K. Takechi, *Catal. Today*, **226**, 109 (2014).

14 S. Park, Y. Watanabe, Y. Nishita, T. Fukuoka, S. Inagaki, Y. Kubota, *J. Catal*., 319, 273 (2014).

15 B.V. Vora, T.L. Marker, P.T. Barger, H.R. Nielsen, S. Kvisle, T. Fuglerud, *Stud. Surf. Sci. Catal.*,**107**, 87 (1997).

16 U. Olsbye, S. Svelle, M. Bjørgen, P. Beato, T.V.W. Janssens, F. Joensen, S. Bordiga, K.P. Lillerud, *Angew. Chem. Int. Ed.*, **51**, 5810 (2012).

17 I. Bull, R.S. Boorse, W.M. Jaglowski, G.S. Koermer, A. Moini, J.A. Patchett, W.M. Xue, P. Burk, J.C. Dettling, M.T. Caudle, *US Patent*, 0 226 545 (2008).

18 M. Moliner, C. Franch, E. Palomares, M. Grill, A. Corma, *Chem. Commun.*, **48**, 8264 (2012).

19 D.W. Fickel, E. D'Addio, J.A. Lauterbach, R.F. Lobo, *Appl. Catal., B: Environ.*, **102**, 411 (2011).

20 R.M. Barrer, *Zeolites*, **1**, 30 (1981).

21 R.M. Barrer, P.J. Denny, *J. Chem. Soc.*, 971 (1961).

22 M. Matsukata, M. Ogura, T. Osaki, P.R.H.P. Rao, M. Nomura, E. Kikuchi, *Top. Catal.*, **9**, 77 (1991).

23 T. Ikeda, S. Inagaki, T. Hanaoka, Y. Kubota, *J. Phys. Chem. C*, **114**, 19641 (2010).

24 R.E. Morris, S.J. Weigel., *Chem. Soc. Rev.*, **26**, 309 (1997).

25 E.R. Cooper, C.D. Andrews, P.S. Wheatley, P.B. Webb, P. Wormald, R.E. Morris, *Nature*, **420**, 1012 (2004).

26 D.M. Ginter, A.T. Bell, C.J. Radke, *Zeolites*, **12**, 742 (1992).

27 P. Wagner, Y. Nakagawa, G.S. Lee, M.E. Davis, S. Elomari, R.C. Medrud, S.I. Zones, *J. Am. Chem. Soc.*, **122**, 263 (2000).

28 T. Shibata, S. Suzuki, H. Kawagoe, K. Komura, Y. Kubota, Y. Sugi, J.-H. Kim, G. Seo, *Micropor. Mesopor. Mater.*, **116**, 216 (2008).

29 R.H. Daniels, G.T. Kerr, L.D. Rollmann, *J. Am. Chem. Soc.*, **100(10)**, 3097 (1978).

30 *ABC-6 family*, http://www.iza-structure.org/databases/Catalog/ABC_6.pdf.

31 G.R. Millward, S. Ramdas, J.M. Thomas, *Proc. R. Soc. Lond. A*, **399**, 57 (1985).

32 G.T. Kokotailo, S.L. Lawton, *Nature*, **203**, 621 (1964).

33 D. Xie, L.B. McCusker, C. Baerlocher, S.I. Zones, W. Wan, X. Zou, *J. Am. Chem. Soc.*, **135**, 10519 (2013).

34 T.M. Davis, A.T. Liu, C.M. Lew, D. Xie, A.I. Benin, S. Elomari, S.I. Zones, M.W. Deem, *Chem. Mater.*, DOI: 10.1021/acs.chemmater.5b04578.

35 J.A. Martens, P.A. Jacobs, S. Cartlidge, *Zeolites*, **9**, 423 (1989).

36 F. Delprato, L. Delmotte, J.L. Guth, L. Huve, *Zeolites*, **10**, 546 (1990).
37 F. Dougnier, J. Patarin, J.L. Guth, D. Anglerot, *Zeolites*, **12**, 160 (1992).
38 S.L. Burkett, M.E. Davis, *Micropor. Mater.*, **1**, 265 (1993).
39 O. Terasaki, T. Ohsuna, V. Alfredsson, J.-O. Bovin, D. Watanabe, S.W. Carr, M.W. Anderson, *Chem. Mater.*, **5**, 452 (1993).
40 T. Ohsuna, O. Terasaki, D. Watanabe, M.W. Anderson, S.W. Carr, *Chem. Mater.*, **6(12)**, 2201 (1994).
41 M.M.J. Treacy, D.E.W. Vaughan, K.G. Strohmaier, J.M. Newsam, *Proc. R. Soc. Lond. A*, **452**, 813 (1996).
42 H.-X. Li, J.N. Armor, *Micropor. Mater.*, **9**, 51 (1997).
43 A. Haas, D. A. Harding, J.R.D. Nee, *Micropor. Mesopor. Mater.*, **28**, 325 (1999).
44 A.L. Yonkeu, V. Buschmann, G. Miehe, H. Fuess, A.M. Goossens, J.A. Martens, *Cryst. Eng.*, **4**, 253 (2001).
45 G. Gonzalez, C.S. Gonzalez, W. Stracke, R. Reichelt, L. Garcia, *Micropor. Mesopor. Mater.*, **101**, 30 (2007).
46 E.-P. Ng, D. Chateigner, T. Bein, V. Valtchev, S. Mintova, *Science*, **335**, 70 (2012).
47 G. Bergerhoff, W.H. Baur, W. Nowacki, *N. Jb. Miner. Mh.*, 193 (1958).
48 W.H. Baur, *Am. Mineral.*, **49**, 697 (1964).
49 *Building scheme for EMT and **FAU***, http://www.iza-structure.org/databases/ModelBuilding/EMT.pdf.
50 R.L. Wadlinger, G.T. Kerr, E.J. Rosinski, US Patent, 3 308 069 (1967).
51 J.M. Newsam, M.M.J. Treacy, W.T Koetsier, *Proc. R. Soc. Lond. A*, **420**, 375 (1988).
52 J.B. Higgins, R.B. LaPierre, J.L. Schlenker, A.C. Rohrman, J.D. Wood, G.T. Kerr, W.J. Rohrbaugh, *Zeolites*, **8**, 446 (1988).
53 P.A. Wright, W. Zhou, J. Perez-Pariente, M. Arranz, *J. Am. Chem. Soc.*, **127**, 494 (2005).
54 A. Corma, T. Navarro, F. Rey, S. Valencia, *Chem. Commun.*, 1720 (2001).
55 A. Cantin, A. Corma, M.J. Diaz-Cabanas, J.L. Jorda, M. Moliner, F. Rey, *Angew. Chem. Int. Ed.*, **45**, 8013 (2006).
56 A. Corma, M. Moliner, A. Cantin, M.J. Diaz-Cabanas, J.L. Jorda, D. Zhang, J. Sun, K. Jansson, S. Hovmoller, X. Zou, *Chem. Mater.*, **20**, 3218 (2008).
57 M.D. Kadgaonkar, M.W. Kasture, D.S. Bhange, P.N. Joshi, V. Ramaswamy, R. Kumar, *Micropor. Mesopor. Mater.*, **101**, 108 (2007).
58 M. Tong, D. Zhang, W. Fan, J. Xu, L. Zhu, W. Guo, W. Yan, J. Yu, S. Qiu, J. Wang, F. Deng, R. Xu, *Sci. Rep.*, **5**, 11521 (2015).
59 B.V. Vora, T.L. Marker, P.T. Barger, H.R. Nielsen, S. Kvisle, T. Fuglerud, *Stud. Surf. Sci. Catal.*, **107**, 87 (1997).
60 F. Gao, E.D. Walter, N.M. Washton, J. Szanyi, C.H.F. Peden, *ACS Catal.*, **3**, 2083 (2013).
61 R. Wendelbo, D.E. Akporiaye, A. Andersen, H.B. Mostad, T. Fuglerud, S. Kvisle, US Patent, 6 334 994 B1 (2002).
62 M.J. Janssen, Verberckmoes, M.M. Mertens, A.J. Bons, W.J. Mortier, Eur. Patent, 1 365 992 B1 (2007).
63 W. Sinkler, R.W. Broach, N. Erdman, T.M. Reynolds, J.Q. Chen, S.T. Wilson, P.T. Barger, US Patent, 7 547 812 B2 (2009).
64 M.M. Mertens, US Patent, 7 622 417 B2 (2009).
65 M.M. Mertens, A. Verberckmoes, M.J. Janssen, Y.F. Chang, L.R.M. Martens, S.N. Vaughn, K.R. Clem, W.J. Mortier, US Patent, 7 622 624 B2 (2009).
66 M.M. Mertens, A. Verberckmoes, M.J. Janssen, Y.F. Chang, L.R.M. Martens, S.N. Vaughn, K.R. Clem, W.J. Mortier, US Patent, 7 914 760 B2 (2011).
67 E.E. Knyazeva, S.V. Konnov, O.V. Shutkina, I.V. Dobryakova, O.A. Ponomareva, I.I. Ivanova, *Petro. Chem.*, **54**, 288 (2014).

68 R.L. Smith, S. Svelle, P. Campo, T. Fuglerud, B. Arstad, A. Lind, S. Chavan, M.P. Attfield, D. Akporiaye, M.W. Andersona, *Appl. Catal. A*, **505**, 1 (2015).

69 R.L. Smith, W.A. Slanwinski, A. Lind, D.S. Wragg, J.H. Cavka, B. Arstad, H. Fjellvag, M.P. Attfield, D. Akporiaye, M.W. Anderson, *Chem. Mater.*, **27**, 4205 (2015).

70 Y. Hu, H. Chen, Y. Hu, J. Deng, Z. Lv, H. Zhang, *Chem. Lett*., **44**, 1116 (2015).

71 R.F. Lobo, S.I. Zones, M.E. Davis, *Stud. Surf. Sci. Catal*, **84**, 461 (1994).

72 R.F. Lobo, M. Pan, I. Chan, H.-X. Li, R.C. Medrud, S.I. Zones, P.A. Crozier, M.E. Davis, *Science*, **262**, 1543 (1993).

73 R.F. Lobo, M. Pan, I. Chan, R.C. Medrud, S.I. Zones., P.A. Crozier, M.E. Davis, *J. Phys. Chem.*, **98**, 12040 (1994).

74 R.F. Lobo, M.E. Davis, *J. Am. Chem. Soc.*, **117**, 3766 (1995).

75 S.I. Zones, R.A.V Nordstrand, *Zeolites*, **8**, 166 (1988).

76 M. Itakura, T. Inoue, A. Takahashi, T. Fujitani, Y. Oumi, T. Sano, *Chem. Lett.*, **37**, 908 (2008).

77 M. Itakura, I. Goto, A. Takahashi, T. Fujitani, Y. Ide, M. Sadakane, T. Sano, *Micropor. Mesopor. Mater.*, **144**, 91 (2011).

78 D.C. Calabro, J.C. Cheng, R.A. Crane Jr., C.T. Kresge, S.S. Dhingra, M.A. Steckel, D.L. Stern, S.C. Weston, US Patent, 6 049 018 (2000).

79 Y. Koyama, T. Ikeda, T. Tatsumi, Y. Kubota, *Angew. Chem. Int. Ed.*, **47**, 1042 (2008).

80 A. Corma, F. Rey, J. Rius, M.J. Sabater, S. Valencia, Nature, 431, 287 (2004).

81 T. Ikuno, W. Chaikittisilp, Z. Liu, T. Iida, Y. Yanaba, T. Yoshikawa, S. Kohara, T. Wakihara, T. Okubo, *J. Am. Chem. Soc.*, **137**, 14533 (2015).

82 S. Inagaki, K. Nakatsuyama, Y. Saka, E. Kikuchi, S. Kohara, M. Matsukata, *J. Phys. Chem. C*, **111**, 10285 (2007).

83 S.I. Zones, R.A. Van Nordstrand, *Zeolites*, **8**, 409 (1988).

84 S.I. Zones, US Patent, 5 194 235 (1993).

85 S.I. Zones, Y. Nakagawa, *Micropor. Mater.*, **2**, 543 (1994).

86 R.F. Lobo, M.E. Davis, *Micropor. Mater.*, **3**, 61 (1994).

87 H. Jon, K. Nakahata, B. Lu, Y. Oumi, T. Sano, *Micropor. Mesopor. Mater.*, **96**, 72 (2006)

88 H. Jon, S. Takahashi, H. Sasaki, Y. Oumi, T. Sano, *Micropor. Mesopor. Mater.*, **113**, 56 (2008)

89 M. Itakura, I. Goto, A. Takahashi, T. Fujitani, Y. Ide, M. Sadakane, T. Sano, *Micropor. Mesopor. Mater.*, **144**, 91 (2011)

90 S. Inagaki, Y. Tsuboi, Y. Nishita, T. Syahylah, T. Wakihara, Y. Kubota, *Chem. Eur. J.*, **19**, 7780 (2013)

91 K. Iyoki, K. Itabashi, T. Okubo, *Micropor. Mesopor. Mater.*, **189**, 22 (2014).

92 B. Xie, J. Song, L. Ren, Y. Ji, J. Li, F.S. Xiao. *Chem. Mater.*, **20**, 4533 (2008).

93 Y. Kubota, K. Itabashi, S. Inagaki, Y. Nishita, R. Komatsu, Y. Tsuboi, S. Shinoda, T. Okubo, *Chem. Mater.*, **26**, 1250 (2014).

94 K Iyoki, Y. Kamimura, K. Itabashi, A. Shimojima, T. Okubo, *Chem. Lett.*, **39**, 730 (2010).

95 Y. Kamimura, K. Itabashi, T. Okubo, *Micropor. Mesopor. Mater.*, **147** 149(2012).

96 H. Imai, N. Hayashida, T. Yokoi, T. Tatsumi, *Micropor. Mesopor. Mater.*, **196**, 341 (2014).

97 K. Iyoki, M. Takase, K. Itabashi, K. Muraoka, W. Chaikittisilp, T. Okubo, *Micropor. Mesopor. Mater.,* **215**, 191 (2015).

98 S. Sogukkanli, K. Iyoki, S.P. Elangovan, K. Itabashi, T. Okubo. *Chem. Lett*. **46**, 1419 (2017).

99 T. Moteki, R.F. Lobo, *Chem. Mater*. **28**, 638 (2016).

Chapter Two

新規*STO型ゼオライトの開発

Novel synthesis of *STO-type zeolite

*Novel ***STO**-type molecular sieves have been successfully synthesized by using trimethyl((-)-cis-myrtanyl)ammonium ($TMMA^+$) as an organic structure-directing agent (OSDA). Pure-silica beta zeolites with less than 500 nm in diameter were used as seed crystals for the crystallization. CIT-1 crystals were also effective to promote the crystallization. The sizes of seed crystals strongly influenced on the morphologies and sizes of obtained ***STO** crystals. This novel synthetic technique to obtain an ***STO**-type zeolite with desired crystal sizes should enhance its potentials for industrial applications especially as the highly shape-selective solid acid catalyst.*

Key words: YNU-4 zeolite, ***STO** framework, seed-assisted crystallization, structure-directing agent.

2.1 Introduction

Zeolites are microporous crystalline aluminosilicate materials with 0.3–1.0 nm pore apertures. They have been widely applied in catalytic reactions as well as adsorption and separation processes. Two of the most important factors which influence on the catalytic properties of zeolites are Si/Al composition and crystal size, and controlling these factors is highly important for the practical applications.

A numerous number of zeolites have been synthesized by using organic structure-directing agents (OSDAs).[1,2] Recently seed-assisted crystallization techniques have also widely performed to obtain novel types of zeolitic materials. For instance, the crystallization of [B]-CIT-1 rapidly occurred by the addition of a small amount of [B]-beta to the synthesis mixture.[3] In the synthesis of nanosized ZSM-5, seeding of silicalite-1 was effective to avoid the formation of MOR.[4] Syntheses of beta,[5,6] **MTW**[7], **MSE**[6] and high-silica **CHA**[8] in the absence of OSDAs were established by seed-assisted techniques.

An ***STO**-type zeolite possesses one-dimensional 12R channel system with 0.86 × 0.57 nm apertures.[9] The 10 polytypes (A–J)[10] are known and none of them has been synthesized as a pure form. To date, 3 ***STO**-type zeolites have been reported as SSZ-31,[11,14,15] NCL-1[12] and OU-1.[13] [B]-SSZ-31 was firstly synthesized from a number of quaternary ammonium cations in 1992.[11] NCL-1 which is quite similar to SSZ-31 was obtained as an aluminosilicate by using 1,1,1,8,8,8-hexaethyl-1,8-diazoniaoctane ($Et_3N^+(CH_2)_6N^+Et_3$) in 1994.[12] OU-1 was synthesized as an aluminosilicate by dry-

gel conversion (DGC) technique by using tetraethylammonium hydroxide in 1999.[13] [Al]-SSZ-31 was prepared by DGC using 1,1,1,8,8,8-hexaethyl-1,8-diazoniaoctane in 2001.[14] Later, it was also obtained in hydrothermal synthetic system by using [Al]-beta as a starting material.[15] Both [Al]-SSZ-31 showed high shape-selectivity in the alkylation of biphenyl with propylene.[16]

Trimethyl((-)-*cis*-myrtanyl)ammonium ($TMMA^+$, Figure 2.1) has already been known as a powerful OSDA for [B]-CIT-1.[3] Recently aluminum-containing [Al,B]-CIT-1 was also obtained in the presence of aluminum and boron sources[17]. To our best knowledge, however, none of aluminosilicate zeolite has been obtained by $TMMA^+$. In this work, aluminum-containing ***STO**-type zeolites have been successfully obtained by using $TMMA^+$. This is the first aluminosilicate zeolite obtained by $TMMA^+$ in the absence of boron sources. More interestingly, all-silica beta (Si-beta) or CIT-1 crystals were essential as seed crystals and their particle sizes strongly affect the particle morphologies and sizes of the products. Because of these special features, this novel ***STO**-type zeolite will be designated to YNU-4 (Yokohama National University-4).

2.2 Experimental

2.2.1 Synthesis of 4,4'-trimethylenebis(1-benzyl-1-methylpiperidinium) dihydroxide

4,4'-trimethylenebis(1-benzyl-1-methylpiperidinium) dihydroxide, denoted as $TMBP^{2+}(OH^-)_2$, was synthesized according to the published procedure with slight modifications (Figure 2.2).[18–20]

4,4'-Trimethylenebis(1-methylpiperidine) (17.3 g, 70 mmol) and ethyl acetate (420 mL) was mixed in 1000-mL recovery flask and benzyl bromide (21.2 mL, 175 mmol, TCI) was added dropwise over 10 min. The whole mixture was stirred at room temperature for 124 h. The resulting suspension was filtered using a glass filter, and the residue was washed with a mixture of ethyl acetate (100 mL) and diethyl ether (100 mL). The crude solid was dried in a vacuum desiccator to give a slightly yellowish white solid (42.0 g, 100%). It was recrystallized with EtOH (300 mL), and diethyl ether (150 mL) was added dropwise over 1 h at room temperature. The resultant solid was collected by suction filtration and washed with a mixture of diethyl ether (100 mL) and EtOH (100 mL). Finally it was washed with benzene (100 mL) and dried in a vacuum desiccator to give slightly yellowish white solid (35.5 g, 57%).

Diaion® SA10A(OH) (Mitsubishi Chemical Co.) anion-exchange resin (136 g, corresponding to 245 mmol of exchange capacity) was added into a solution of the dibromide salt (35.5 g, 61.2 mmol) in distilled water (260 mL). The whole mixture was kept statically for 120 h. After filtration, the aqueous solution was concentrated to 155 g to give 0.362 mmol/g $TMBP^{2+}(OH^-)_2$ based on HCl titration of the resulting solution. The yield was 92%.

2.2.2 Synthesis of Si-beta

A typical procedure to synthesize Si-beta is as follows. $TMBP^{2+}(OH^{-})_2$ aqueous solution (0.280 mmol/g, 26.74 g) and distilled water (17.48 g) were mixed in a 180-mL PFA beaker, and $Si(OEt)_4$ (10.52 g) was added dropwise over 10 min. The mixture was stirred at room temperature for 22 h until 11.23 g of solvent (EtOH and H_2O) was evaporated. As-synthesized Si-beta crystals (0.062 g) were added and then the whole mixture was stirred for another 1 h. The composition of the synthesis mixture is 1.0 SiO_2–0.150 $TMBP^{2+}(OH^{-})_2$–39 H_2O. The hydrothermal treatment was carried out at 135 °C for 8 days using a 125-mL Teflon-lined autoclave. After cooling it down to room temperature, the obtained solid was recovered by centrifuging, washed several times with distilled water, and dried at 100 °C overnight. The as-synthesized Si-beta zeolite was obtained as white powder (2.92 g). The calcination was carried out in a muffle furnace. The temperature was raised from room temperature to 550 °C under 1.5 °C/min of the ramping rate, and maintained at the same temperature for 6 h. Finally, the sample was cooled to room temperature to give a calcined sample as white powder.

2.2.3 Synthesis of deboronated CIT-1 (siliceous CIT-1)

Since the crystallization of CIT-1 occur only in the presence of boron, we carried out the synthesis and [B]-CIT-1 and the subsequent deboronation.

The synthesis of [B]-CIT-1 was carried out based on the known procedure.[3)] [B]-beta seed crystals for [B]-CIT-1 was also synthesized according to the known procedure by dry-gel conversion (DGC) technique using tetramethylammonium.[21)] A typical procedure to synthesize [B]-CIT-1 is as follows. $TMMA^{+}OH^{-}$ (0.577 mmol/g, 34.68 g), NaOH (0.940 mmol/g, 10.64 g), deionized water (4.2063) and $B(OH)_3$ (Wako, 0.3107 g) were mixed and stirred until $B(OH)_3$ was completely dissolved (ca. 5 min at r.t.). As-synthesized [B]-Beta crystals (0.3907 g, 5wt% based on SiO_2) were added and stirred for 5 min at r.t. for dispersion. Next, fumed silica (Cab-O-Sil M5) was added and stirred for 6 hours at r.t. The composition of the synthesis mixture was 1.0 SiO_2–0.050 $B(OH)_3$–0.20 $TMMA^{+}OH^{-}$–0.10 NaOH–25 H_2O. The mixture was transferred into a 125-mL Teflon-lined stainless-steel autoclave and the crystallization was carried out at 160 °C for 9 h under tumbling conditions (20 rpm). The solid product was filtered and washed with deionized water several times. The sample was died at 80 °C overnight and 5.23 g of white powder was obtained. The calcination for the removal of OSDAs was carried out at 600 °C for 3 h. 4.78 g of the as-synthesized sample gave 4.48 g of calcined [B]-CIT-1.

Deboronation was carried out based on the reported procedure.[22)] The typical procedure was as follows. 1.00 g of calcined [B]-CIT-1 was dispersed into 100 mL of 0.01 M HCl solution in a 100-mL PP bottle. The bottle was tightly sealed and the suspension was kept at 100 °C under static conditions. The solid was recovered by filtration to give 0.792 g of deboronated CIT-1.

2.2.4 Synthesis of YNU-4 zeolite

A typical procedure to synthesize YNU-4 is as follows. $TMMA^+OH^-$ (0.563 mmol/g, 5.3 g), NaOH (0.519 mmol/g, 5.81 g), distilled water (1.52 g) and amorphous $Al(OH)_3$ (Aldrich, 50−57wt%, 0.0029 g) were mixed and stirred until $Al(OH)_3$ was completely dissolved. Fumed silica (Cab-O-Sil M5, 0.860 g) and seed crystals (calcined Si-beta, 0.048 g) was added and stirred gently for 4 h at room temperature. The composition of the synthesis mixture is 1.0 SiO_2–0.002 $Al(OH)_3$–0.20 $TMMA^+OH^-$ –0.20 NaOH–44 H_2O. The mixture was transferred into a 23-mL Teflon-lined autoclave and it was settled in an oven at 160 °C for 94 h. The solid product was filtered and washed with distilled water several times. The sample was dried at 80 °C overnight and 0.440 g of white powder was obtained. The calcination for the removal of OSDAs was carried out at 600 °C for 3 h. The syntheses using CIT-1 seed crystals were carried out in a similar manner.

2.2.5 Characterization

The crystallinity and phase purity of the zeolite samples were examined by powder X-ray diffraction (XRD) on an Ultima-IV (Rigaku) using CuKα radiation at 40 kV and 20 mA. The Si/Al and Na/Al molar ratios in the bulk were determined by inductively coupled plasma, atomic emission spectrometer (ICP-AES, ICPE-9000, Shimadzu). Nitrogen adsorption and desorption isotherms at −196 °C were collected for the samples pre-treated at 400 °C for 12 h on a BELSORP-max gas adsorption instrument (MicrotracBEL). The morphologies of zeolite samples were observed by scanning electron microscope (SEM) on a JSM-7001F (JEOL). The organic contents included in the as-synthesized zeolite were determined by thermogravimetric and differential thermal analysis (TG-DTA, Thermo plus EVO II TG8120, Rigaku). The solid-state magic angle spinning nuclear magnetic resonance (MAS NMR) measurements were performed by using AVANCEIII 600 (Bruker) operating at 600 MHz for ^1H, 119.2 MHz for ^{29}Si and 156.4 MHz for ^{27}Al. All of the MAS NMR spectra were recorded at room temperature with samples in a 4 mm diameter ZrO_2 tube. The ^{27}Al chemical shifts were determined by using an aqueous $Al(NO_3)_3$ solution, the resonance peak of which was adjusted to 0 ppm. The direct-excitation (DE) MAS NMR spectra were recorded by using 1024 pulses with a recycle time of 0.5 s at a spinning rate of 13 kHz.

2.3 Results and discussions

2.3.1 Syntheses of Si-beta with various particle sizes

Three types of as-synthesized Si-beta crystals, respectively denoted as Si-beta-1, Si-beta-2 and Si-beta 3, were obtained by changing synthetic conditions as listed in Table 1. Figures 2.3 and 2.4 show the powder XRD patterns of as-synthesized and calcined Si-beta samples, respectively. Each of them was pure enough to use as seeds for the following crystallization although a trace amount of **MTW**

was observed in sample 3. Figure 2.5 exhibits FE-SEM images of Si-beta samples, revealing the tendency that the particle sizes increase with increasing synthetic temperature. The particle sizes of Si-beta-1, -2 and -3 were estimated to be 50−100 nm, 300−500 nm and 800−1200 nm in diameter, respectively. Morphologies of Si-beta-1 and -2 were spherical. On the other hand, Si-beta-3 showed bipyramidal morphology that is typically observed in beta zeolites.

2.3.2 Syntheses of YNU-4 by using calcined Si-beta as seed crystals

The three Si-beta zeolites were used as seed crystals to obtain YNU-4. Table 2.2 shows the synthetic conditions and the results. No crystalline phases were obtained without the aid of seed crystals (entry 1). Figure 2.6 shows the crystalline-phase change with a time course when Si-beta-1 (50–100 nm in diameter) was seeded. Although no crystalline phases appeared after 22 h, the crystallization rapidly occurred and YNU-4 was obtained after 44 h as a pure form. The prolonged hydrothermal treatment till 66 h co-produced cristobalite as an impurity, indicating that the excess of crystallization time leads to the formation of any dense phases which are thermodynamically more stable than YNU-4. Figure 2.7 shows the crystalline-phase change with a time course when Si-beta-2 (300–500 nm in diameter) was seeded. Although no crystallization occurred after 48 h, YNU-4 began to appear after 74 h and the fully crystallized YNU-4 was obtained after 94 h. Interestingly, seeding Si-beta-2 resulted in a double longer crystallization period compared to seeding Si-beta-1, suggesting the size of Si-beta crystals strongly affects nucleation step of YNU-4. The further hydrothermal treatment till 138 h led to the formation of a dense phase.

In contrast, Si-beta-3 (800–1200 nm) did not give pure YNU-4 (Figure 2.8). Although YNU-4 appeared along with kenyaite (one of the layered silicate) after 94 h, a YNU-4 phase almost disappeared and kenyaite was completely crystallized after 138 h. It indicates that the large seed crystals do not play a so significant role on the crystallization of YNU-4.

Figure 2.9 shows the FE-SEM observation of the two YNU-4 zeolites (entry 3 and 9). Entry 3 consisted of needle-like particles with 300–1000 nm in length and about 100 nm in width (Figures 2.9a and 2.9b). On the other hand, entry 9 had elongated plate-like morphology with 500–1000 nm in length and 200–400 nm in width. Reported ***STO**-type zeolites such as NCL-1[9] and [Al]-SSZ-31[15] have also elongated morphologies. Particle sizes of YNU-4 decreased with decreasing the sizes of seed crystals.

2.3.3 Characterizations of YNU-4 zeolites

YNU-4 zeolites (entries 3 and 9) were thermally stable enough to maintain ***STO** framework structures after calcination at 600 °C. The nitrogen adsorption-desorption measurements of the both samples gave typical I-type isotherms as shown in Figure 2.10, promising the presence of micropores.

Physicochemical properties of YNU-4 are summarized in Table 2.3. The BET area (S_{BET}) and the external surface area (S_{ext}) increased with decreasing the particle sizes of YNU-4. In contrast, the micropore volumes (V_{micro}) did not show significant changes. The Si/Al molar ratios of entries 3 and 9 were 166 and 279, respectively.

The ^{27}Al DE MAS NMR spectrum of entry 9 (Figure 2.11) revealed the existence of 4-coordinated Al and the absence of 6-coordinated Al. It shows almost all of Al atoms in the sample are incorporated into YNU-4 framework structure.

The weight of occluded organic molecules of entry 9 was determined to 90.4 mg/g-silica by TG-DTA. Assuming the organics was totally attributed to $TMMA^+$ and one unit cell contained 28 T atoms per unit cell as well as ***STO** polymorph A, the number of $TMMA^+$ cations per unit cell is estimated to be 0.84, meaning almost one OSDA per unit cell. Similarly, the occluding $TMMA^+$ in entry 3 is found to be 0.82 cations per unit cell.

2.3.4 Conditions for successful synthesis using Si-beta-2

In order to clarify the crystallization conditions of YNU-4, detailed investigation was carried out as listed in Table 2.4. Raising synthetic temperature from 160 °C to 170 °C caused the formation of dense phase (entry 15). The decrease in the amount of seed crystals from 5wt% to 2wt% inhibited the crystallization of YNU-4, and none of crystalline phases appeared after at least 4 days (entry 16). The increase in input $Al(OH)_3/SiO_2$ molar ratios from 0.002 from 0.004 also inhibited the appearance of any crystalline phases, indicating $TMMA^+$ does not direct the crystallization of relatively low-silica ***STO**-type zeolites (entry 17). Decrease in $TMMA^+OH^-/SiO_2$ molar ratios from 0.20 to 0.10 led the formation of cristobalite although crystallization of a trace amount of YNU-4 was confirmed (entry 18). These results reveled the strict conditions for the crystallization of YNU-4.

2.3.5 Speculation about the role of the seed crystals

Considering the difference of crystallization periods and particle sizes, smaller seed crystals can probably induce more frequent nucleation of YNU-4. Structural similarity between ***BEA** and ***STO** is probably responsible for the clear relationship between the size of seed crystals and the nucleation rate of YNU-4. Figure 2.12 shows the framework structures of ***STO** and ***BEA**. Apparently, the both structures are similar, especially the topologies of colored plane areas are the same. It is speculated that the seed crystals are partially dissolved at the beginning of the hydrothermal treatment and the resultant fragment species which possess partial structures of ***STO** assists the crystallization of YNU-4. The rate of dissolution generally increases with decreasing particle sizes, and the small Si-beta crystals (Si-beta-1) may provide more common fragments that promote to construct the nuclei of YNU-4 crystals.

2.3.6. Effect of Al on the crystallization of YNU-4

In order to clarify the effect of Al on the crystallization, the synthesis was also carried out in pure-silica conditions (without $Al(OH)_3$). Figure 2.13 shows the crystallization of pure-silica YNU-4 with a time course using Si-beta-2 seed crystals. Interestingly, pure-silica YNU-5 (Si-YNU-4) was observed even after 38 h while the aluminum-containing YNU- 4 ([Al]-YNU-4) did not crystallize until at least 48 h (entry 6, Table 2). The relatively rapid crystallization can be explained by the unaffinity of the OSDA to the aluminum. Additionally, the XRD peaks of Si-YNU-4 indexing 100, 300 and 400 plane (Figure 2.13c) were extraordinary high, which indicated that the plate-like morphology spreading along with *b* and *c* axis. Figure 2.14 reveals the morphology and size of pure-silica YNU-4 particle. Elongated plate-like particles were observed with approximately 1 × 10 μm in size. The length of the plate was probably correspond to the length of 1D channel. Actually elongated plate or rod was typical morphology in zeolites with 1-dimensional channel system such as mordenite[23], SSZ-24[24] and CIT-5[25]. The thinness was probably reflected by (100) fault plane and the crystal growth along *a* axis would be difficult.

2.3.7 Effect of alkali cations on crystallization of YNU-4

Role of alkaline cations was also investigated. Figure 2.15 shows the results of the syntheses using LiOH, NaOH, KOH or CsOH as an alkaline source. The crystallization was 6 days long under pure-silica conditions. Interestingly, only NaOH gave fully crystallized YNU-4 (Figure 2.15b). LiOH did not promote crystallization and trace amount of BIK phase appeared (Figure 2.15a). KOH promoted crystallization of quartz which was not observed in NaOH system (Figure 2.15c). CsOH somehow led the crystallization of kenyaite (Figure 2.15d). Although the necessity of Na^+ still remains unclear, it indicated that the inorganic structure-direction should also play a crucial role on YNU-4 crystallization.

2.3.8 Investigation of other zeolite seed crystals for YNU-4

As described above, a pure-silica beta zeolite was found to be efficient as seed crystals for ***STO**-type zeolite in our study. The structural similarity between ***BEA** and ***STO** would contribute to promote the crystal nucleation. If that is the case, other zeolites possessing some common building

unit or some structural similarity with ***STO** should be candidates for the seed crystals for YNU-4.

Therefore, we focused on a CIT-1 zeolite with *mel* composite building unit that was common with YNU-4. (Figure 2.16) Since CIT-1 was synthesized only as boron-containing form, deboronated CIT-1 was used as seed crystals. Figure 2.17 shows the crystallization of YNU-4 with the aid of CIT-1. The synthesis temperature was 170 °C , the period was 4 days, the seed amount was 2wt% as SiO_2 other synthesis parameters were the same. YNU-4 was successfully obtained, but the seed crystals were still remained after the crystallization of YNU-4. Probably CIT-1 has relatively low dissolution rate compared to beta. The framework density of CON (FD_{Si} = 15.7 T/nm^3) is actually higher than that of ***BEA** (FD_{Si} = 15.3 T/nm^3).[26] Even so, we confirmed the fact that the nucleation of YNU-5 could be assisted by CIT-1 seed crystals.

Figure 2.18 shows FE-SEM images of the CIT-1 seed crystals and the YNU-5. Compared to YNU-5 obtained by beta, YNU-5 from CIT-1 possessed large particle sizes. Some crystals had twins.

2.4 Conclusion

Aluminum-containing YNU-4 zeolites with an ***STO** topology were firstly synthesized by using $TMMA^+$ and Si-beta as an OSDA and seed crystals, respectively. The size of seed crystals (Si-beta) strongly affects the crystallization kinetics as is confirmed by XRD and SEM. In terms of practical usage of YNU-4, this novel size-controllable ***STO**-type zeolite is a good candidate for highly shape solid-acid catalysts because balance the diffusion of molecule in micropores and the suppression of external surface reactions is especially important for one-dimensional zeolites to show both high activity and high shape-selectivity in catalytic reactions.

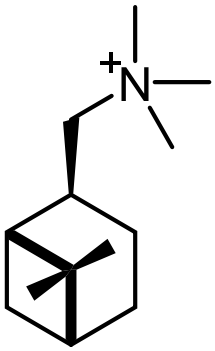

Figure 2.1. Skeletal chemical structure of trimethyl((-)-*cis*-myrtanyl)ammonium ($TMMA^+$).

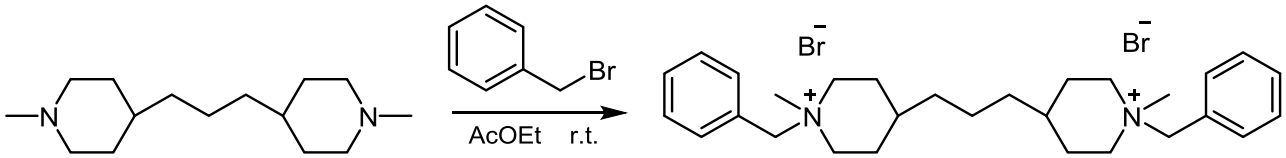

Figure 2.2. Preparation of 4,4'-trimethylenebis(1-benzyl-1-methylpiperidinium) dibromide.

Table 2.1. Synthesis of Si-beta with various particle sizes.

Entry	Synthetic conditions			Molar composition of synthesis mixture				Product	
	Temp. [°C]	Time [days]	Si [mmol]	SiO_2	$TMBP^{2+}(OH^-)_2$ [a]	H_2O	EtOH	Phases	Yield[b] [%]
Si-beta-1	100	16	15	1	0.175	36	none	***BEA**	100
Si-beta-2	135	8	50	1	0.150	39	none	***BEA**	97
Si-beta-3	150	5	30	1	0.150	46	4	***BEA** + trace **MTW**	106

[a] 4,4'-Trimethylenebis(1-benzyl-1-methylpiperidinium) dihydroxide.
[b] Mass of an as-synthesized product over that of SiO_2 in the synthesis mixture.

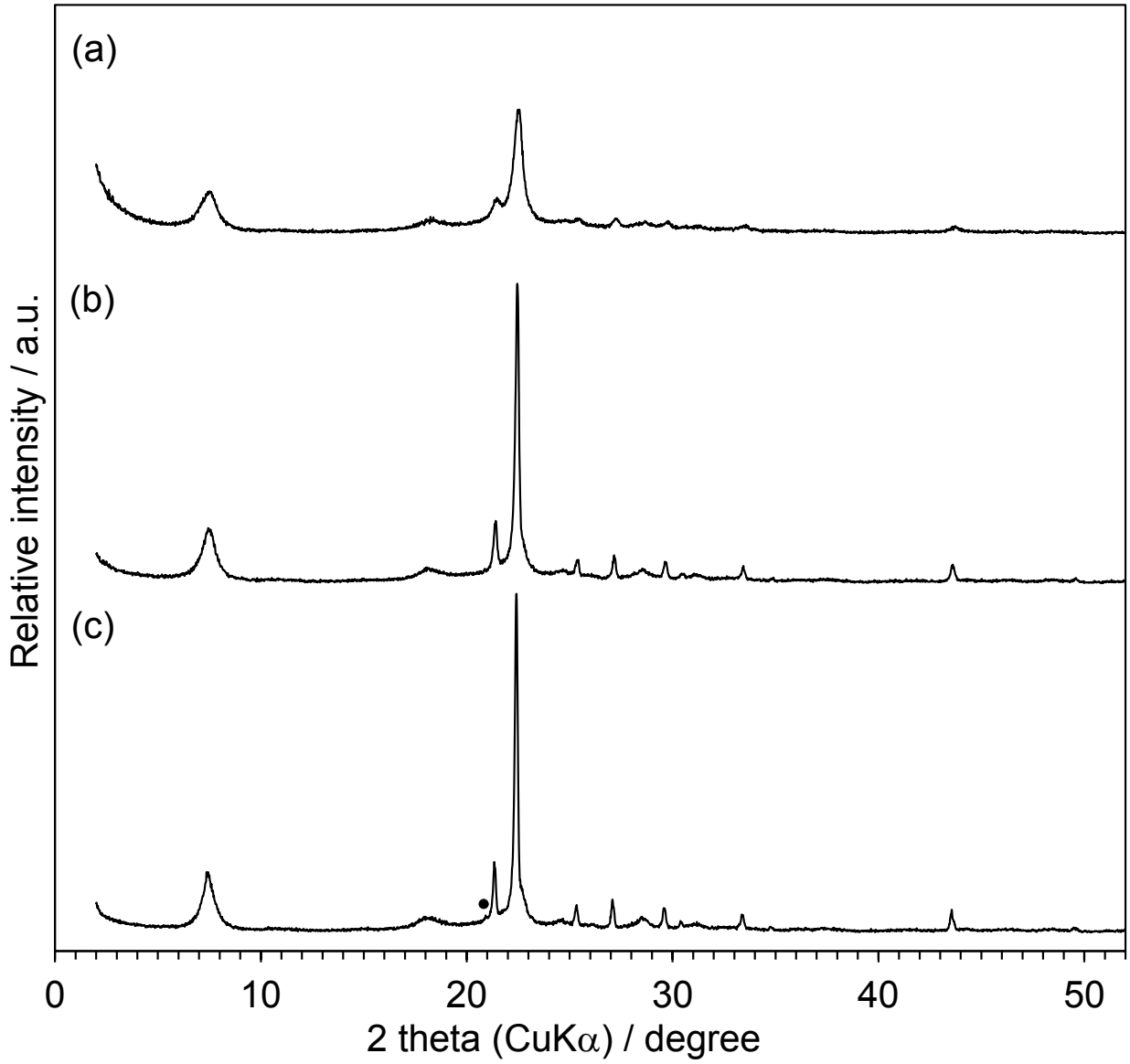

Figure 2.3. Powder XRD patterns of as-synthesized (a) Si-beta-1, (b) Si-beta-2 and (c) Si-beta-3, respectively. The detailed synthetic conditions are listed in Table 1. The symbol (●) refers to the peak attributable to an **MTW** phase.

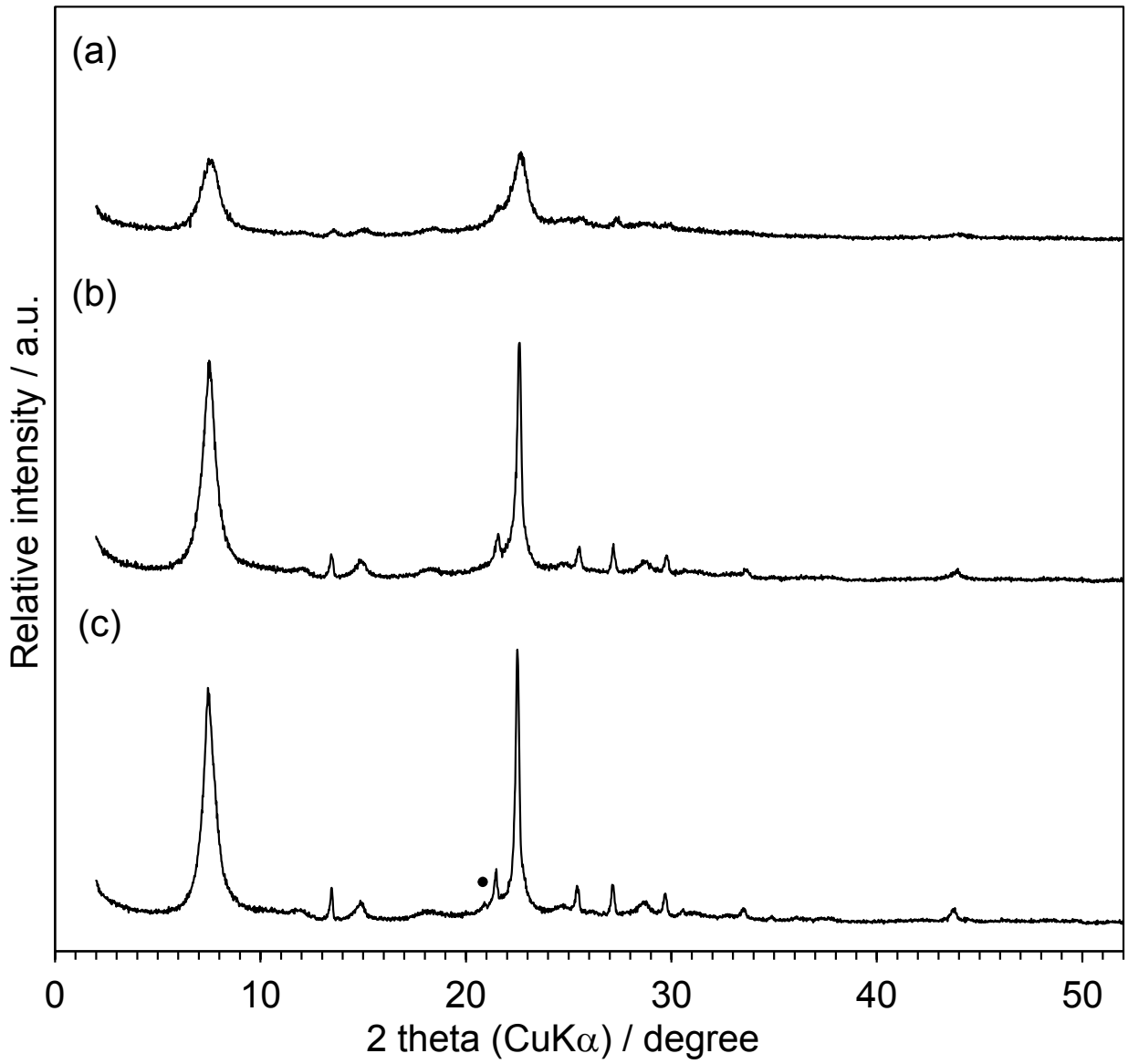

Figure 2.4. Powder XRD patterns of calcined (a) Si-beta-1, (b) Si-beta-2 and (c) Si-beta-3, respectively. The detailed synthetic conditions are listed in Table 1. The symbol (●) refers to the peak attributable to an **MTW** phase.

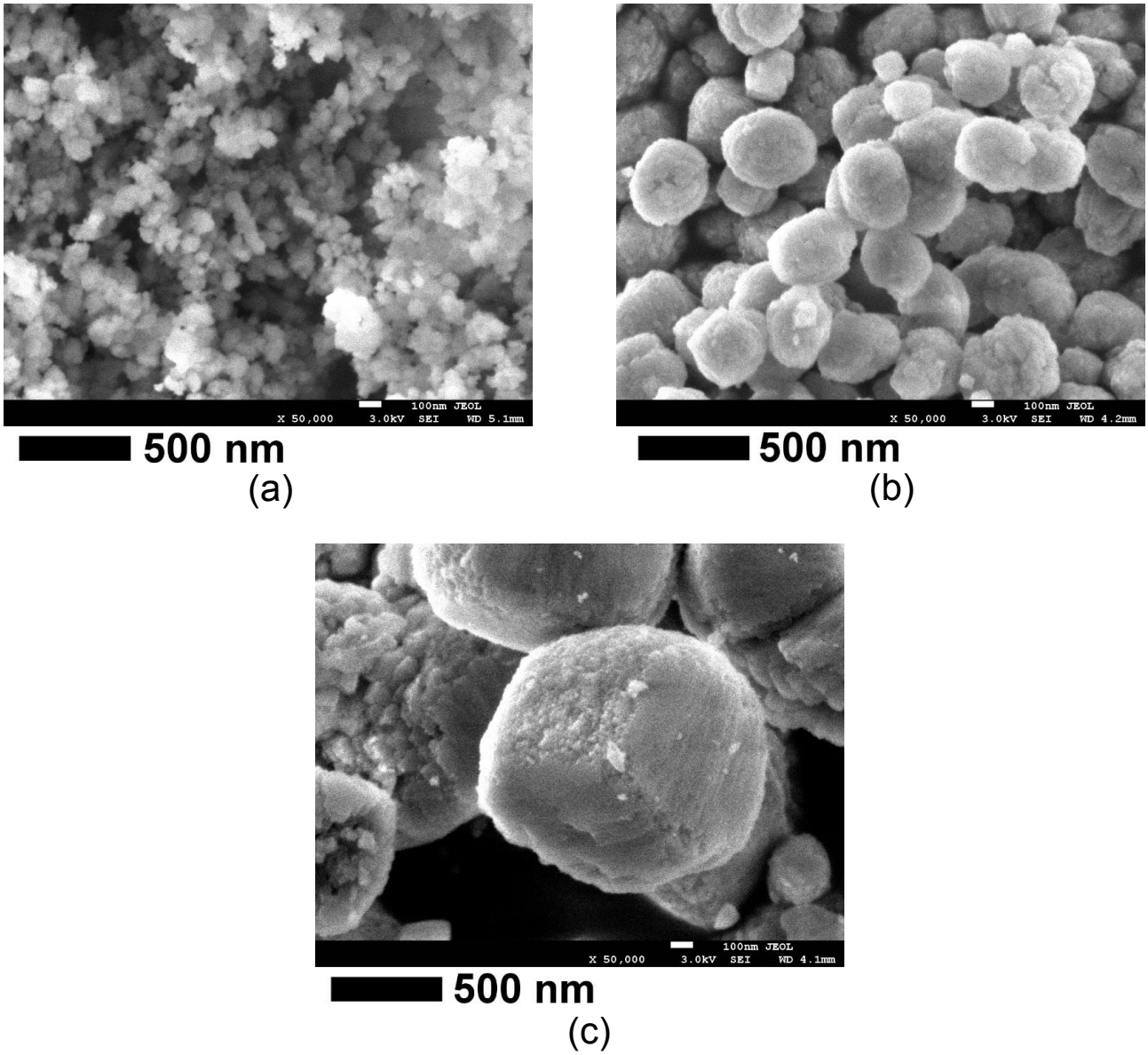

Figure 2.5. FE-SEM images of (a) Si-beta-1, (b) Si-beta-2 and (c) Si-beta-3, respectively. All images were taken at the same magnification.

Table 2.2. Synthesis of YNU-4 (***STO**) by using various calcined Si-beta as seed crystals.

Entry	Synthetic conditions[a]		Product	
	Seed[b] (particle size)	Time [h]	Phases	Yield[c] [%]
1	none	92	amor.	43
2	Si-beta-1 (50−100 nm)	22	amor. + ***BEA**(seed)	41
3		44	***STO**	43
4		68	cristobalite + ***STO**	48
5	Si-beta-2 (300−500 nm)	24	amor. + ***BEA**(seed)	43
6		48	amor. + ***BEA**(seed)	41
7		74	amor. + ***STO** + ***BEA**(seed)	42
8		94	***STO**	49
9		138	cristobalite + unknown dense	56
10	Si-beta-3 (800−1200 nm)	24	amor. + ***BEA**(seed)	44
11		48	amor. + ***BEA**(seed)	51
12		72	amor. + ***BEA**(seed)	49
13		94	amor. + ***STO** + kenyaite	56
14		138	kenyaite	74

[a] Composition of synthesis mixtures are 1.0 SiO_2−0.002 $Al(OH)_3$−0.20 $TMMA^+OH^-$−0.20 NaOH−44 H_2O. All hydrothermal treatments were carried out at 160 °C. 5wt% of SiO_2 came from seed crystals and 95wt% came from Cab-O-Sil M5.

[b] Detailed synthetic conditions of seed crystals are described in Table 5.1. Particle sizes are estimated by FE-SEM observations.

[c] Mass of an as-synthesized product over that of SiO_2 in the synthesis mixture.

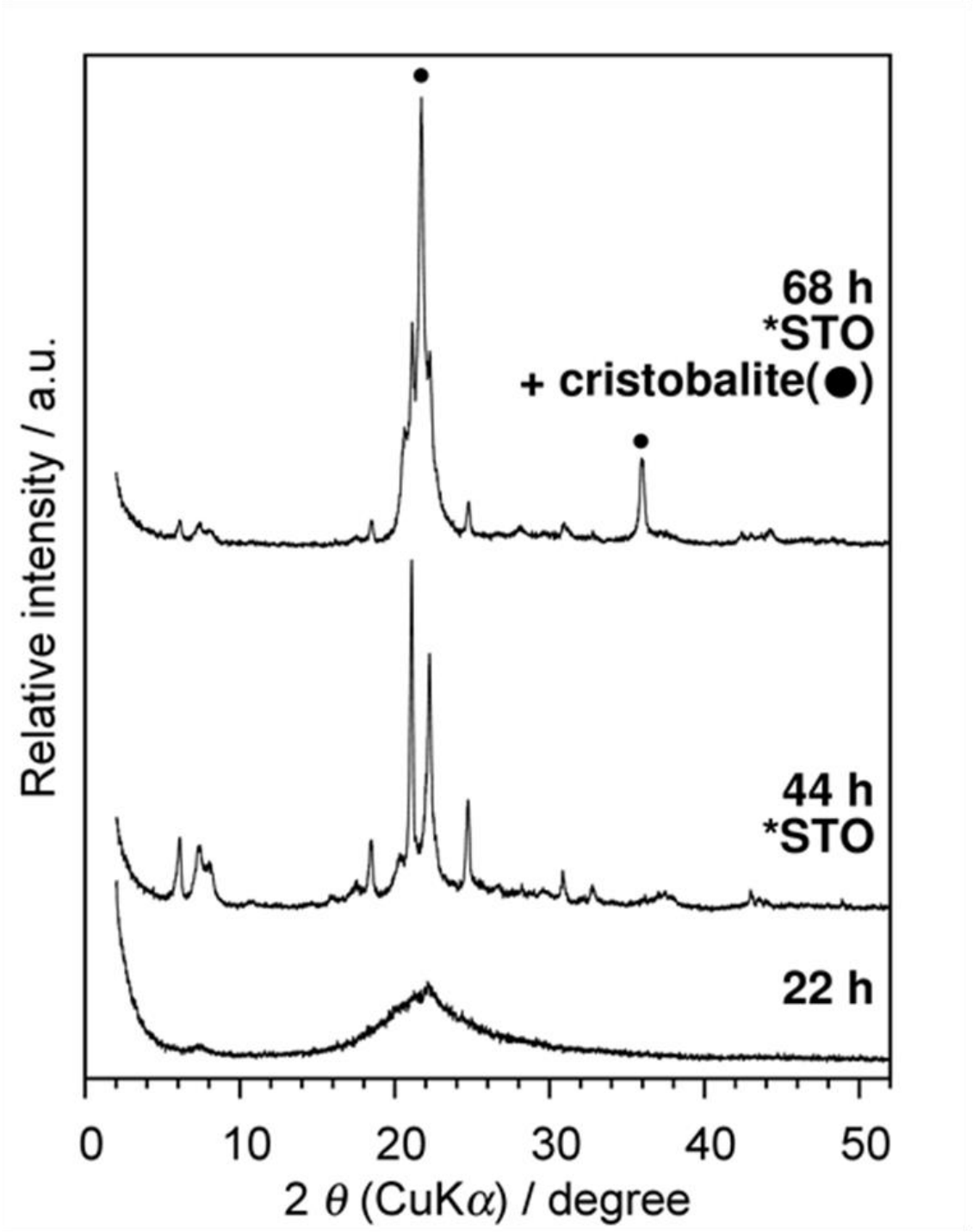

Figure 2.6. Phase change with time course as reflected in the powder XRD patterns of the as-synthesized samples; The used seed is calcined Si-beta with less than 100 nm in diameter (entry 1 in Table 2.1). The symbols (●) refer to the peaks attributable to a cristobalite phase.

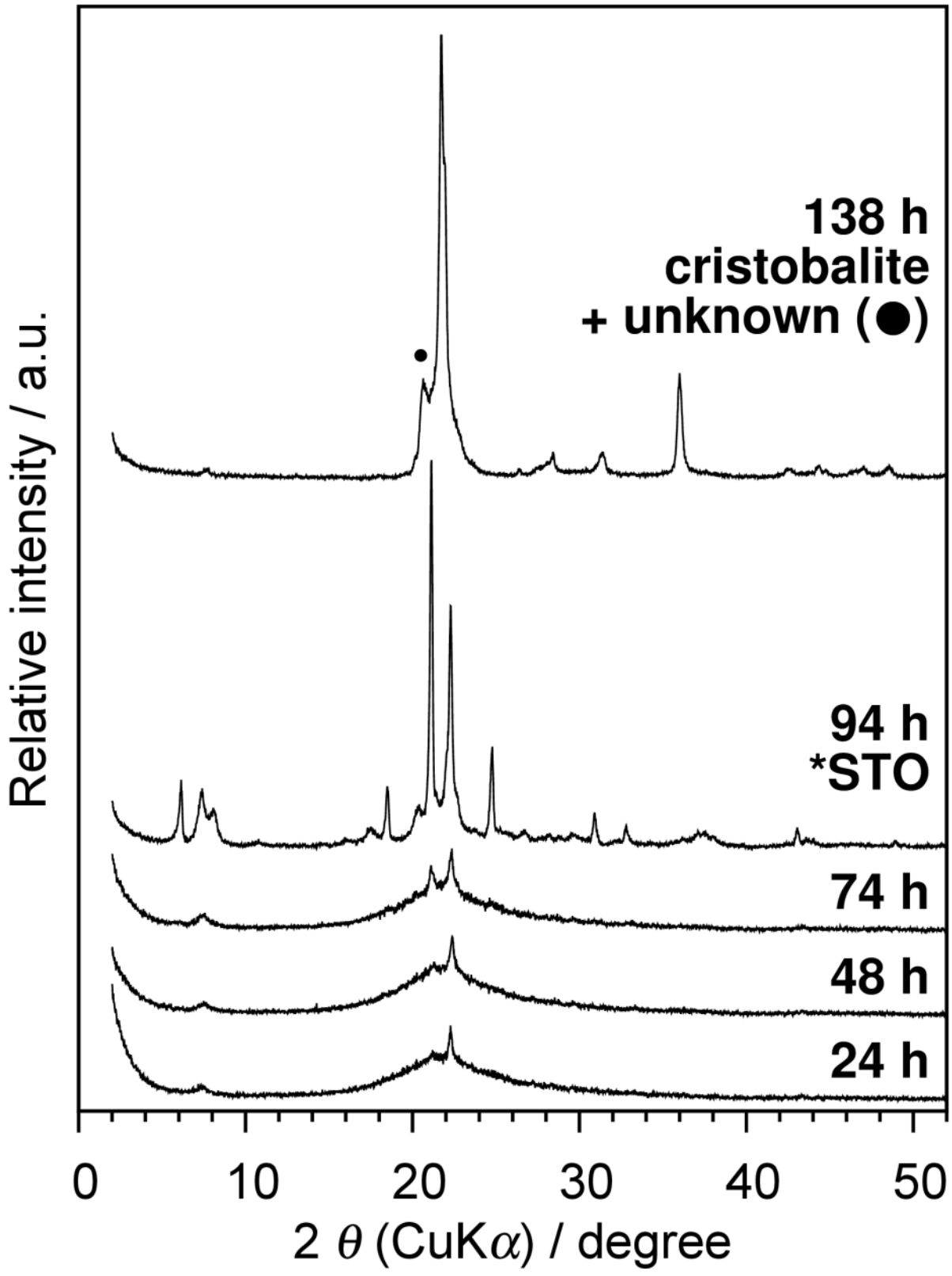

Figure 2.7. Phase change with time course as reflected in the powder XRD patterns of the as-synthesized samples; The used seed is calcined Si-beta with 300−500 nm in diameter (sample 2 in Table 1). The symbol (●) refers to the peaks attributable to an unknown phase.

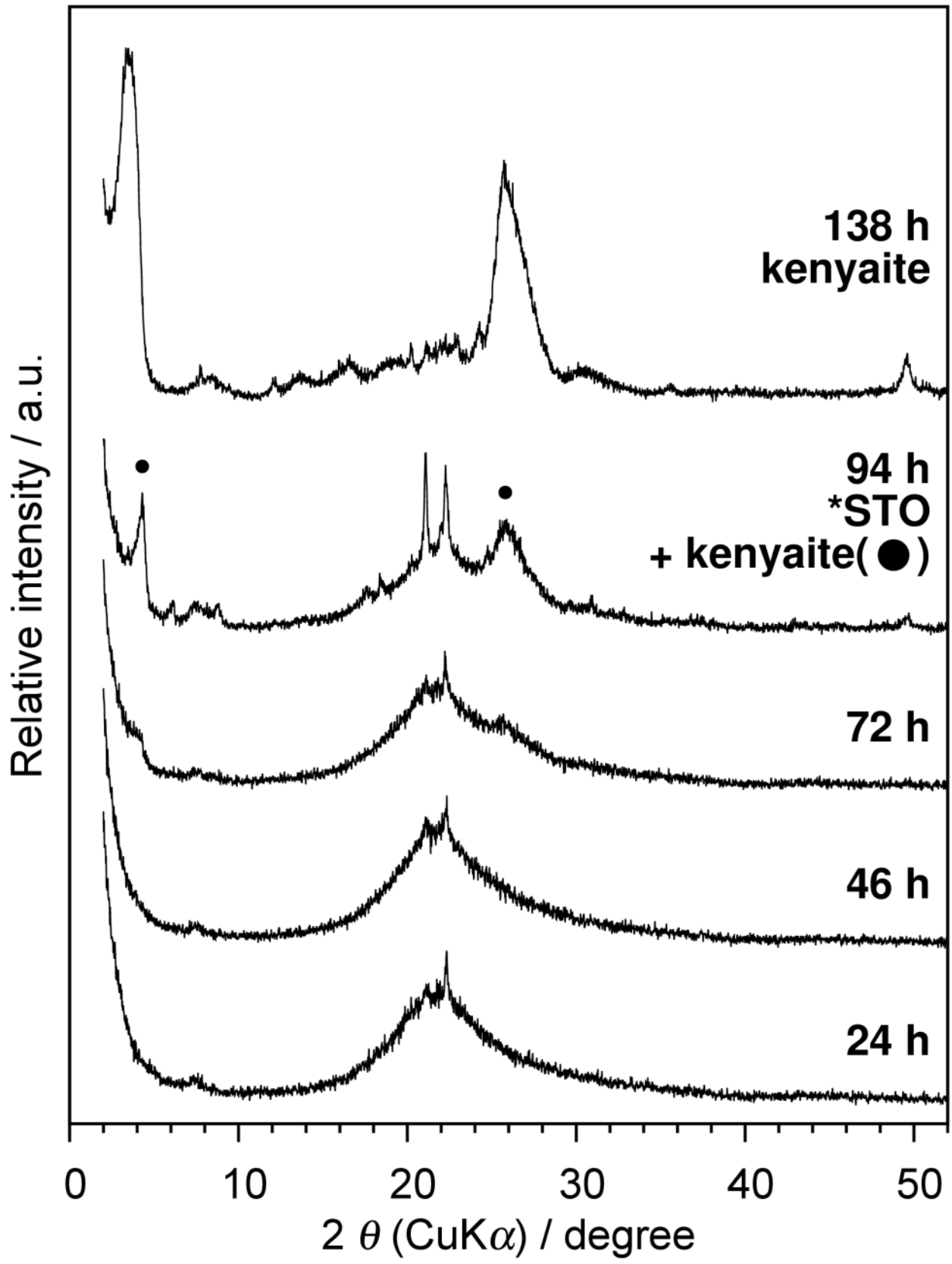

Figure 2.8. Phase change with time course as reflected in the powder XRD patterns of the as-synthesized samples; The used seed is calcined Si-beta with about 1 μm in diameter (sample 3 in Table 1). The symbols (●) refer to the peaks attributable to a kenyaite phase.

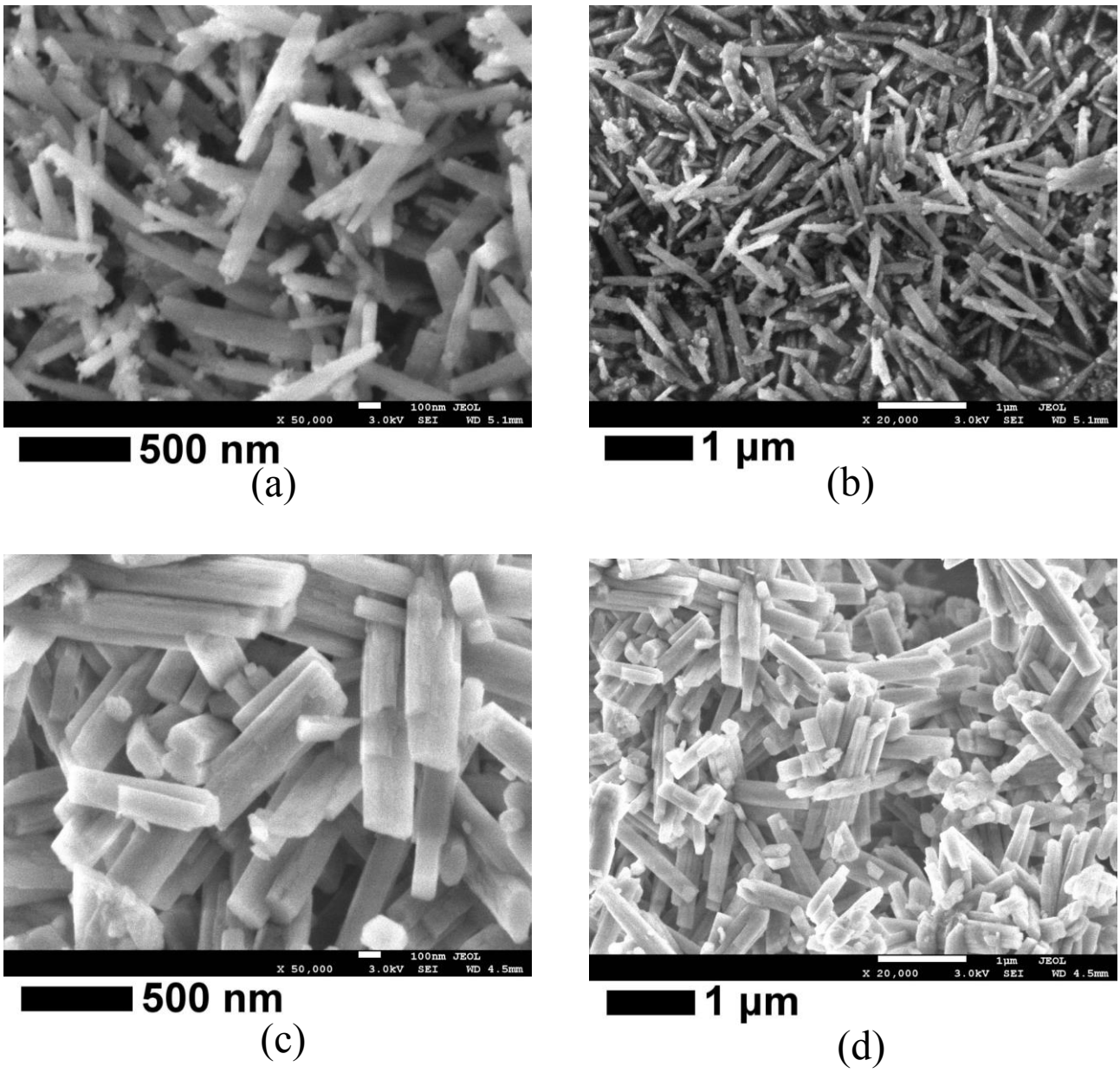

Figure 2.9. FE-SEM images of YNU-4 ; entry 3 and (c, d) entry 8 in Table 2.2, respectively.

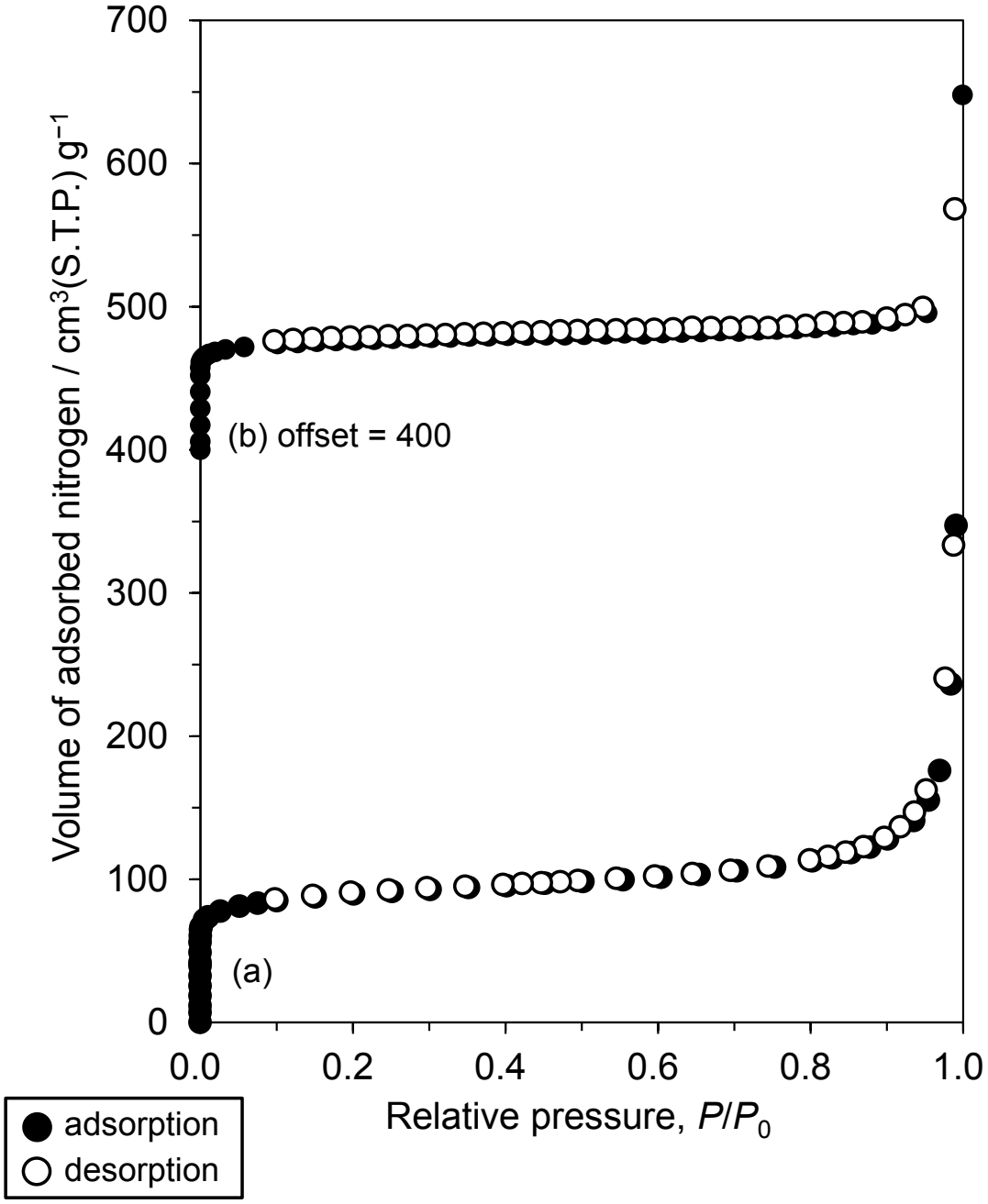

Figure 2.10. Nitrogen adsorption-desorption isotherms of YNU-4. (a) entry 3 and (b) entry 8, respectively.

Table 2.3. Physicochemical properties of YNU-4 zeolites.

Entry[a]	Si/Al[b]	S_{BET}[c] [m^2/g]	S_{ext}[d] [m^2/g]	V_{micro}[e] [cm^3/g]	Particle size[f] [nm] (length × width)
3	166	335	63.4	0.113	(300−1000) × 100
8	279	267	17.9	0.114	(500−1000) × (200−400)

[a]The crystallization conditions are described in Table 2.2. [b]Estimated by ICP-AES. [c]BET area estimated on the basis of nitrogen adsorption isotherms. [d]External surface area estimated by the *t*-plot method. [e]Micropore volume estimated by the *t*-plot method. [f]Estimated by FE-SEM observation.

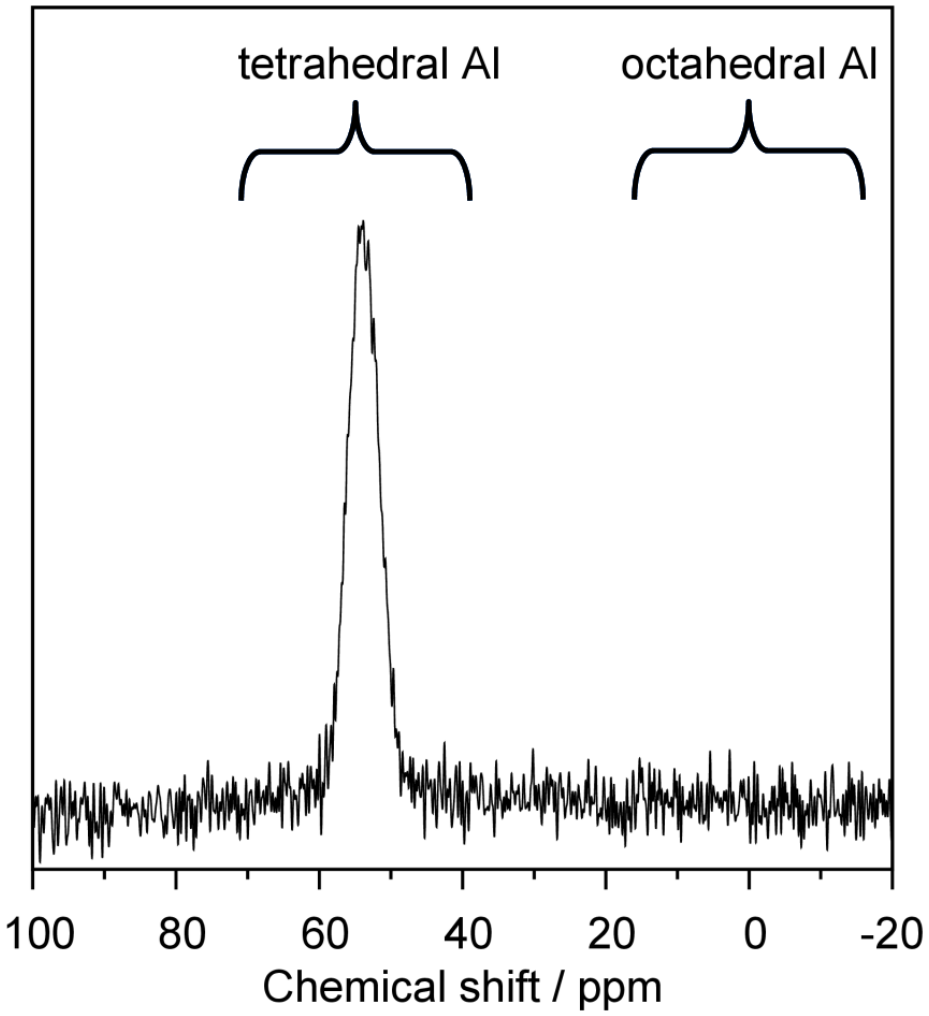

Figure 2.11. ^{27}Al DE MAS NMR spectrum of as-synthesized YNU-4 (entry 8).

Table 2.4. Investigation of the crystallization conditions for YNU-4 using Si-beta-2.

Entry	Synthetic conditions[a]			Molar composition of synthesis mixture			Product phases
	Temp. [°C]	Time [days]	Seed [wt%]	SiO_2	$Al(OH)_3$	$TMMA^+OH^-$	
8	160	4	5	1	0.002	0.20	***STO**
15	170	4	5	1	0.002	0.20	dense + ***STO**
16	160	4	2	1	0.002	0.20	amor. + beta(seed)
17	160	7	5	1	0.004	0.20	amor. + beta(seed)
18	160	5	5	1	0.002	0.10	dense + trace ***STO**

[a] Other composition of synthesis mixtures are 1.0 SiO_2−0.20 NaOH−44 H_2O. SiO_2 came from seed crystals and Cab-O-Sil M5. The used seed crystals were Si-beta-2. Detailed synthetic conditions of seed crystals are described in Table 2.1.

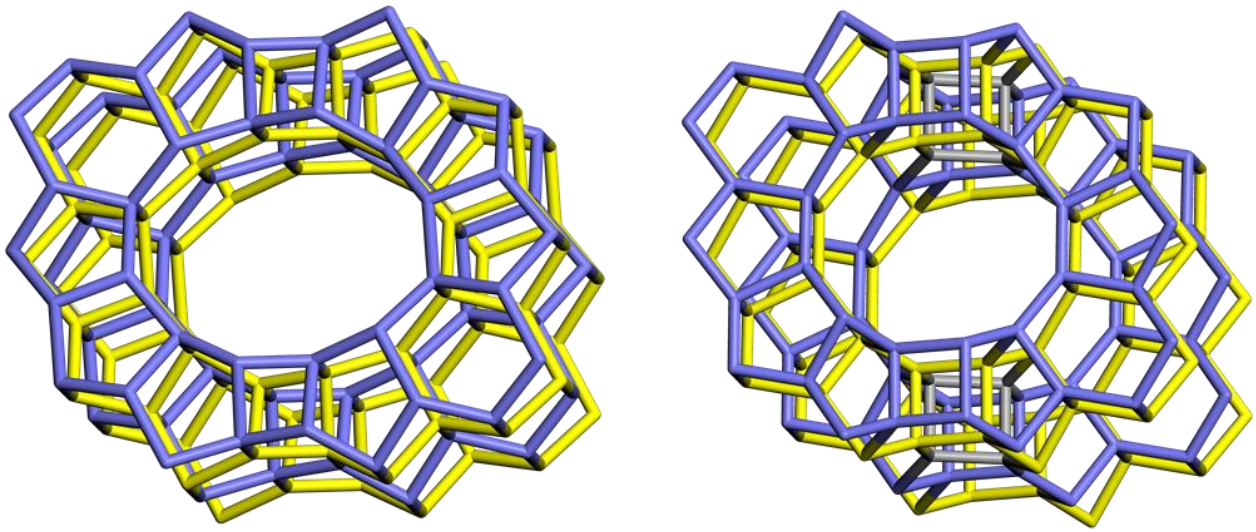

Figure 2.12. (a) ***STO** polymorph A viewed along [010] and (b) ***BEA** polymorph B viewed along [110]. Although there was no common composite building units, topologies of the plane structures (colored area) are similar.

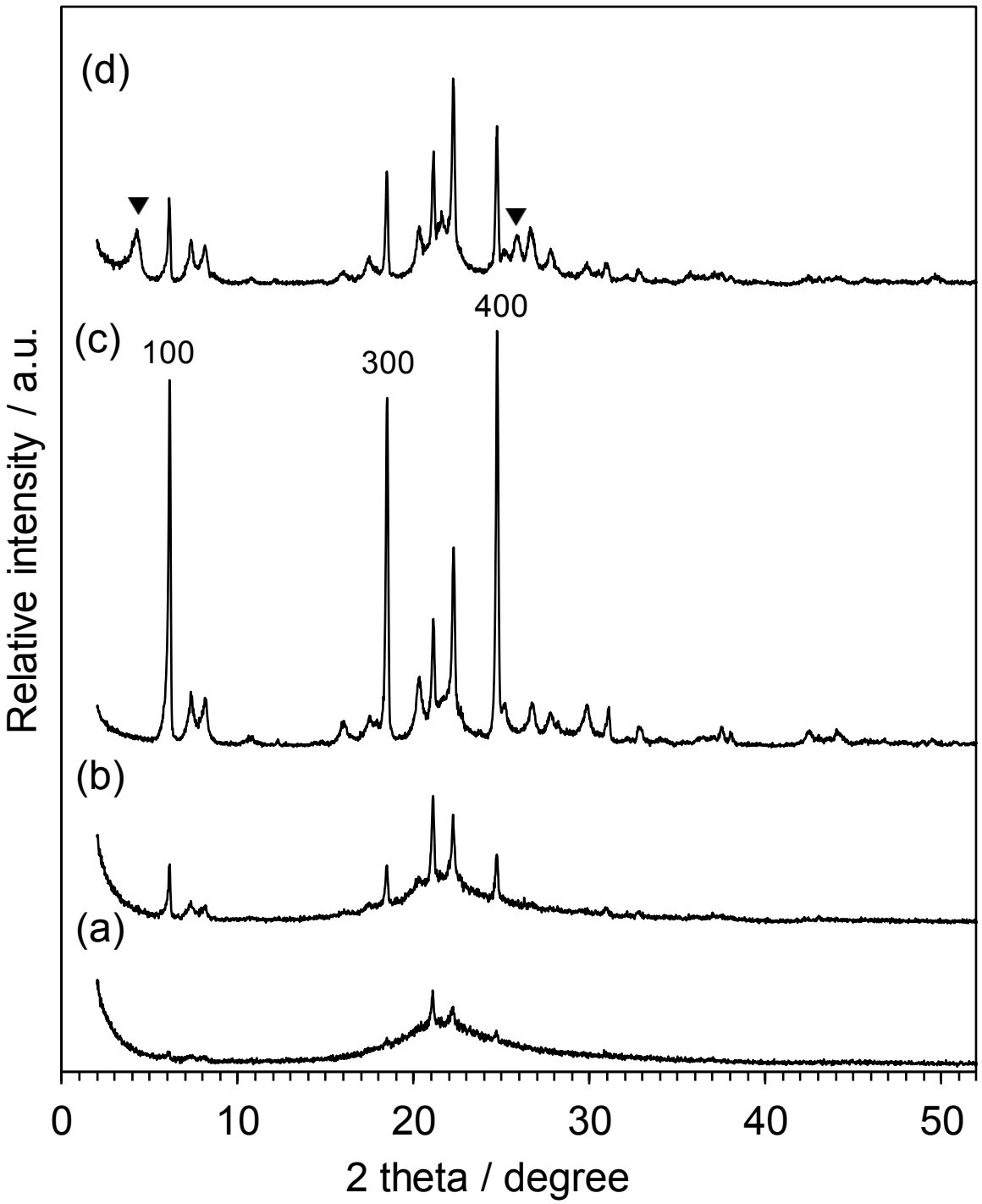

Figure 2.13. Crystallization of pure-silica YNU-4 with time-course with the aid of Si-beta-2 seed crystals. Synthesis period were (a) 38, (b) 63, (c) 89 and (d) 139 h, respectively.

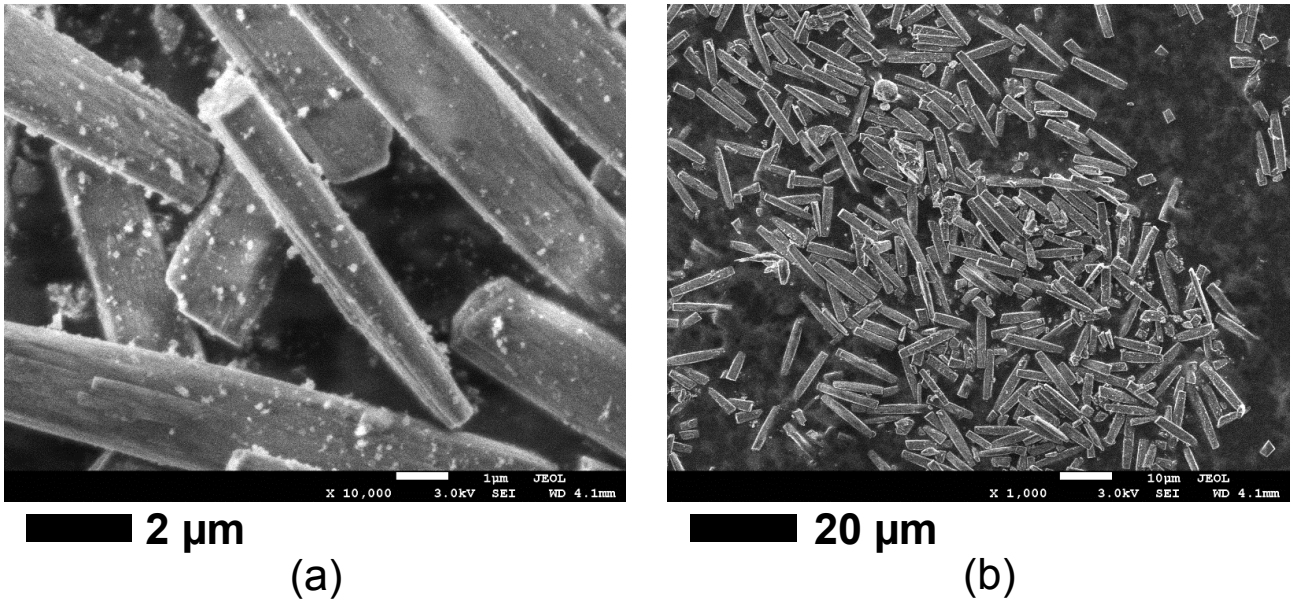

Figure 2.14. FE-SEM images of Si-YNU-4 in (a) high and (b) low magnifications, respectively.

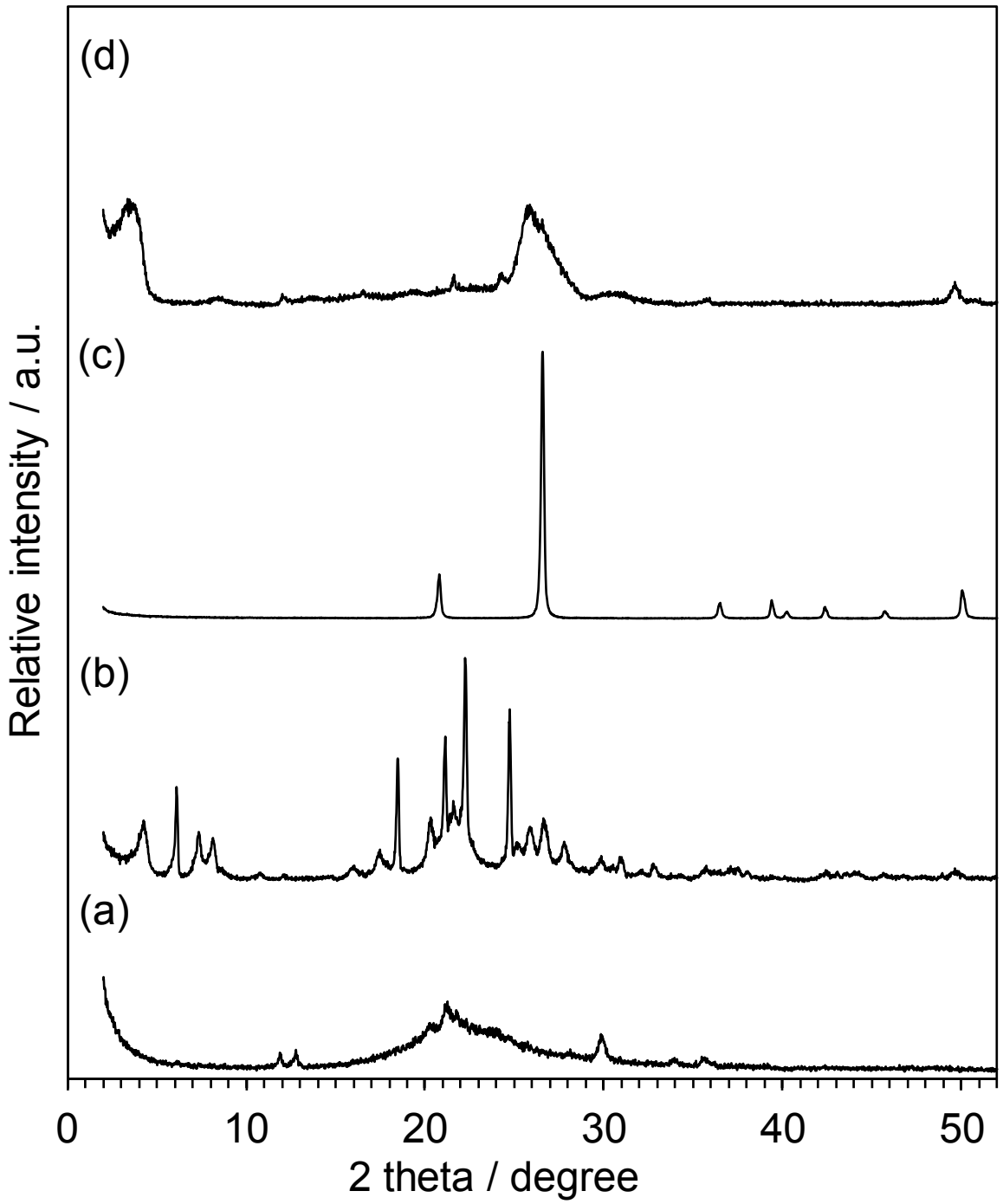

Figure 2.15. Effects of alkaline cations on the crystallization of Si-YNU-4. XRD patterns of the solid product obtained using (a) LiON, (b) NaOH, (c) KOH and (d) CsOH, respectively.

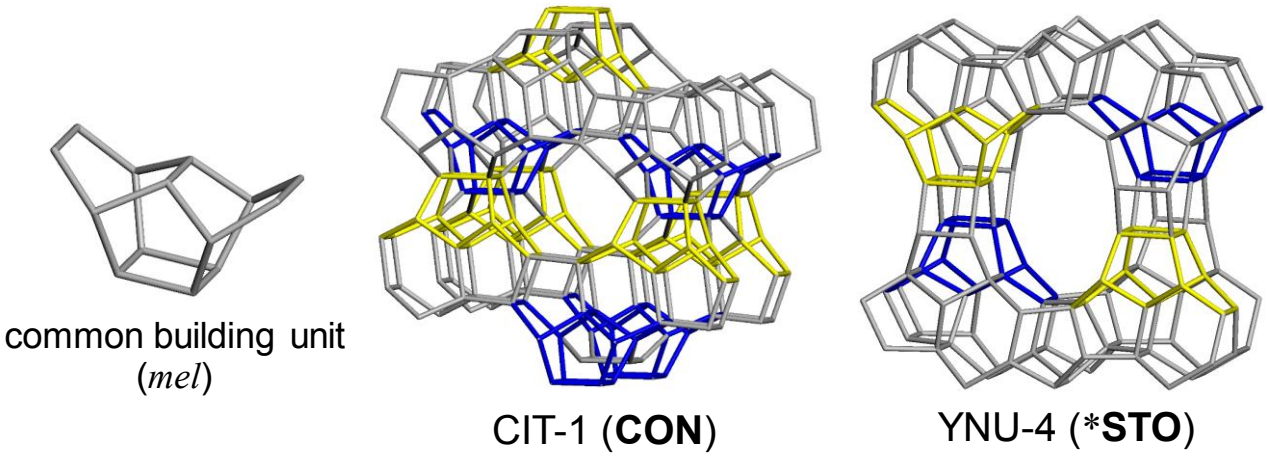

Figure 2.16. Common building unit (*mel*) between CIT-1 with **CON** topology and YNU-4 with ***STO** topology.

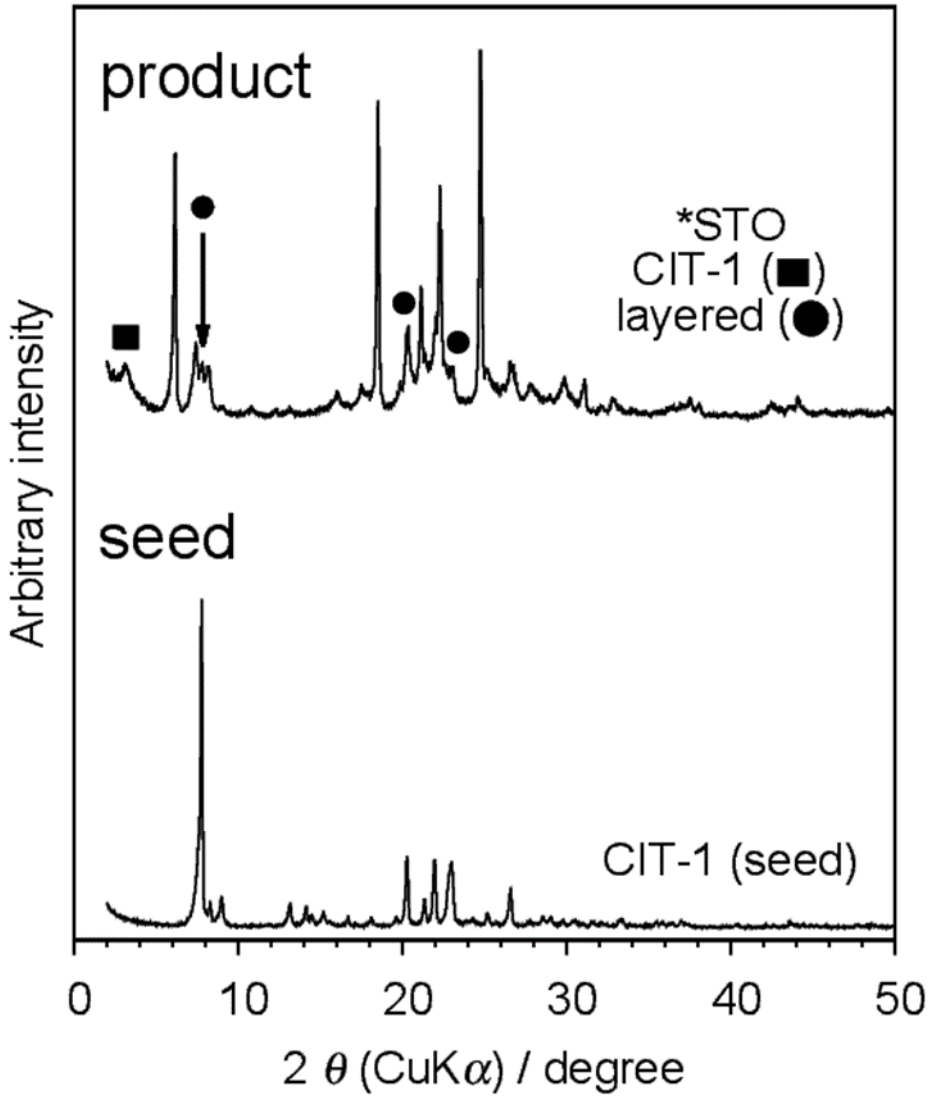

Figure 2.17. XRD patterns of CIT-1 crystals.

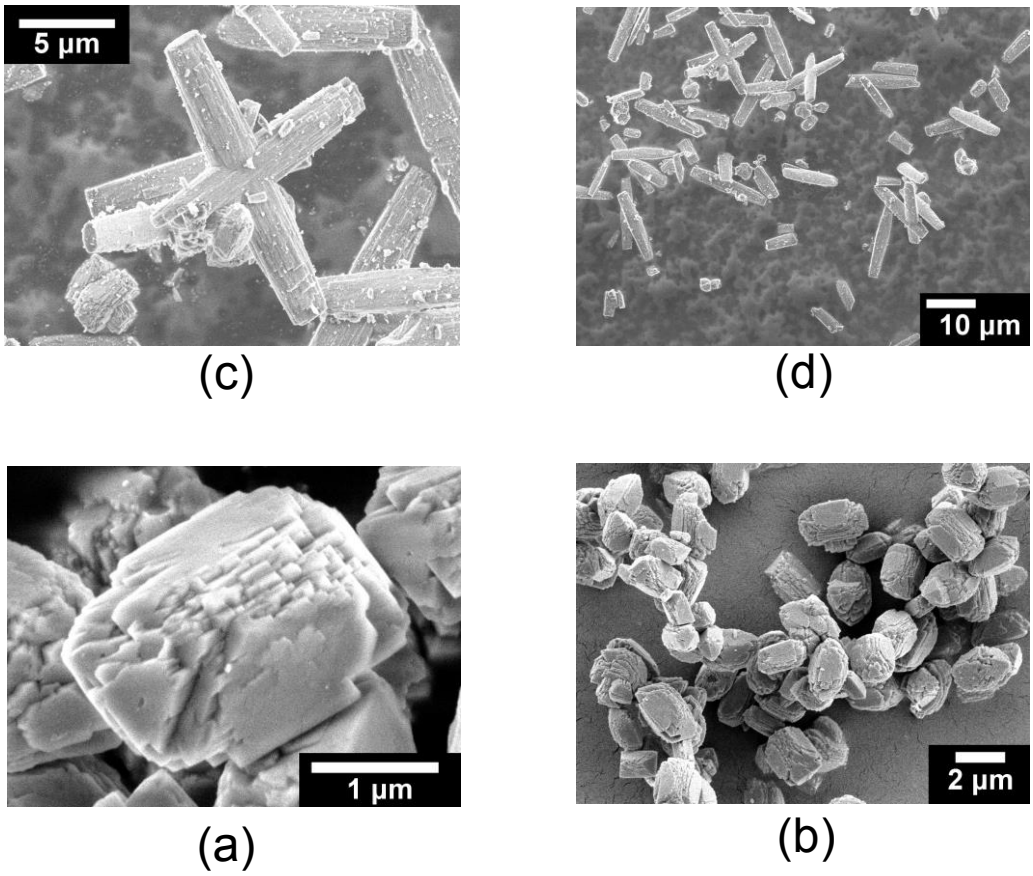

Figure 2.18. FE-SEM images of (a, b) deboronated CIT-1 seed crsytals and (c, d) YNU-4 synthesized by using deboronated CIT-1 as seed crystals, respectively.

2.5. References

1) M.E. Davis, R.F. Lobo, *Chem. Mater*., **4**, 756 (1992).

2) R.F. Lobo, S.I. Zones, M.E. Davis, *J. Incl. Phenom. Mol. Recognit. Chem.*, **21**, 47 (1995).

3) R.F. Lobo, M.E. Davis, *J. Am. Chem. Soc.*, **117**, 3766 (1995).

4) G. Majano, A. Darwiche, S. Mintova, V. Valtchev, *Ind. Eng. Chem. Res.*, **48**, 7084 (2009).

5) B. Xie, J. Song, L. Ren, Y. Ji, J. Li, F.S. Xiao. *Chem. Mater.*, **20**, 4533 (2008).

6) Y. Kubota, K. Itabashi, S. Inagaki, Y. Nishita, R. Komatsu, Y. Tsuboi, S. Shinoda, T. Okubo, *Chem. Mater.*, **26**, 1250 (2014).

7) K Iyoki, Y. Kamimura, K. Itabashi, A. Shimojima, T. Okubo, *Chem. Lett.*, **39**, 730 (2010).

8) H. Imai, N. Hayashida, T. Yokoi, T. Tatsumi, *Micropor. Mesopor. Mater.*, **196**, 341 (2014).

9) R.F. Lobo, M. Tsapatsis, C.C. Freyhardt, I. Chan, C.Y. Chen, S.I. Zones, M.E. Davis, *J. Am. Chem. Soc.*, **119**, 3732 (1997).

10) H.V. Koningsveld, R.F. Lobo, *J. Phys. Chem. B*, **107**, 10983 (2003).

11) S.I. Zones, T.V. Harris, A. Rainis, D.S. Santilli, *US Patent*, 5,106,801 (1992).

12) K.R. Reddy, V. Ramaswamy, R. Kumar, and A.V. Ramaswamy., *Zeolites*, **14**, 326 (1994).

13) P.R.H.P. Rao, K. Ueyama, E. Kikuchi, M. Matsukata, *Chem. Lett.*, **27**, 311 (1998).

14) R.K. Ahedi, Y. Kubota, Y. Sugi, *J. Mater. Chem.*, **11**, 2922 (2001).

15) R.K. Ahedi, Y. Kubota, Pusparatu, Y. Sugi, *Bull. Chem. Soc. Jpn.*, **76**, 883 (2003).

16) R.K. Ahedi, S. Tawada, Y. Kubota, Y. Sugi, J.H. Kim, *J. Mol. Cat. A*: *Chem*., **197**, 133 (2003).

17) M. Yoshioka, T. Yokoi, T. Tatsumi, ACS Catal. **5**, 4268 (2015).

18) K. Tsuji, M.E. Davis, *Micropor. Mater.*, **11**, 53 (1997).

19) K. Tsuji, L.W. Beck, M.E. Davis, *Micropor. Mesopor. Mater.*, **28**, 519 (1999).

20) O. Larlus, S. Mintova, S.T. Wilson, R.R. Willis, H. Abrevaya, T. Bein, *Micropor. Mesopor. Mater.*, **142**, 17 (2011).

21) R. Bandyopadhyay, Y. Kubota, N. Sugimoto, Y. Fukushima, Y. Sugi, Micropor. Mesopor. Materl. **32**, 81 (1999).

22) T. Mathew, S.P. Elangovan, T. Yokoi, T. Tatsumi, M. Ogura, Y. Kubota, A. Shimojima. T. Okubo, *Micropor. Mesopor. Mater.*, **129**, 126 (2010).

23) L. Zhang, S. Xie. W. Xin, X. Li, S. Liu, L. Xu, *Mater. Res. Bull.*, **46**, 894 (2011).

24) R.F. Lobo, M.E. Davis, *Micropor. Mater.*, **3**, 61 (1994).

25) Y. Kubota, S. Tawada, K. Nakagawa, H. Naitoh, N. Sugimoto, Y. Fukushima, T. Hanaoka, Y. Imada, Y. Sugi, *Micropor. Mesopor. Mater.*, **37**, 291 (2000).

26) International Zeolite Association, http://www.iza-structure.org/databases/

Chapter Three

高シリカSSZ-39の直接合成

Direct hydrothermal synthesis of high-silica SSZ-39 zeolites

*High-silica SSZ-39 zeolite tiny crystals with a Si/Al molar ratio as high as 16 have been directly synthesized. Tuning both alkali and water contents in the synthesis mixture followed by using relatively high-silica **FAU** crystals is essential for the single-phase crystallization. Our novel SSZ-39 could be a powerful candidate for the environmentally-benign catalyst for claimed resources conversion and gas purification.*

3.1 Introduction

Zeolites are microporous crystalline aluminosilicates and usually synthesized in hydrothermal alkaline media with or without the aid of organic structure-directing agents (OSDAs). Besides usage of silicates and aluminates, the use of zeolites as starting materials has widely been applied to obtain novel types of zeolitic materials. For instance, the syntheses of [Al]-SSZ-31 and [Al]-SSZ-24 were firstly made possible by using [Al]-beta as starting materials.[1,2] The hydrothermal conversion of an **FAU**-type zeolite gave ***BEA**,[3] **RUT**,[4] **CHA**[5] and **MSE**-type zeolites.[6] The use of zeolites as seed crystals enabled OSDA-free syntheses[7] of ***BEA**,[8,9] **MTW**,[10,11] **MSE**,[9] **CHA**,[12] and **NES**-type zeolites.[13]

SSZ-39 is an aluminosilicate zeolite with an **AEI** framework which consists of *d6r* composite building units.[14,15] The structure is featured by small pore-windows with 0.38 × 0.38 nm in diameter and large cages (**AEI** cage) with around 0.85 × 0.99 nm in size. (Figure 3.1) SSZ-39 currently attracts considerable attention since Cu-SSZ-39 is reported to be highly active and hydrothermally stable in the selective catalytic reduction (SCR) of NOx.[16] Cu-SSZ-39 was also reported to be potentially active in the conversion of methane to methanol.[17] Most recent report of the application of H-SSZ-39 in methanol-to-olefin (MTO) reaction includes the detailed investigation an effect of steaming conditions on the catalytic properties.[18]

In order to tune adsorptive or catalytic properties of zeolites, the contents of Al that directly affects to an affinity to guest molecules in the micropores should be controlled as freely as possible. Especially for the utilization as solid acid catalysts, the high-silica composition is generally desired from the viewpoints of hydrothermal stability and resistance to coke-formation. In the case of SSZ-39, however, the Si/Al molar ratios were limited to 6–10 when using 1,1,3,5-tetramethylpiperidinium

(TMP^+) as an OSDA (Figure 3.2).[16,18,19] High-silica SSZ-39 with Si/Al as high as 26.5 was obtained by using 9,9-dimethyl-9-azoniabicyclo[3.3.1]nonane (Figure 1b),[20,21] which is much more expensive and difficult to prepare than TMP^+. The syntheses of high-silica **AEI**-type zeolites via a hydroxide route (Si/Al = 16.2) and via a fluoride-assisted route (Si/Al = 20.6) have been recently established using tetraethylphosphonium as an OSDA; however, the P species inside the cages cannot be completely removed.[22,23]

Control of particle sizes has also been required to apply zeolites in adsorptive and catalytic processes. Zeolite nanocrystals are especially favored because they take advantage of fewer diffusion limitations of molecules to promise enhanced activity and prevent undesirable consecutive reactions. Accordingly, a series of nanocrystalline zeolites have been synthesized and their applications have been widely investigated.[24–33]

In such a situation, we have successfully synthesized high-silica SSZ-39 nanocrystals with Si/Al as high as 16.4 using relatively inexpensive TMP^+ as an OSDA.

A **GME**-type zeolite is of great interest due to its unique 12−8−8R channel system.[15] The 12R channels are straight and the pore diameter is approximately 0.70 × 0.70 nm (Figure 3.9).[15] They are connected by 8R channels with 0.36 × 0.39 nm windows (Figure 3.10).[15] 8R channels consist of **GME** cages with 0.32 × 0.73 nm.

A **GME**-type zeolite occurs naturally as **gmelinite**.[36] Its 12R channels are, however, blocked by intergrowth with chabazite with **CHA** topology.[36] Fault-free **gmelinite** was synthesized in 1978 using polymeric Dab-4Br (Figure 3.11),[37] but it was obtained only as an as-synthesized form (occluding organics) and calcination led to convert to an **AFI** phase.[37] Ion exchange of as-synthesized sample with K^+ was known to suppress the conversion at the high temperature.[38] Another synthetic **GME**-type zeolite was reported in 1991, where tetraethylammonium bromide was used as an OSDA.[39] The sample contained an impurity **ANA** phase and prolonged hydrothermal treatment led to convert of **GME** into **ANA** hydrothermally. **Gmelinite** was also synthesized by hydrothermal conversion of **FAU**-type zeolites exchanged with Sr^{2+}.[40] **FAU**-type zeolites with other alkaline-earth cations (Ca^{2+} or Ba^{2+}) did not give **gmelinite**.[40]

Generally one OSDA can give several zeolites with different topologies. In the syntheses using TMP^+, SSZ-39 crystallized in relatively aluminum-rich conditions.[41] ZSM-5, ZSM-5/11 and ZSM-12 were obtained in relatively high-silica conditions.[41] SSZ-35 crystallized in borosilicate media.[41] Other synthetic parameters such as aging conditions, starting materials, alkali contents, concentration of synthesis mixture and synthetic temperature generally influence on the phase selectivity. Designing appropriate synthetic system is therefore quite important to draw capability of an OSDA. In other word, novel designed syntheses will provide new zeolites even if the OSDA is already known.

A **GME**-type zeolites is a low-silica aluminosilicate, comprising of *d6r* building unit (Figure 3.13)

and have large 12R pores. These features are quite similar to well-known Y zeolites with **FAU** topology. USY, which is a high-silica **FAU**-type zeolite prepared by repeated steaming and acid treatment of Y, is extensively applied in fluid catalytic cracking (FCC) processes.[42−48] Although many *d6r*-based zeolites were not able to be dealuminated by post-treatment due to their small pore sizes, the **GME**-type zeolites have large 12R pores where diffusion of aluminum species removed from the zeolite frameworks can take place. **GME** is one of the three large-pore zeolite frameworks constructed by *d6r* building units as well as **FAU** and **EMT**. Post-treated **GME** zeolites have considerable potentials for application in FCC as well as other processes catalyzed by acid catalysts.

Synthesis of a novel **GME-type** zeolite using diastereomeric mixture of 1,1,3,5-tetramethylpiperidinium hydroxide (TMP^+OH^-) is firstly reported in this work. A new technique to prevent **GME→AFI** transformation is also provided.

3.2 Experimental

3.2.1 Preparation of *cis*- and *trans*- mixture of 1,1,3,5-tetramethylpiperidinium hydroxide

TMP^+OH^-, 1,1,3,5-tetramethylpiperidinium hydroxide was prepared as follows. K_2CO_3 (74 g, 554 mmol) were added into methanol (300 mL) and then 3,5-dimethylpiperidine (mixture of *cis*- and *trans*-, 51.5 mL, 43.0 g, 365 mmol, >96%, TCI) were added. The mixture was stirred for 10 min at room temperature. Methyl iodide (68.5 mL, 155 g, 1094 mmol) were added dropwise 10 min and the whole mixture was stirred for 186 h. Chloroform (175 mL) were added to the white suspension and stirred for another 1 h. Inorganic salts were removed by filtration and the product was extracted with chloroform (200 mL). The filtrate was dried by evaporator and the resultant solid was filtered and extracted with chloroform again. This procedure was repeated until undissolved inorganic salts were removed (2−3 times). The resultant solution was dried again to obtain crude. It was recrystallized from ethanol (300 mL). The solid was filtered, washed with ethanol and dried in a vacuum desiccator to give white crystalline solid (72.2 g, 74%).

Diaion® SA10A(OH) (Mitsubishi Chemical Co.) anion-exchange resin (290 g, corresponding to 521 mmol of exchange capacity) was added into a solution of the iodide salt (70.2 g, 261 mmol) in water (500 mL). The whole mixture was kept statically for 53 h. After filtration, the aqueous solution was concentrated to 123.0 g to give 2.024 mmol/g TMP^+OH^- based on HCl titration of the resulting solution. The yield was 95%.

3.2.2 Preparation of high-silica FAU crystals used as a starting material for SSZ-39

An **FAU**-type zeolite with Si/Al = 10.3 was prepared as follows. 5.00 g of an **FAU**-type zeolites with Si/Al = 5.3 (Tosoh, HSZ-350HUA) was dispersed into 50 mL of 0.30 mol/L HNO_3 solution. The mixture was stirred at room temperature for 20 h. The solid was recovered by filtration, washed

with water and dried at 35 °C for 3 days. The mass of the resultant solid was 4.50 g. The XRD pattern showed that the **FAU** framework structure was maintained by the acid-treatment. The composition of the resultant solid was SiO_2 : 68.3 wt% and Al_2O_3 : 5.6 wt%, determined by ICP-AES.

3.2.3 Synthesis of high-silica SSZ-39

The synthesis procedure of SSZ-39 with Si/Al = 16.4 is as follows. 4.19 g of 1,1,3,5-tetramethylpiperidinium hydroxide solution (TMP^+OH^-, 2.03 mmol/g), 2.43 g of NaOH solution (3.68 mmol/g), 4.84 g of colloidal silica (Ludox AS-40, DuPont) were mixed in PFA beaker. The mixture was stirred on a hot plate at >80 °C allowing water to evaporate. Although the mixture became so viscosious that the stirrer was stopped after 1 h, the heating was continued. After 2 h, the resultant gel was cooled to room temperature and 5.31 g of H_2O was found to be evaporated. 0.11 g of H_2O (Milli-Q) and 1.52 g of **FAU** crystals with Si/Al = 10.3 were added and the whole mixture was stirred manually. The molar composition of the synthesis mixture was 1.0 SiO_2–0.017 Al_2O_3–0.17 TMP^+OH^-–0.18 NaOH–3.3 H_2O. The mixture was transferred into 23-mL Teflon vessel and the hydrothermal treatment was carried out statically at 160 °C for 92 h using an autoclave. The product was collected by repeated centrifugation (5 times, 4000 rpm) and dried at 100 °C overnight to give white powder (2.07 g). The calcination for the removal of OSDA was carried out in a muffle furnace. The temperature was raised from room temperature to 600 °C under 1 °C/min of the ramping rate, and maintained at the same temperature for 10 h. Finally the sample was cooled to room temperature in ambient condition.

3.2.4 Acid treatment of low-silica SSZ-39

Acid-treatment of low-silica SSZ-39 was carried out as follows. 0.10 g of calcined SSZ-39 was dispersed to the 5 mol/L nitric acid (3 mL) in 23-mL Teflon vessel. The treatment was carried out at 150 °C for 21 h with rotation at 20 rpm using an autoclave. The solid was filtered, washed with water and dried at 80 °C overnight. The treatment at 170 °C was carried out by the same way.

3.2.5 Synthesis of fault-free GME-type zeolite

TMP^+OH^- solution, NaOH solution and deionized water were mixed and then $Na_2Si_4O_9$ solution which was prepared by dissolving Ludox AS-40 to NaOH solution added. Next, **FAU** crystals with Si/Al = 2.8 (Tosoh, HSZ-320HOA) were added to the aqueous solution and dispersed well. The molar composition of the synthesis mixture is 1.0 SiO_2−0.033 Al_2O_3−0.17 TMP^+OH^- −0.50 NaOH−10 H_2O. The mixture was transferred into a Teflon-lined 23-mL steel autoclave and settled in a convection oven at 140 °C for 7 days. The solid product was filtered, washed with deionized water and dried at 100 °C overnight. The calcination of the as-synthesized sample was conducted in a muffle furnace. The temperature was raised from room temperature to 500 °C under 1.5 °C/min of the ramping rate,

and maintained at the same temperature for 3 h. Finally the sample was cooled to room temperature in ambient condition, which resulted in the white calcined powder.

3.2.6 Acid-treatment of as-synthesized samples

0.30 g of as-synthesized samples was dispersed into the 0.1 mol/L nitric acid (9.0 g) in 23-mL Teflon vessel. The treatment was carried out at 170 °C for 24 h with rotation at 20 rpm using an autoclave. The solid was filtered, washed with water and dried at 80 °C overnight. 0.238 g of the acid-treated sample was obtained as white powder. Calcination followed by the acid-treatment was carried out by the same way as mentioned before.

3.2.7 Synthesis of fault-free GME-type zeolites without using FAU crystals

TMP^+OH^- solution, NaOH solution and deionized water were mixed and $Al_2(SO_4)_3$ was added. The whole mixture was stirred at r.t. for 1 h to give almost clear solution. Sodium silicate solution (26.5wt% SiO_2, 10.6wt% Na_2O) was added dropwise and the while mixture was stirred at r.t. for another 3 h. The molar composition of synthesis mixture is 1.0 SiO_2−0.050 $Al_2(SO_4)_3$−0.17 TMP^+ OH^-−0.88 NaOH−20 H_2O. The resultant white suspension was transferred into a 125-mL Teflon-lined steel autoclave and rotated with 20 rpm at 140 °C for 4 days. The solid product was filtered, washed with deionized water and dried at 80 °C overnight.

3.2.8 Synthesis of typical AFI-type zeolites for XRD reference

N(16)-methylsparteinium hydroxide solution, NaOH solution and deionized water were mixed and sodium borate decahydrate ($Na_2B_4O_7{\cdot}10H_2O$) was added. The mixture was stirred at r.t. until sodium borate is dissolved. Fumed silica (Cab-O-Sil M5) was added and the whole mixture was stirred at r.t. for another 3 h. The resultant yellowish sol was transferred into a 23-mL Teflon-lined steel autoclave and the hydrothermal treatment was carried out statically at 170 °C for 7 days. The solid product was filtered, washed with deionized water and dried at 80 °C overnight. The calcination of the as-synthesized sample was conducted in a muffle furnace. The temperature was raised from room temperature to 600 °C under 5 °C/min of the ramping rate, and maintained at the same temperature for 6 h. Finally the sample was cooled to room temperature in ambient condition, which resulted in the white calcined powder.

3.2.9 Characterization

The crystallinity and phase purity of the zeolite samples were examined by powder X-ray diffraction (XRD) on an Ultima-IV (Rigaku) using CuKα radiation at 40 kV and 20 mA. The Si/Al and

Na/Al molar ratios in the bulk were determined by inductively coupled plasma, atomic emission spectrometer (ICP-AES, ICPE-9000, Shimadzu). Nitrogen adsorption and desorption isotherms at −196 °C were collected for the samples pre-treated at 400 °C for 12 h on a BELSORP-max gas adsorption instrument (MicrotracBEL). The morphologies of zeolite samples were observed by scanning electron microscope (SEM) on a JSM-7001F (JEOL). The organic contents included in the as-synthesized zeolite were determined by thermogravimetric and differential thermal analysis (TG-DTA, Thermo plus EVO II TG8120, Rigaku). The solid-state magic angle spinning nuclear magnetic resonance (MAS NMR) measurements were performed by using AVANCEIII 600 (Bruker) operating at 600 MHz for ^{1}H, 119.2 MHz for ^{29}Si and 156.4 MHz for ^{27}Al. All of the MAS NMR spectra were recorded at room temperature with samples in a 4 mm diameter ZrO_2 tube. The ^{29}Si chemical shifts were determined relative to hexamethylcyclotrisiloxane at −9.66 ppm. The dipolar-decoupling (DD) MAS NMR spectra were recorded by using 1024 pulses with a recycle time of 30 s at a spinning rate of 10 kHz. The ^{27}Al chemical shifts were determined by using an aqueous $Al(NO_3)_3$ solution, the resonance peak of which was adjusted to 0 ppm. The direct-excitation (DE) MAS NMR spectra were recorded by using 1024 pulses with a recycle time of 0.5 s at a spinning rate of 13 kHz.

3.3 Results and discussion

3.3.1 Synthesis of high-silica SSZ-39

Figure 3.3 shows the XRD patterns of the high-silica SSZ-39 in as-synthesized and calcined forms. Zeolitic phase of the as-synthesized sample was identified as **AEI** without impure phases. The **AEI** framework structure was retained by calcination, which promises high thermal stability. The Si/Al molar ratio was determined to be 16.4 by ICP-AES. This is the first example of the direct synthesis of the high-silica SSZ-39 with Si/Al higher than 10 by using TMP^+.

It was also firstly made possible to control the composition of SSZ-39 by tuning the amounts of alkali and water in the synthesis mixtures. Table 1 shows the synthetic conditions and results (XRD patterns are found in Figure 3.4). Notably, the Si/Al composition of the products can be flexibly controlled from 7.8 to 16.4. The product yield was improved with increasing the product Si/Al ratios. Diminishing both alkali and water amounts is necessary to obtain relatively high-silica products. In the synthesis of the sample with the lowest Al content (Table 1, entry 5), the parent mixture was gelated by evaporating water insistently at >80 °C till H_2O/SiO_2 = 3.3. Besides, the fraction of SiO_2 from **FAU** crystals designated as $(SiO_2)_{\mathbf{FAU}}$ should be large to obtain high-silica products. SSZ-39 had been synthesized from sodium silicate as an silica source, which caused highly alkaline synthesis mixtures.[14,16,18,19,21] In our work, Ludox AS-40 was used instead of sodium silicate to establish the lower alkaline conditions.

The increase in Si/Al ratios and the improved yields by decreasing alkali contents in the parent

mixtures are explained by decreased solubility of silicate species during SSZ-39 crystallization. However, the lower alkali content in the parent mixture often gave undesirable results without careful control of $(SiO_2)_{\mathbf{FAU}}$ and the content of H_2O. For example, SSZ-39 did not crystallize in dilute alkaline conditions (entry 6). In addition, the use of relatively low-silica **FAU** crystals in the concentrated conditions (H_2O/SiO_2 = 3.3) led to SSZ-39 crystallization accompanying with an impurity phase **(MTW**). This investigation indicates the necessity of both the evaporation process and the use of relatively high-silica **FAU** crystals, suggesting that the compositional similarity between the starting **FAU**-type zeolite and the SSZ-39 product as well as the structural similarity is essential for the single phase crystallization.

3.3.2 Characterizations of the high-silica SSZ-39

Based on TG-DTA analyses, the amount of OSDA cations occluded in SSZ-39 was found to be ca. 4 per unit cell regardless of Si/Al molar ratios of the solid products, meaning that 1 OSDA exactly occluded in an AEI cage. Therefore, the OSDA should be playing an important role to form the cage structure in both low- and high-silica SSZ-39. The amount of Na^+, on the other hand, decreased with decreasing the Si/Al ratios in relatively low-silica region (Si/Al < 10) mainly because Na^+ cation is generally occluded as the counter cation for anionic oxygen connecting to framework Al. However, the content of Na^+ was almost constant where Si/Al >10, probably due to remaining space in the micropores of SSZ-39 occluding OSDA cations.

Nitrogen adsorption-desorption measurements of calcined SSZ-39 with various Si/Al ratios gave typical type-I isotherms (Figure 3.5), promising the presence of micropores. The physicochemical properties are summarized in Table 3.2. The Si/Al ratios increased with the increase in the BET area (S_{BET}) and the external surface area (S_{ext}), suggesting high-silica SSZ-39 particles are small. In contrast, the micropore volume (V_{micro}) did not show significant changes regardless of Si/Al ratios.

As shown in FE-SEM images (Figure 3.6), morphologies of SSZ-39 obtained in this work were rectangular or plate-like. There was tendency that the particle diameters decreased with increasing the Si/Al ratios. The sample with the highest Si/Al molar ratio (16.4, entry 5) was composed of nanocrystals with 200−300 nm in size (Figure 3.6d). This is the first achievement of nanocrystalline SSZ-39. Decreasing water and alkali contents made the gel extremely concentrated, which may have promoted effective interaction between OSDA and silicate species, leading to frequent nucleation of SSZ-39 crystals.

SSZ-39 with the lowest Al content (Si/Al = 16.4) was investigated by solid-state ^{27}Al and ^{29}Si MAS NMR to examine the states of Al and defect sites. Figure 3.7 shows the ^{27}Al DE-MAS NMR spectra of as-synthesized and calcined SSZ-39. All the Al atoms in both samples were tetrahedrally

coordinated, and no octahedral Al was observed. ^{29}Si DD and CP MAS NMR spectra of as-synthesized and calcined SSZ-39 (Figure 3.8) proved the presence of framework Al. The both samples showed three peaks at ca. −110, −105 and −100 ppm assigned to Q^4(0Al) ($Si(OSi)_4$), Q^4(1Al) ($Si(OSi)_3(OAl)$) and Q^3(0Al) ($Si(OSi)_3(OH)$), respectively. The framework ratios of the as-synthesized sample and the calcined sample are estimated to be 15.8 and 19.2. Calcination led to decrease Q^3(0Al) ($Si(OSi)_3(OH)$) probably due to disappearance of connectivity defects ($SiO^-\ldots HOSi$)[34] which were formed in order to balance the cationic charges of OSDA. These values are almost consistent with the bulk Si/Al ratio(16.4), meaning that the assignation of the peaks are correct. The spectra are quite similar to that of high-silica CHA-type zeolites which have considerable structural similarity to SSZ-39.[35]

3.3.3 Trial for preparation of high-silica SSZ-39 via post-synthetic modification

We now attempted to prepare high-silica SSZ-39 via dealumination of low-silica one by acid-treatment using 5 mol/L nitric acid. The treatment at 150 °C of the low-silica sample (Si/Al = 8.0) gave the slightly dealuminated product with Si/Al = 12.7. Raising the treatment temperature to 170 °C caused partial amorphization. The high-silica SSZ-39 with Si/Al as high as 16 was not obtained via dealumination of low-silica SSZ-39, which revealed the necessity of the direct hydrothermal synthesis.

3.3.4 Synthesis of GME-type zeolite by TMP^+

Figure 3.14 shows XRD patterns of the as-synthesized sample with the highest purity (among the products obtained from **FAU** crystals) and the calcined sample. Although an **ANA** phase contained in the sample as an impurity, the sample was pure enough to conduct further characterizations (Figure 4.14a). The XRD peaks of the as-synthesized **GME**-type zeolite are not broadened significantly, which indicates that the sample is fault-free and its 12R channels are not likely to be blocked by intergrowth of other phases. The **GME** phase converted into an **AFI** phase by calcination (Figure 4.14b). Similar conversion was reported about the **GME**-type zeolites obtained by Dab-4Br polymer.[3)] The XRD pattern of a typical **AFI**-type zeolite (calcined [B]-SSZ-24) is shown in Figure 4.14c. Slight difference of lattice constants between aluminosilicate and borosilicate **AFI**-type zeolites resulted in some shifts of the XRD patterns along with the horizontal axis. The separation parameters of both **AFI**-type zeolites are listed in Table 1. Al-rich **AFI**-type zeolite has relatively higher lattice constants, indicating longer T−O bond lengths and/or higher T−O−T angles.

Figure 3.15 showed XRD patterns of the samples before/after the acid-treatment and after the subsequent calcination. The framework structure did not change after acid-treatment (Figure 4.15b). Interestingly, the thermal conversion into the **AFI** phase did not occur under the calcination conditions

(Figure 4.15c). Thus the OSDA was successfully removed from the micropore, obtaining the microporous fault-free **GME**-type zeolite.

3.3.5 Characterization of GME-type zeolites

Table 4.4 showed the elemental analyses of the **GME**-type zeolites by ICP-AES. The Si/Al ratio of the as-synthesized sample (3.6) was relatively high compared to the reported **GME**-type zeolites (2.5−3.5).[3)] The Na/Al ratio (0.72) was lower than 1, indicating a part of counter cations of anionic framework was the OSDA cation. After the acid-treatment, the Si/Al ratio was slightly increased (4.1). This is the highest value among that of **GME**-type zeolites which have been prepared so far. The Na/Al ratio was drastically decreased to around the half value (0.33) by the treatment. It suggests that the cation exchange of Na^+ with H^+ occurred. Although cation exchange of Na^+ in an as-synthesized **GME**-type zeolite with K^+ is reported to be an effective way to prevent the conversion into **AFI**,[4)] this study provides the alternative method to obtain the microporous **GME**-type zeolites.

Figure 3.16 showed FE-SEM images of the particles of the as-synthesized **GME**-type zeolite. Hexagonal rod-shaped particles were clearly observed. The length of the crystals was 0.5−10 μm and the thickness was approximately 200 nm. This morphology is easily expected from the crystal structure. Figure 3.17 showed an FE-SEM image of the **ANA**-type zeolite containing in the sample as an impurity. The spherical particle with approximately 5 μm in diameter was observed and it is easy to distinguish the **GME** particles from the impurity. Figure 3.18 showed the particles after the acid-treatment. The hexagonal rod-shaped morphology was remained. The length of the particles, however, significantly decreased to shorter than 2 μm probably because the rods were broken by the treatment. Site defects formed by dealumination probably weakened the rods mechanically. This explanation is under the assumption that the observed hexagonal particles are single crystals.

3.3.6 Formation of mesopores by acid-treatment

If the hexagonal particles are polycrystalline, volume shrinkages of primary particles can give a reasonable explanation about the cleavage. It is well-known that steam treatments of zeolites at high temperature often lead dealumination and resultant site defects are filled by diffusion or migration of neighbor Si atoms. Continuous Si migration results diffusion of site defects to external surfaces, diminishing site defects.

Si migration is often observed as formation of mesopores which is derived from volume shrinkages of primary crystals. For example, there are many reports about the formation of mesopores in **FAU**-type zeolites (USY) by steam treatment.[49,50)] Recently, the as-synthesized pure-silica **MSE**-type zeolite (YNU-2P) was reported to form mesopores by steaming at relatively low temperature (~250

°C).[51] Although the formation of mesopores are often seen in gas phase steaming at high temperatures, Si migration could occur by acid-treatment in liquid phase at relatively low temperature (< 200 °C). Besides, H^+ can catalyze hydrolysis and condensation of silicate, which means that it promotes Si migration. Therefore, shrinkages of primary particles possibly resulted in the formation of cleavages, leading the crystals to be broken into two.

Figure 3.19 displays nitrogen adsorption-desorption isotherms of the **AFI** and **GME**-type zeolites obtained in this work. Obviously the micropore volume of the **GME**-type zeolite was much higher than the **AFI**-type zeolite as reflected in the isotherms in $P/P_0 < 0.1$. This is in agreement with the difference in crystal structures. Although both zeolites have 1-dimensional 12R pores, the presence of 2-dimensional 8R pores in the **GME**-type zeolite resulted in

the high micropore volumes. A hysteresis in the desorption isotherm is another remarkable feature of the **GME** sample. It revealed the presence of mesopores which is formed by Si migration during the acid-treatment as mentioned above. BET (Brunauer-Emmett-Teller) surface areas, external surface areas and micropore volumes were estimated and listed in Table 2.

Figure 3.20 shows an illustration of mesopores and cleavages originated from volume shrinkages of primary crystals by the acid-treatment. Mesopores would be space formed between sides of hexagonal crystals. On the other hand, cleavages would be space formed between heads of rod crystals.

3.3.7 Influence of Al sources on particle morphology

Figure 3.21 exhibits the FE-SEM images of the **GME**-type zeolite obtained by using $Al_2(SO_4)_3$ as an Al source. Although primary crystals were likely to be hexagonal, complicated aggregations were observed. The sizes of primary crystals were approximately 400 nm and which is a double sizes of those obtained from the **FAU**-type zeolite. It indicates the **FAU**-type zeolite promotes more frequent nucleation than $Al_2(SO_4)_3$ does, probably due to the structural similarity between **FAU** and **GME**.

3.4 Conclusion

In summary, SSZ-39 with Si/Al as high as 16 has been directly synthesized for the first time by using TMP^+OH^-. Its particle size was 200−300 nm which is smaller than any other SSZ-39 reported so far. We have also developed the synthetic method of SSZ-39 to tune their Si/Al ratios of SSZ-39 in the range between 8 and 16. This high-silica SSZ-39 is the promising material for catalytic applications such as MTO and SCR processes, and our developed synthetic method should enhance the industrial feasibility of SSZ-39.

A novel **GME**-type zeolite has been successfully obtained by using 1,1,3,5-tetramethylpiperidinium as an OSDA. The removal of the OSDA required the acid-treatment prior to the calcination, in order to decrease the Na^+ content in the sample. This novel large-pore zeolite can be dealuminated

probably, suggesting the tunability of Si/Al composition. If so, this material has tremendous pontetials for industrial applications as solid acid catalysts.

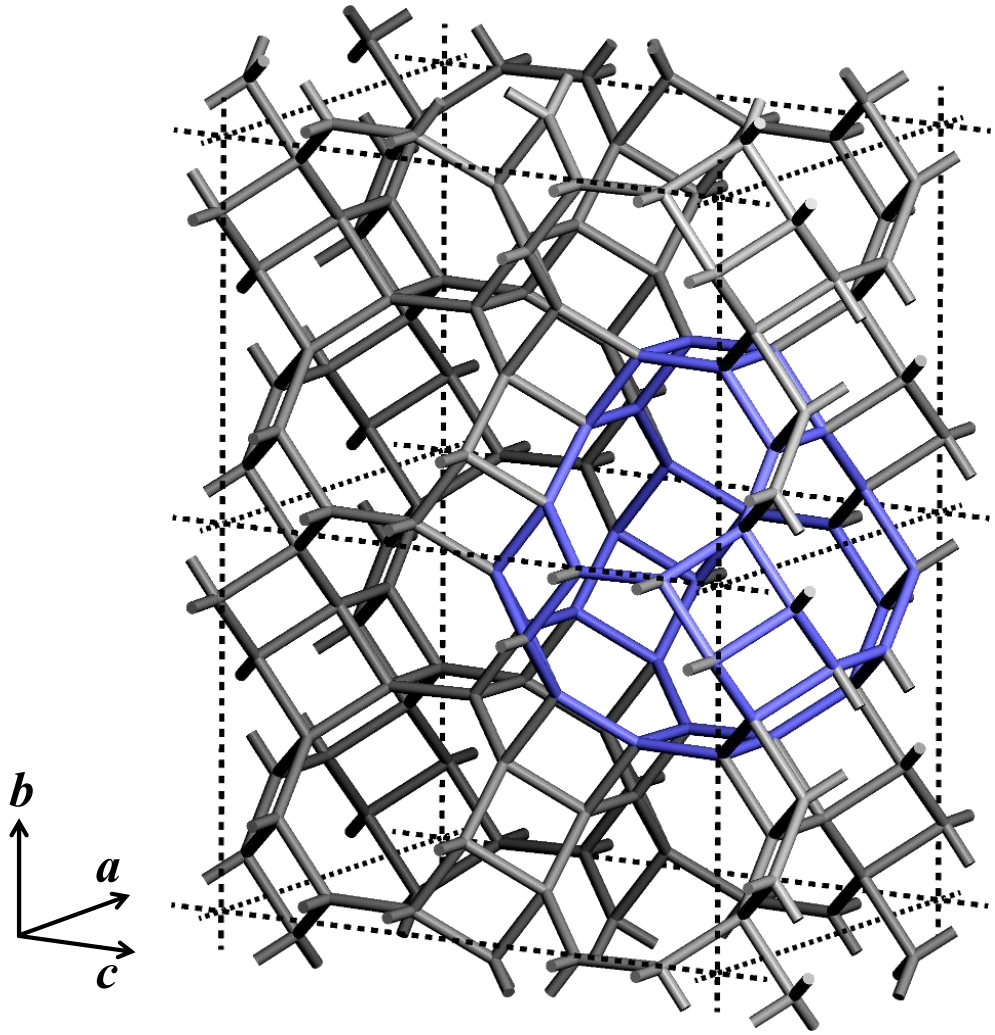

Figure 3.1. Framework structure of **AEI.**

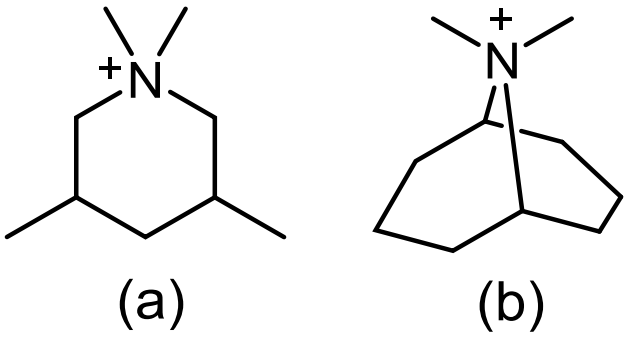

Figure 3.2. Two representative OSDAs to obtain SSZ-39 : (a) 1,1,3,5-tetramethylpiperidinium (used in this work) and (b) 9,9-dimethyl-9-azoniabicyclo[3.3.1]nonane.

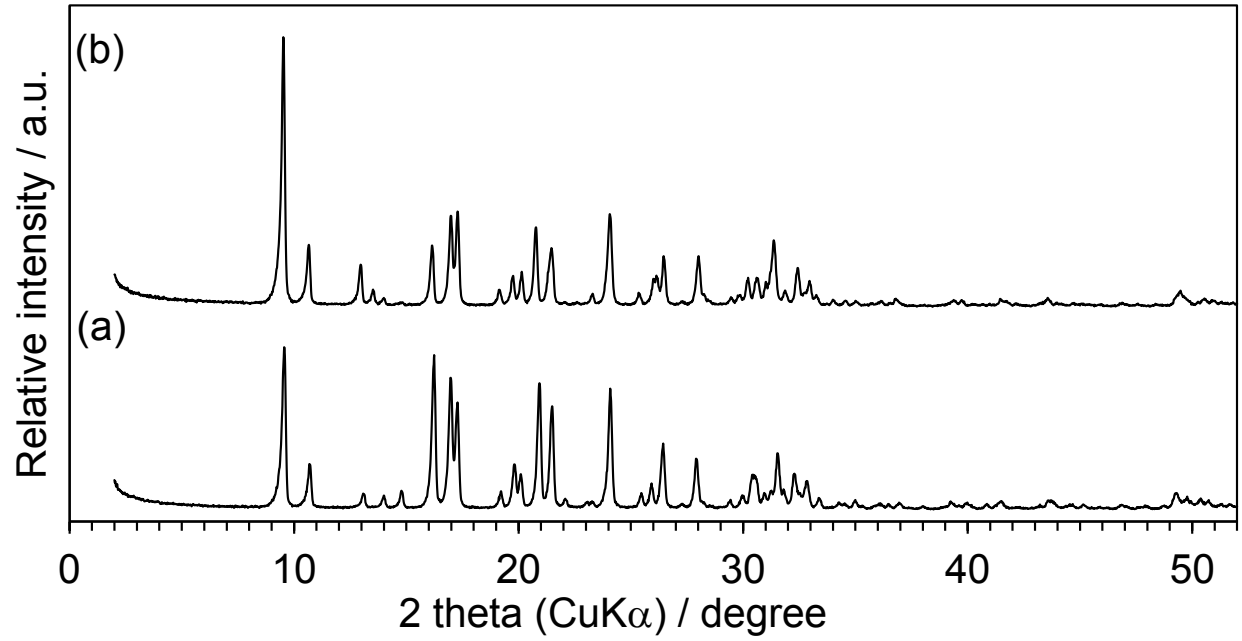

Figure 3.3. XRD patterns of (a) as-synthesized and (b) calcined SSZ-39 with Si/Al = 16.4.

Table 3.1. Synthetic investigation of SSZ-39 with the **AEI** topology.

Entry	Molar composition of synthesis mixture[a]				Product				
	$(SiO_2)_{\mathbf{FAU}}$[b]	$(SiO_2)_{amor.}$[c]	NaOH	H_2O	Phases	Yield[d] [%]	Si/Al[e]	Na/Al[e] per unit cell	TMP^+ per unit cell[f]
1	0.12[g]	0.88	0.45	20.0	**AEI**	39	7.8	1.96	4.16
2	0.12[g]	0.88	0.40	12.0	**AEI**	43	9.3	0.89	4.20
3	0.18[h]	0.82	0.30	8.0	**AEI**	56	12.7	0.56	4.46
4	0.18[h]	0.82	0.24	5.0	**AEI**	56	14.7	0.41	4.42
5	0.35[i]	0.65	0.18	3.3	**AEI**	69	16.4	0.74	4.48
6	0.12[g]	0.88	0.18	20.0	**FAU + MTW**	56	n.d.	n.d.	n.d.
7	0.18[h]	0.82	0.18	3.3	**FAU + AEI + MTW**	34	n.d.	n.d.	n.d.

[a]Synthesis temperature was 160 °C and crystallization time was 3 days except entry 5 (4 days). Input Si/Al molar ratio was 30 and SiO_2 came from **FAU** crystals and colloidal silica. TMP^+OH^-/SiO_2 ratio was 0.17.
[b]SiO_2 came from **FAU** crystals.
[c]SiO_2 came from Ludox AS-40.
[d]The mass of the as-synthesized product over that of SiO_2 in the synthesis mixture.
[e]The Si/Al molar ratio was determined by ICP-AES.
[f]Determined by TG-DTA.
[g]Si/Al = 3.6 (Tosoh, HSZ-341NHA).
[h]Si/Al = 5.3 (Tosoh, HSZ-350HUA).
[i]Si/Al = 10.3 (dealuminated HSZ-350HUA).

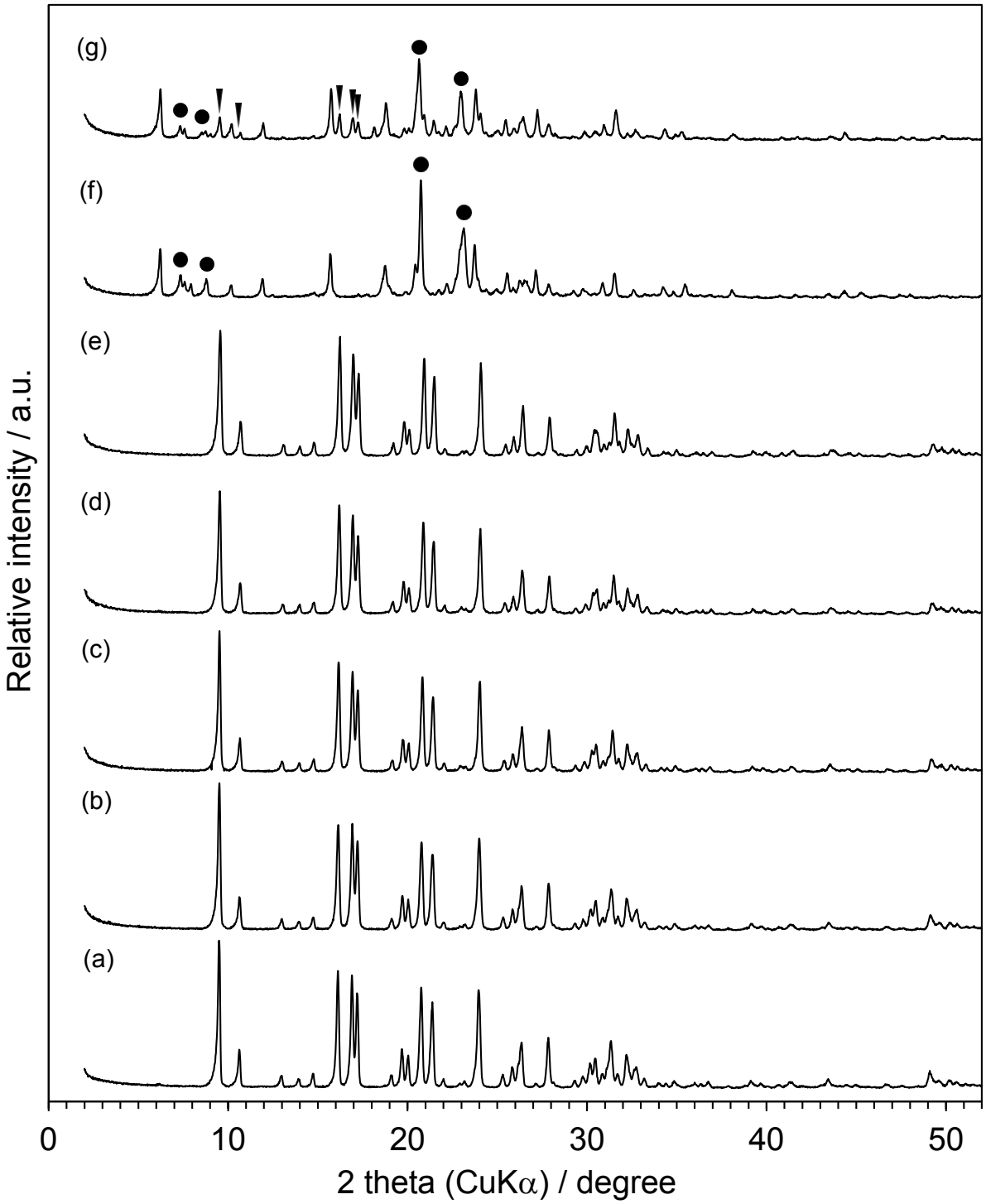

Figure 3.4. XRD patterns of (a) entry 1, (b) 2, (c) 3, (d) 4, (e) 5, (f) 6 and (g) 7 in Table 3.1, respectively. The symbols (●) and (▼) refer to the peaks attributable to **MTW** and **AEI**, respectively.

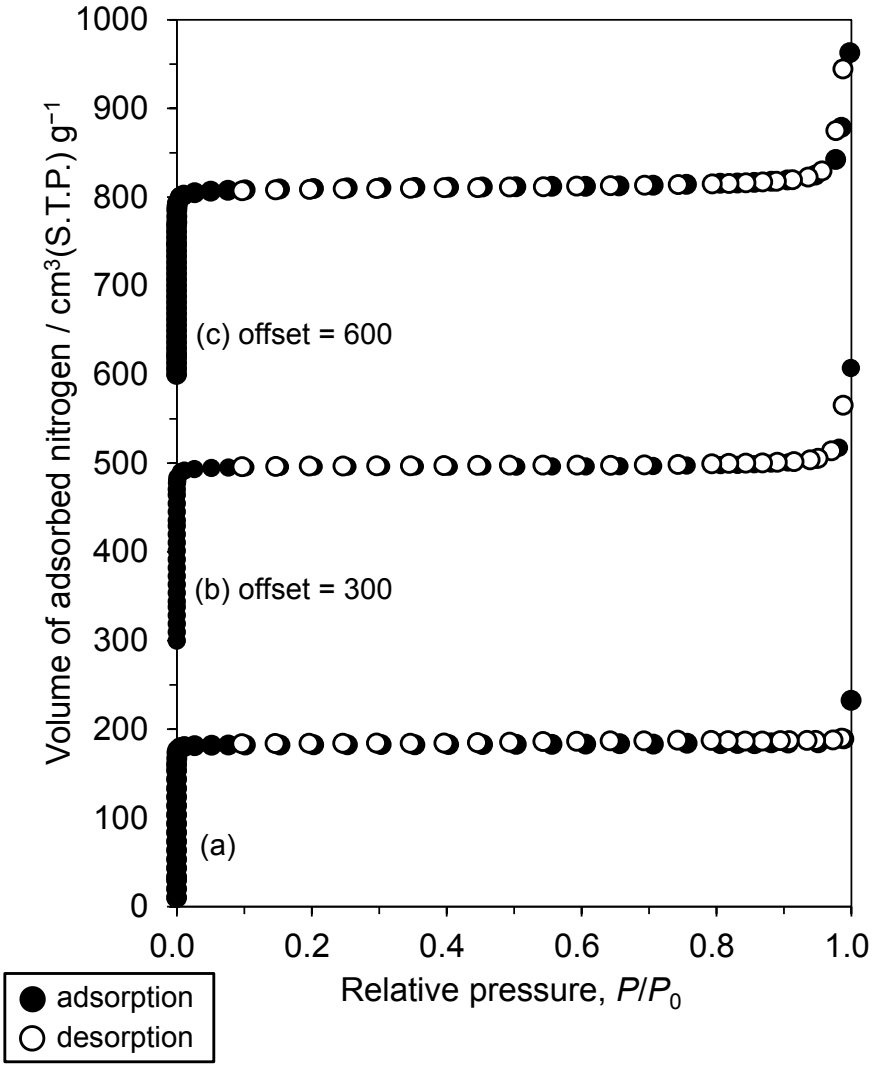

Figure 3.5. Nitrogen adsorption-desorption isotherms of SSZ-39 with (a) Si/Al = 7.8, (b) 12.7 and (c) 16.4, respectively.

Table 3.2. Physicochemical properties of SSZ-39.

Entry[a]	Si/Al[b]	S_{BET}[c] [m^2/g]	S_{ext}[d] [m^2/g]	V_{micro}[e] [cm^3/g]	Particle size[f] [μm]
1	7.8	730	1.6	0.283	2
3	12.7	782	7.6	0.299	0.4
7	16.4	829	16.6	0.316	0.3

[a]The crystallization conditions are described in Table 3.1. [b]Estimated by ICP-AES. [c]BET area estimated on the basis of nitrogen adsorption isotherms. [d]External surface area estimated by the *t*-plot method. [e]Micropore volume estimated by the *t*-plot method. [f]Estimated by FE-SEM observation.

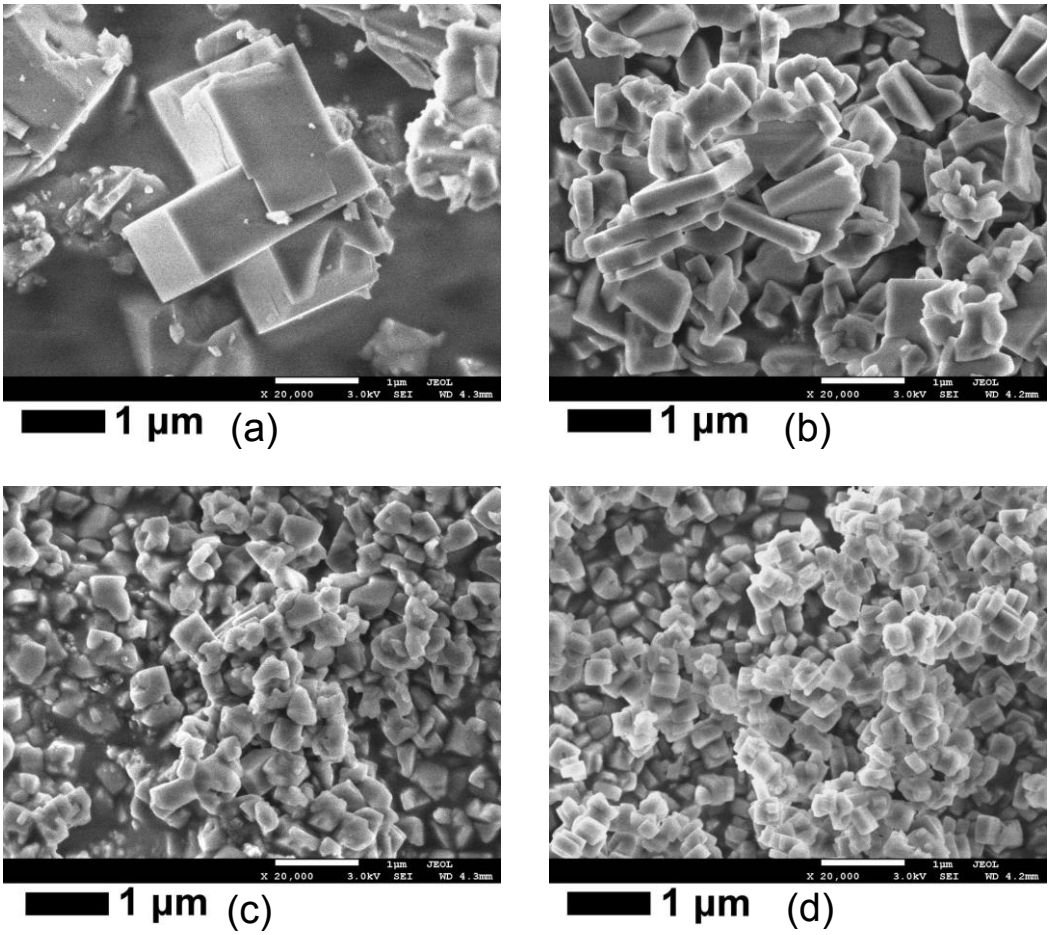

Figure 3.6. FE-SEM images of SSZ-39 with (a) Si/Al = 7.8, (b) 9.1, (c) 12.7 and (d) 16.4.

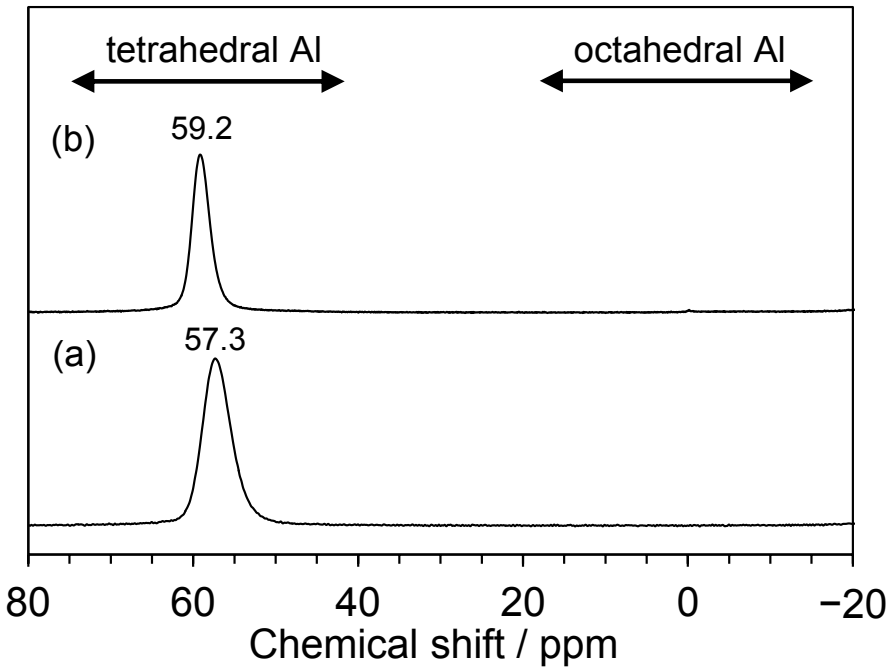

Figure 3.7. ^{27}Al DE MAS NMR spectra of (a) as-synthesized and (b) calcined SSZ-39 with bulk Si/Al = 16.4.

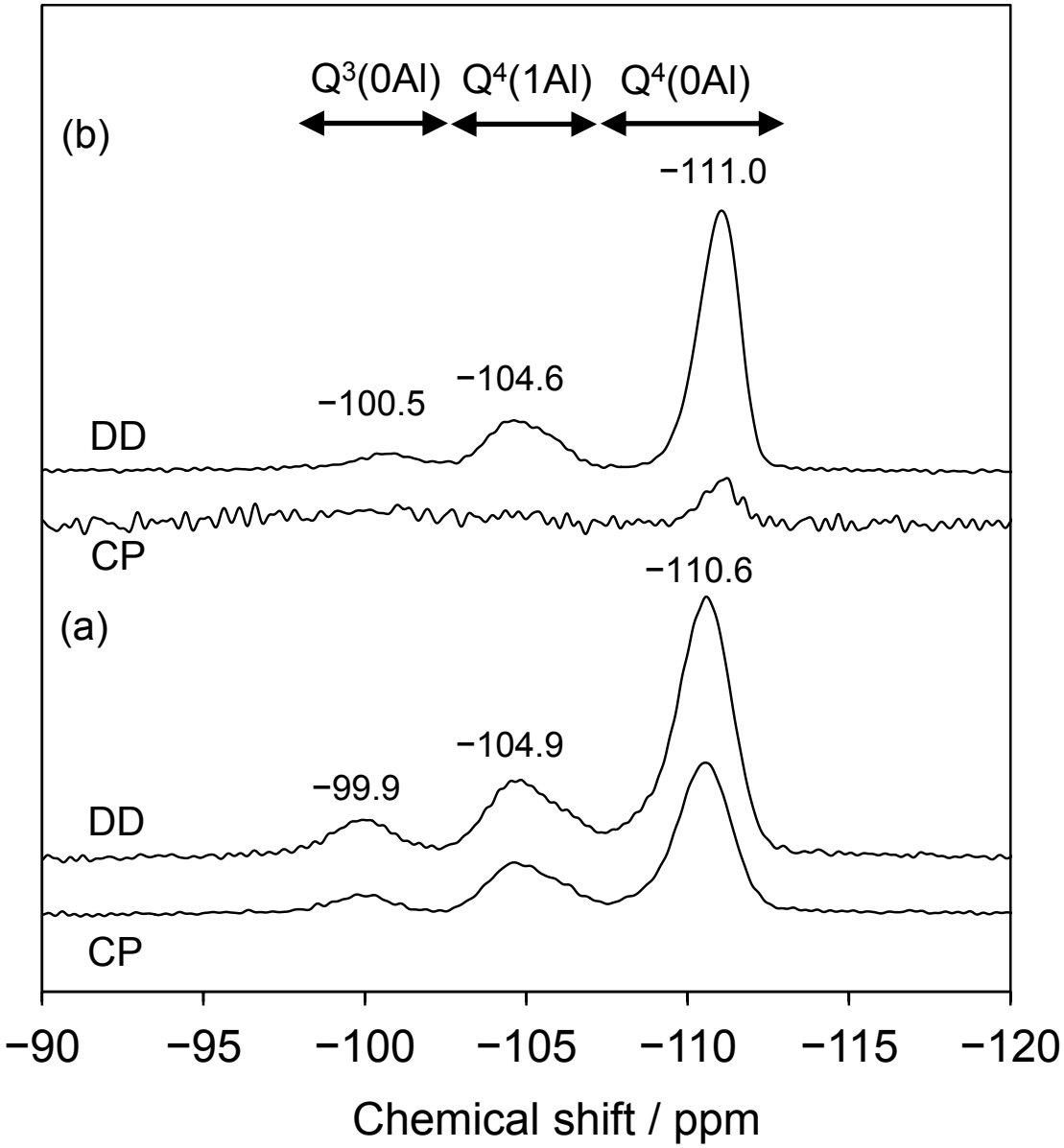

Figure 3.8. ^{29}Si DD and CP MAS NMR spectra of (a) as-synthesized and (b) calcined SSZ-39 with bulk Si/Al = 16.4. $Q^4(0Al)$, $Q^4(1Al)$ and $Q^3(0Al)$ denote $Si(OSi)_4$, $Si(OAl)(OSi)_3$ and $Si(OSi)_3(OH)$, respectively.

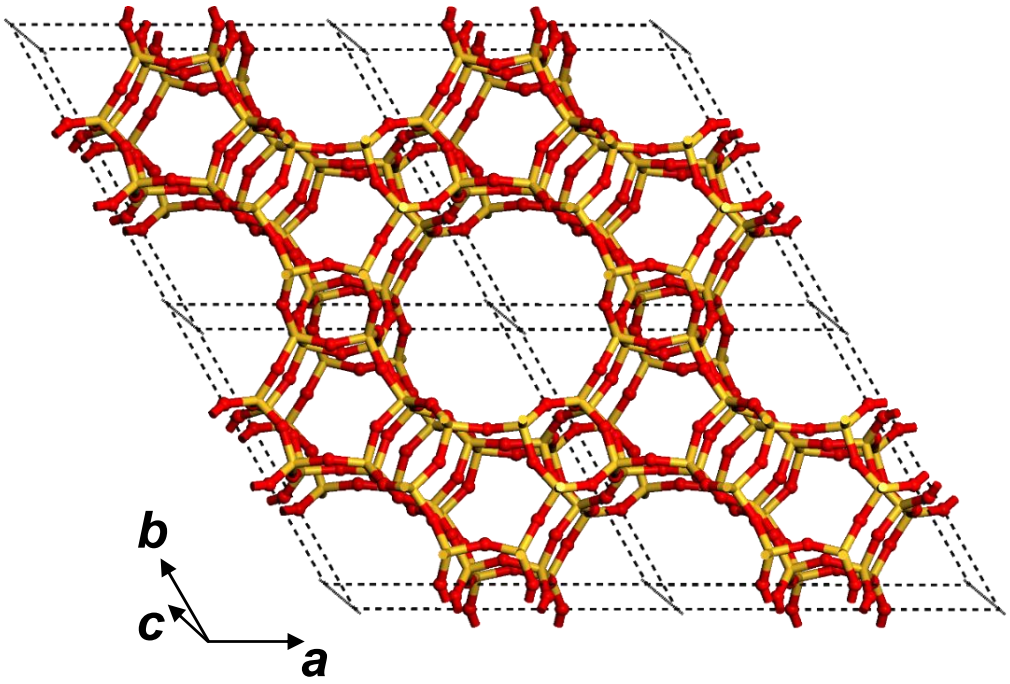

Figure 3.9. Crystal structure of **GME**-type zeolites view along [001].

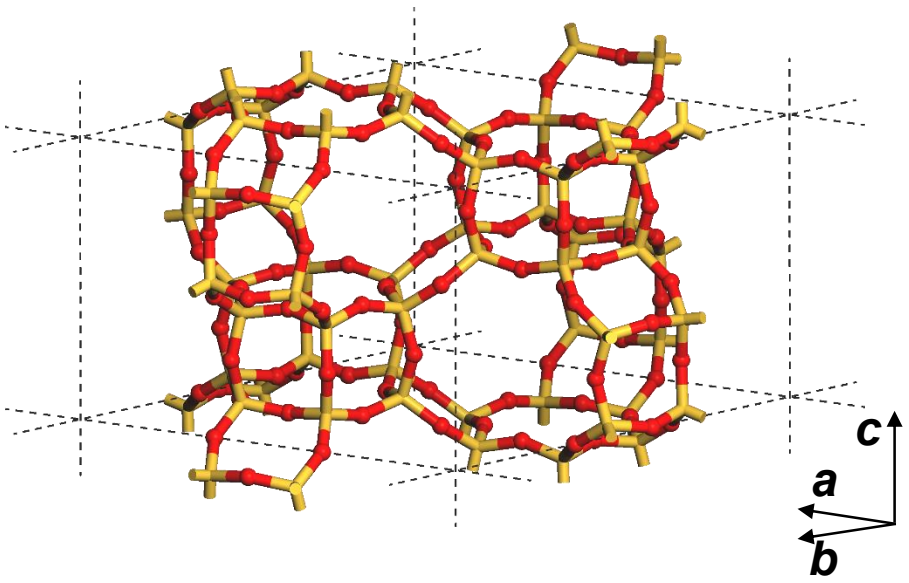

Figure 3.10. A unit cell of **GME**-type zeolites. 8R channels are composed of small **GME**-cages. $a = b = 1.375$ nm, $c = 10.05$ nm, $\alpha = 90°$, $\beta = 90°$, $\gamma = 120°$ [19)]

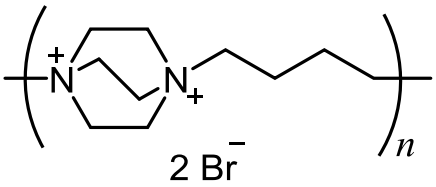

Figure 3.11. Chemical structure of polymeric Dab-4Br.

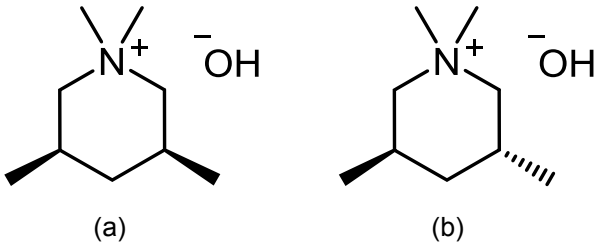

Figure 3.12. Chemical structures of (a) *cis*- and (b) *trans*-1,1,3,5-tetramethylpiperidinium hydroxide

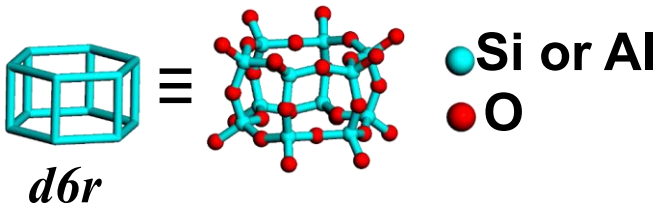

Figure 3.13. *D6r* building unit.

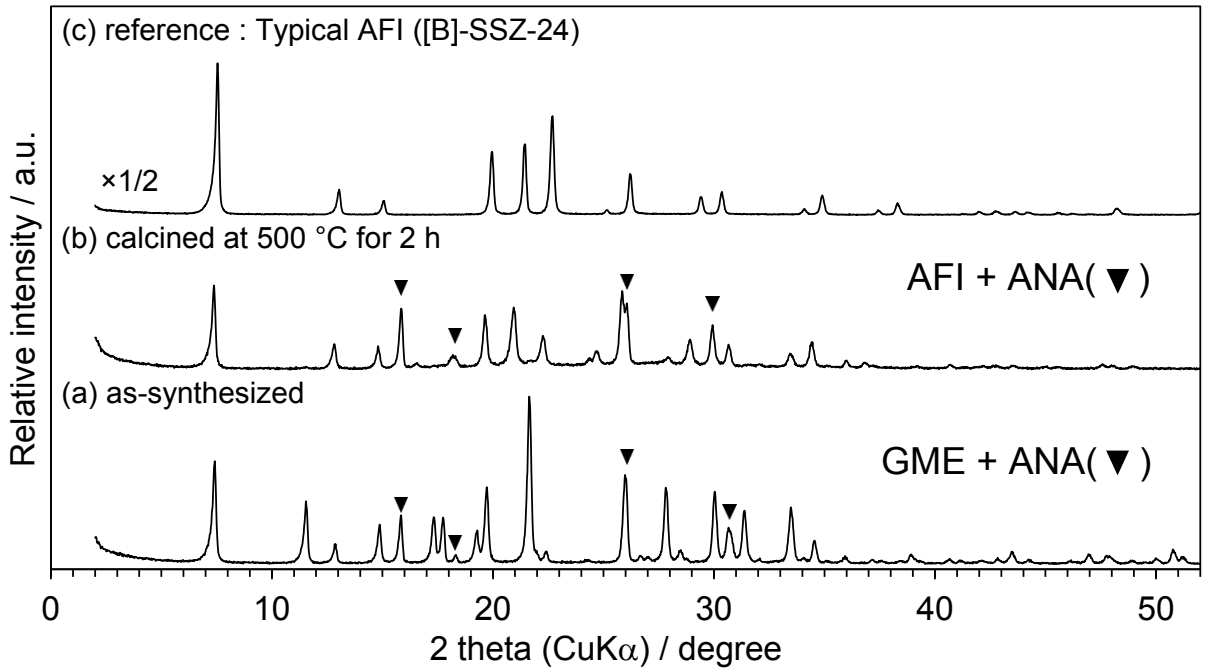

Figure 3.14. XRD patterns of (a) the as-synthesized sample with the highest purity (among the products from FAU crystals), (b) the calcined sample and (c) a typical calcined **AFI**-type zeolite ([B]-SSZ-24).

Table 3.3. Separation parameters of aluminosilicate (Si/Al ~ 3) and borosilicate **AFI** (Si/B ~ 20) determined by powder X-ray diffraction.

	aluminosilicate **AFI**		borosilicate **AFI**	
hkl	2 theta [degree]	*d* [Å]	2 theta [degree]	*d* [Å]
100	7.54	11.72	7.38	11.97
110	13.04	6.78	12.82	6.90
200	15.06	5.88	14.82	5.97
210	19.96	4.44	19.66	4.51
002	21.44	4.14	20.96	4.24

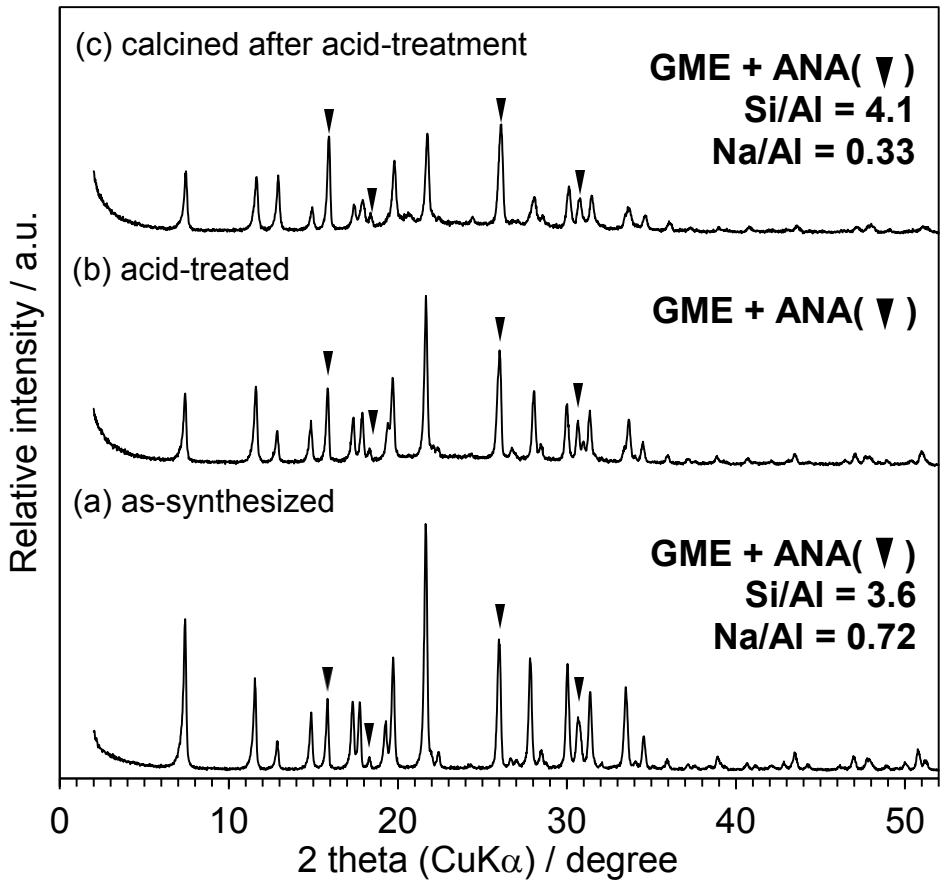

Figure 3.15. XRD patterns of (a) the as-synthesized sample, (b) the acid-treated sample and (c) the sample calcined after acid-treatment.

Table 3.4. Elemental analyses of **GME**-type zeolites by ICP-AES. The values were obtained from hydrofluoric acid solutions of the samples.

Samples	Si/Al	Na/Al
calcined, without acid-treatment	3.6	0.72
calcined after acid-treatment	4.1	0.33

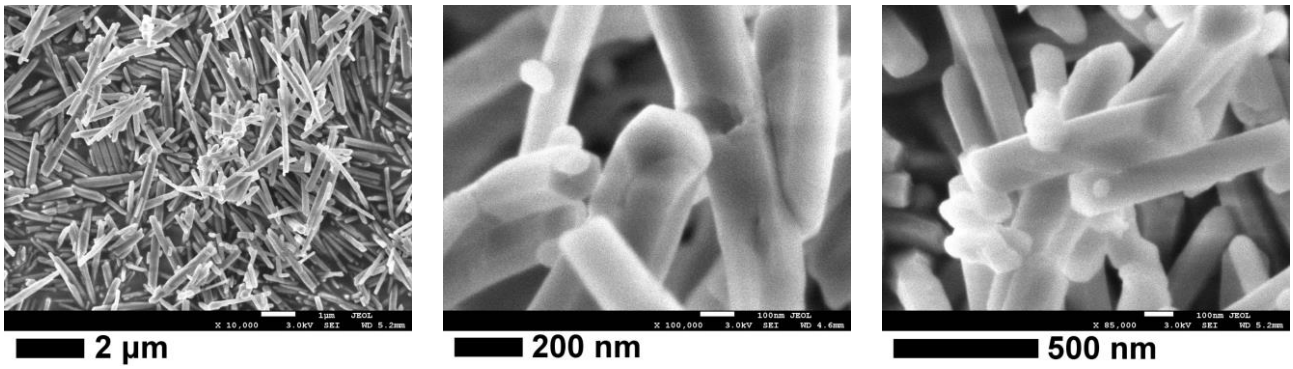

Figure 3.16. FE-SEM images of the as-synthesized **GME**-type zeolites.

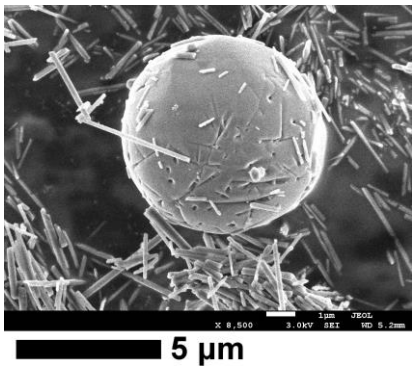

Figure 3.17. An FE-SEM image of the **ANA**-type zeolite containing in the **GME** sample as an impurity.

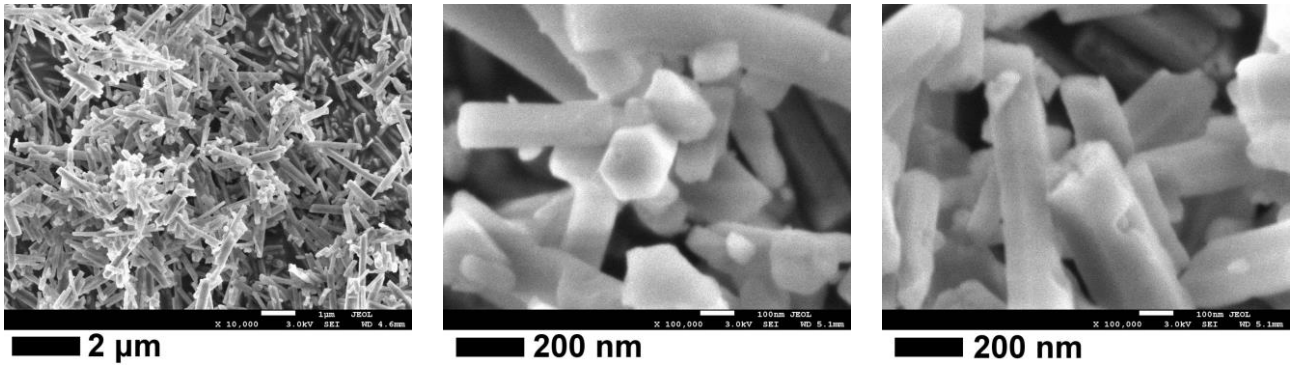

Figure 3.18. FE-SEM images of the acid-treated **GME**-type zeolites.

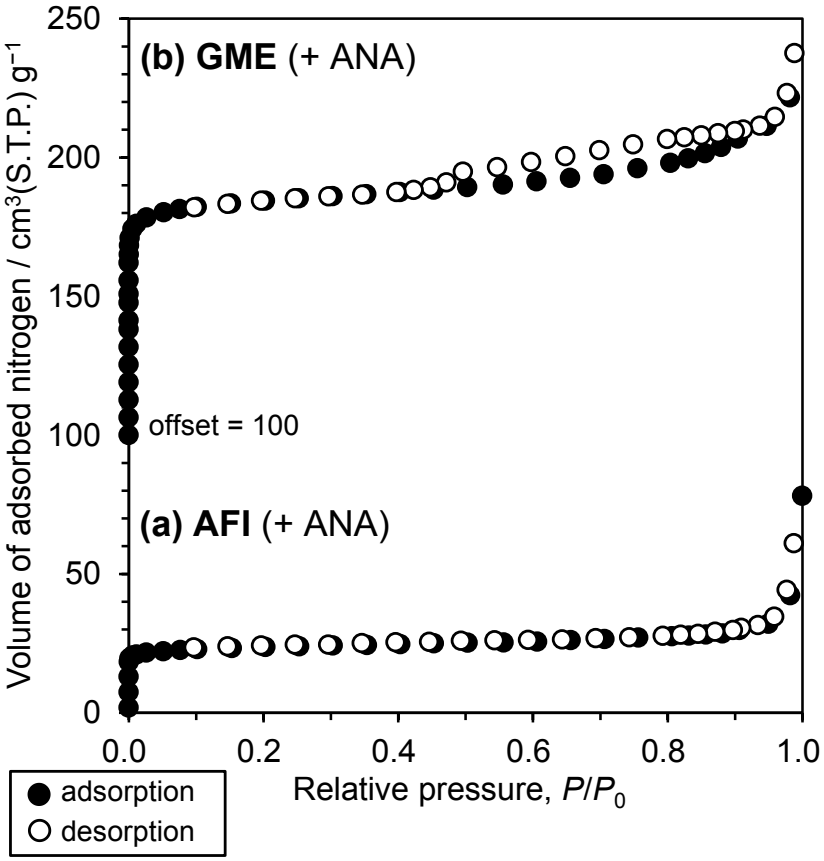

Figure 3.19. Nitrogen adsorption-desorption isotherms of (a) the **AFI**-type zeolite and (b) the **GME**-type zeolite obtained in this work. Both samples contained the **ANA**-type zeolite as an impurity.

Table 3.4. Surface areas and micropore volumes estimated from nitrogen adsorption measurements.

Sample phases	S_{BET} [a] **[m²/g]**	$S_{ext.}$ [b] **[m²/g]**	V_{micro} [c] **[cm³/g]**
AFI + **ANA**	88	9.9	0.033
GME + **ANA**	322	35.3	0.118

a) BET (Brunauer-Emmett-Teller) surface area.
b) External surface area estimated by the *t*-plot method.
c) Micropore volume estimated by the *t*-plot method.

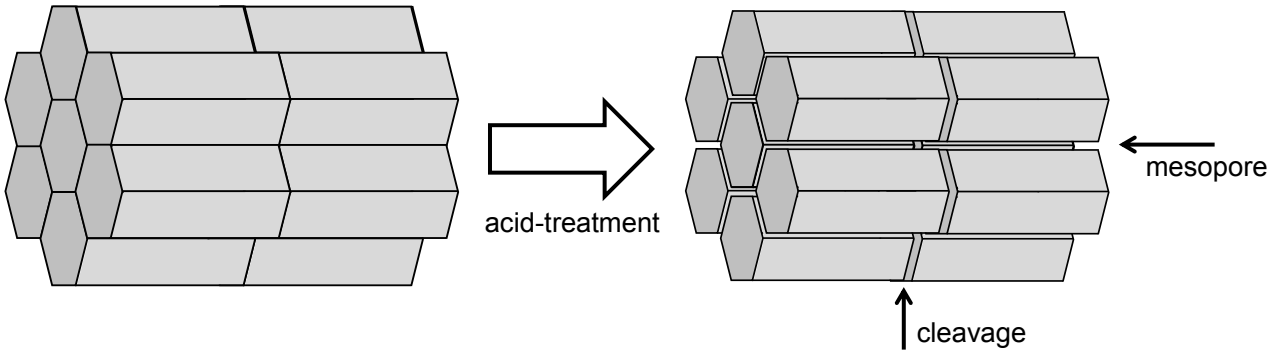

Figure 3.20. Illustration of mesopores and cleavages originated from volume shrinkages of primary crystals by acid-treatment.

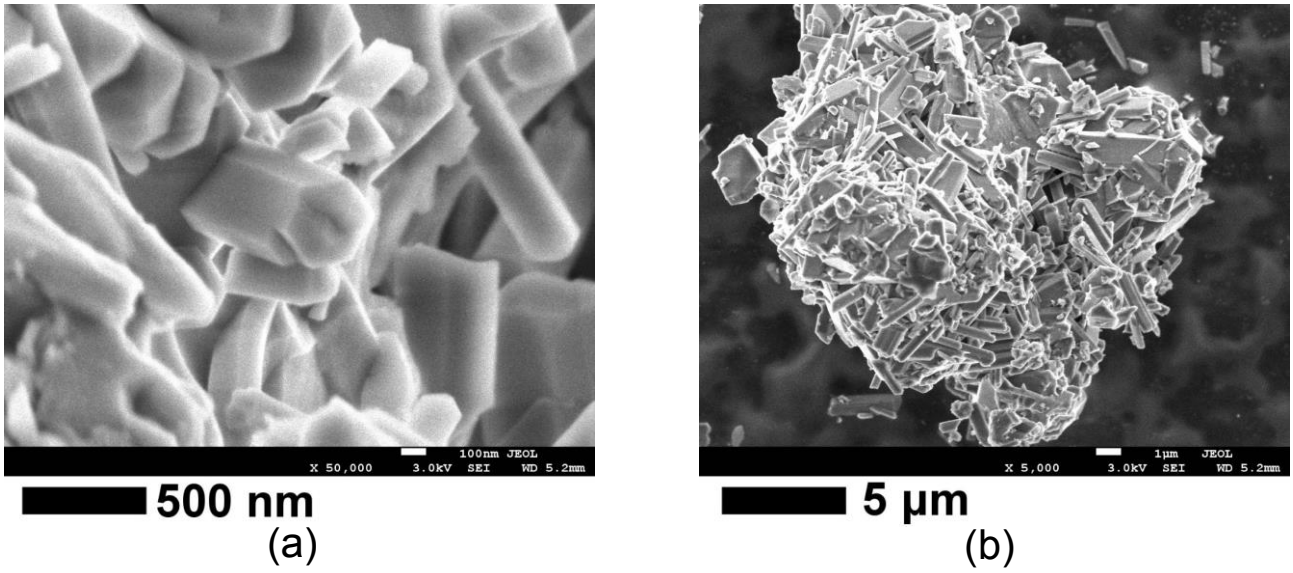

Figure 3.21. FE-SEM observations of the **GME**-type zeolite obtained by using $Al_2(SO_4)_3$ as an Al source.

3.5 References

1) R.K. Ahedi, Y. Kubota, Pusparatu, Y. Sugi, *Bull. Chem. Soc. Jpn.*, **76**, 883 (2003)

2) H. Maekawa, Y. Kubota, Y. Sugi, *Chem. Lett.*, **33**, 1126 (2004).

3) H. Jon, K. Nakahata, B. Lu, Y. Oumi, T. Sano, *Micropor. Mesopor. Mater.*, **96**, 72 (2006).

4) H. Jon, S. Takahashi, H. Sasaki, Y. Oumi, T. Sano, *Micropor. Mesopor. Mater*., **56**, 113 (2008).

5) M. Itakura, I. Goto, A. Takahashi, T. Fujitani, Y. Ide, M. Sadakane, T. Sano, *Micropor. Mesopor. Mater*., **144**, 91 (2011).

6) S. Inagaki, Y. Tsuboi, Y. Nishita, T. Syahylah, T. Wakihara, Y. Kubota, *Chem. Eur. J.*, **19**, 7780 (2013).

7) K. Iyoki, K. Itabashi, T. Okubo, *Micropor. Mesopor. Mater.*, **22**, 189 (2014).

8) B. Xie, J. Song, L. Ren, Y. Ji, J. Li, F.S. Xiao. *Chem. Mater.*, **20**, 4533 (2008).

9) Y. Kubota, K. Itabashi, S. Inagaki, Y. Nishita, R. Komatsu, Y. Tsuboi, S. Shinoda, T. Okubo, *Chem. Mater.*, **26**, 1250 (2014).

10) K Iyoki, Y. Kamimura, K. Itabashi, A. Shimojima, T. Okubo, *Chem. Lett.*, **39**, 730 (2010).

11) Y. Kamimura, K. Itabashi, T. Okubo, *Micropor. Mesopor. Mater.*, **147**, 149 (2012).

12) H. Imai, N. Hayashida, T. Yokoi, T. Tatsumi, *Micropor. Mesopor. Mater.*, **196**, 341 (2014).

13) K. Iyoki, M. Takase, K. Itabashi, K. Muraoka, W. Chaikittisilp, T. Okubo, *Micropor. Mesopor. Mater.*, **215**, 191 (2015).

14) P. Wagner, Y. Nakagawa, G.S. Lee, M.E. Davis, S. Elomari, R.C. Medrud, S.I. Zones, *J. Am. Chem. Soc.*, **122**, 263 (2000).

15) Ch. Baerlocher, L.B. McCusker, D.H. Olson, *Atlas of Zeolite framework Types*, Elsevier, Amsterdam, 6th edn., 2007, see also: http://www.iza-structure.org/databases/.

16) M. Moliner, C. Franch, E. Palomares, M. Grill, A. Corma, *Chem. Commun.*, **48**, 8264 (2012).

17) M.J. Wulfers, S. Teketel, R.F. Lobo, *Chem. Commun.*, **51**, 4477 (2015).

18) M. Dusselier, M.A. Deimund, J.E. Schmidt, M.E. Davis, *ACS Catal*., **5**, 6078 (2015).

19) M. Dusselier, J.E. Schmidt, R. Moulton, B. Haymore, M. Hellums, M.E. Davis, *Chem. Mater.*, **27**, 2695 (2015).

20) Y. Nakagawa, US Patent, 5 273 736 (1993).

21) S.I. Zones, Y. Nakagawa, S.T. Evans, G.S. Lee, *US Patent*, 5 958 370 (1999).

22) T. Maruo, N. Yamanaka, N. Tsunoji, M. Sadakane, T. Sano, *Chem. Lett.*, 302, **43** (2013).

23) T. Sonoda, T. Maruo, Y. Yamasaki, N. Tsunoji, Y. Takamitsu, M. Sadakane, T. Sano, *J. Mater. Chem. A*, **3**, 857 (2015).

24) M.A. Camblor, A. Corma, S. Valencia, *Micropor. Mesopor. Mater.*, **25**, 59 (1998).

25) I. Schmidt, C. Madsen, C.J.H. Jacobsen, *Inorg. Chem.*, **39**, 2279 (2000).

26) L. Tosheva, V.P. Valtchev, *Chem. Mater.*, **17**, 2494 (2005).

27) G. Majano, A. Darwiche, S. Mintova, V. Valtchev, *Ind. Eng. Chem. Res.*, **48**, 7084 (2009).

28) M. Choi, K. Na, J. Kim, Y. Sakamoto, O. Terasaki, R. Ryoo, *Nature*, **461**, 246 (2009).

29) O. Larlus, S. Mintova, S.T. Wilson, R.R. Willis, H. Abrevaya, T. Bein, *Micropor. Mesopor. Mater.*, **142**, 17 (2011).

30) E.-P. Ng, D. Chateigner, T. Bein, V. Valtchev, S. Mintova, *Science*, **335**, 70 (2012).

31) T. Tago, H. Konno, Y. Nakasaka, T. Masuda, *Catal. Surv. Asia*, **16**, 148 (2012).

32) S. Inagaki, Y. Watanabe, Y. Nishita, Y. Kubota, *Chem. Lett.*, **42**, 186 (2013).

33) S. Inagaki, S. Shinoda, S. Hayashi, T. Wakihara, H. Yamazaki, J.N. Kondo, Y. Kubota, *Catal. Sci. Tech.*, **6**, 2598 (2015).

34) H. Koller, R.F. Lobo, S.L. Burkett, M.E. Davis, *J. Phys. Chem*., **99**, 12588 (1995).

35) N. Yamanaka, M. Itakura, Y. Kiyozumi, Y. Ide, M. Sadakane, T. Sano, *Micropor. Mesopor. Mater*., **158**, 141 (2012).

36) G.T. Kokotailo, S.L. Lawton, *Nature*, **203**, 621 (1964).

37) R.H. Daniels, G.T. Kerr, L.D. Rollmann, *J. Am. Chem. Soc.*, **100(10)**, 3097 (1978).

38) Q. Huo, E. Amherst, US Patent, 6 423 295 B1 (2002).

39) P.N. Joshi, A. Thangaraj, V.P. Shiralkar, *Zeolites*, *11*, 164 (1991).

40) O. Chiyoda, M.E. Davis, *Micropor. Mesopor. Mater.*, **32**, 257 (1999).

41) P. Wagner, Y. Nakagawa, G.S. Lee, M.E. Davis, S. Elomari, R.C. Medrud, S.I. Zones, *J. Am Chem. Soc.*, **122**, 263 (2000).

42) M.S. Rana, V. Samano, J. Ancheyta, J.A.I. Diaz, *Fuel*, **86**, 1216 (2007).

43) J.-E. Otterstedt, Y.-M. Zhu, J. Sterte, *Appl. Catal.*, **38**, 143 (1988).

44) J. Dwyer, D.J. Rawlence, *Catal. Today*, **18**, 487 (1993).

45) W. Vermeiren, J.-P. Gilson, *Top. Catal.*, **52**, 1131 (2009).

46) R.H. Harding, A.W. Peters, J.R.D. Nee, *Appl. Catal. A*, **221**, 389 (2001).

47) Y.-M. Chen, *Powder Technol.*, **163**, 2 (2006).

48) J. Biswas, I.E. Maxwell, *Appl. Catal.*, **63**, 197 (1990).

49) C. S. Triantafillidis, A.G. Vlessides, N.P. Evmiridis, *Ind. Eng. Chem. Res.*, **39**, 307 (2000).

50) G. Weber, M.H. Simonot-Grange, *Zeolites*, **14**, 433 (1994).

51) T. Ikeda, S. Inagaki, T. Hanaoka, Y. Kubota, *J. Phys. Chem. C*, **114**, 19641 (2010**).**

52) R.F. Lobo, M.E. Davis, *Micropor. Mater.*, **3**, 61 (1994).

53) Fischer, K., *N. Jb. Miner. Mh.*, **1**, 1 (1966).

Chapter Four

TEBOP^{2+}を用いた中シリカAFX型ゼオライトの合成

Novel synthetic technique to give AFX-type zeolite by using a bulky and rigid diquarternary ammonium (TEBOP^{2+})

*Small pore zeolites with large cavities have greatly attracted attention because of recently-developed industrial applications especially such as methanol or dimethyl ether-to-olefin (MTO or DTO) reaction and selective catalytic reduction (SCR) of NOx. **AFX**-type zeolites, possessing 8-ring channels and elongated large-cavity (**AFT** cage), have not been applied to such processes contrary to well-known **CHA**-type zeolites due to the limited Si/Al composition range which arises from a narrow synthesis window. In this work, a bulky and rigid N,N,N',N'-tetraethylbicyclo[2.2.2]oct-7-ene-2,3:5,6-dipyrrolidinium (TEBOP^{2+}) dication, which is already known to give **MSE**-type zeolites, was firstly used to synthesize **AFX**-type zeolites and successfully widen the synthesis window. The product Si/Al molar ratio in the range between 6 and 9 and the dihexahedron-based particle morphology are the remarkable features which have never been observed in conventional **AFX**-type zeolites. Crystallization of this novel **AFX**-type zeolite can be understandable based on guest/host relationship between the OSDA and the cage structure in **AFX**. An **FAU**-type zeolite, which has the considerable structural similarity with an **AFX**-type zeolite, is essential for the crystallization as a starting material. In addition to potentials for industrial applications, an investigation of crystallization kinetics is also discussed.*

4.1. Introduction

Zeolites are crystalline microporous aluminosilicates which comprise of corner-sharing TO_4 tetrahedra, where T is Si or Al atom. Applications of zeolites in catalysis, adsorption and separation have been industrially developed in past few decades. In particular, small-pore zeolites possessing 3-dimensional 8-ring channel system have recently drawn attention mainly because of excellent catalytic performances in selective catalytic reduction (SCR) of NOx and methanol or dimethyl ether-to-olefin (MTO or DTO) reaction.[1–4] Although many work focused on a **CHA**-type zeolite or its silicoaluminophosphate analogue (SAPO-34), there are other promising small-pore materials with **AEI**, **AFX**, **LEV**, **RTH** and **RHO** topologies. The synthesis windows of these zeolites are narrow compared to **CHA**, resulting limited compositions and particle sizes. Therefore, increasing a variety of synthetic routes of small-pore zeolites is highly desired for their industrial utilizations.

An **AFX**-type zeolite which is one of the small-pore zeolites has unique porous structure comprised of large and elongated **AFT** cage (0.55 × 1.35 nm) and small **GME** cage (0.33 × 0.74 nm).

The first **AFX**-type zeolite, especially known as SSZ-16, was firstly synthesized as a low-silica form (Si/Al < 6) by using a flexible 1,1'-tetramethylenebis(1-azoniabicyclo[2.2.2]octane) dication as an organic structure-directing agent (OSDA).[5,6] Lately **AFX**-type zeolites were obtained by other flexible OSDAs such as 1,1'-tetramethylenebis(1-azonia-4-azabicyclo[2.2.2]octane) ([Dab-4]$^{2+}$)[7,8] and 1,4-bis(*N*-methylpiperidinium)butane.[9] Recently a high-silica **AFX**-type zeolite with Si/Al higher than 16 was obtained by 1,3-bis(1-adamantyl)imidazolium which is a bulky and rigid monocationic OSDA.[10] It is noted that an **AFX**-type zeolite with medium Si/Al ratios in the range between 6 and 16 has not been directly synthesized so far.

AFX-type zeolites with Si/Al < 6 have disadvantages in terms of hydrothermal stability. The deactivation of copper-loading SSZ-16 catalyst in SCR of NOx was actually reported to be faster than that of ZSM-5 and SSZ-13 probably due to decreasing crystallinity.[11] On the other hand, the high-silica **AFX**-type zeolite with Si/Al > 16 cannot load so many copper ions, which would lead low catalytic activity in SCR. Actually small pore zeolites with Si/Al around 10 have showed excellent catalytic performance in SCR of NOx.[1,11,12] For this reason an **AFX**-type zeolite with medium aluminum content (6 < Si/Al < 16) is highly desired.

The uses of a variety of OSDAs have greatly contributed to the discoveries of new zeolites. One of the remarkable roles of OSDAs is templating, and there are a lot of examples where geometrical structures of guest OSDA cations reflected the size and shape of cavities of host zeolites. For example, tetramethylammonium cation is known to form sodalite cage.[13] 1-Adamantyltrimethylammonium cation was found intact within the cage-based pores of SSZ-13.[14] [Dab-4]$^{2+}$ dication gave very good fit to an **AFT**-cage in SSZ-16.[8] **AEI**[15], **EUO**[16], **IFW**[17], **MSE**[18], **SFW**[19] and many other zeolites showed very good fit between OSDAs and zeolitic frameworks. Therefore, rational choice of OSDA is quite important to obtain a zeolite with the desired cavity.

In this study, novel **AFX**-type zeolites crystallized in the presence of *N*,*N*,*N*',*N*'-tetraethylbicyclo[2.2.2]oct-7-ene-2,3:5,6-dipyrrolidinium (TEBOP^{2+}). The product Si/Al molar ratio in the range between 6 and 9 and the dihexahedron-based particle morphology are the remarkable features which have never been observed in conventional **AFX**-type zeolites. Besides the choice of OSDA, the use of an **FAU**-type zeolite as a starting material is essential for the successful crystallization.

4.2 Experimental

4.2.1 Synthesis of novel AFX-type zeolite using TEBOP^{2+}

N,*N*,*N*',*N*'-Tetraethylbicyclo[2.2.2]oct-7-ene-2,3:5,6-dipyrrolidinium diiodide (TEBOP^{2+}(I^-)$_2$) was synthesized according the reported procedure.[10] It was converted to hydroxide form as follows. Diaion® SA10A(OH) (Mitsubishi Chemical Co.) anion-exchange resin (398 g, corresponding to 716 mmol of exchange capacity) was added into a solution of the diiodide salt (99.0 g, 177 mmol) in

deionized water (600 mL). The whole mixture was kept statically for 120 h. After filtration, the aqueous solution was concentrated to 354 g to give 0.471 mmol/g $TEBOP^{2+}(OH^{-})_2$ based on HCl titration of the resulting solution. The anion-exchange rate was 94%.

An **FAU**-type zeolite with Si/Al = 10.3 which was used as a starting material for **AFX**-type zeolites was prepared as follows. **FAU** crystals with Si/Al = 5.3 (Tosoh, Co., namely HSZ-350HUA) were dispersed into 200 mL of 0.30 mol/L HNO_3 aqueous solution. The mixture was stirred at room temperature for 20 h. The solid was recovered by filtration, washed with water and dried at 80 °C for 5 h, which resulted in 19.2 g of the product as white powder.

The typical synthesis procedure to obtain an **AFX**-type zeolite with Si/Al = 8.4 is as follows. 0.435 g of **FAU** crystals prepared by the method described above was settled in 23 mL Teflon vessel. 0.672 g of deionized water, 1.066 g of $TEBOP^{2+}(OH^{-})_2$ aqueous solution (0.471 mmol/g) and 0.145 g of NaOH aqueous solution (3.47 mmol/g) were added and then the **FAU** crystals were dispersed into the solution. The molar composition of the synthesis mixture is 1.0 SiO_2−0.049 Al_2O_3−0.10 $TEBOP^{2+}(OH^{-})_2$−0.10 NaOH−20 H_2O. The hydrothermal treatment was conducted at 170 °C for 24 h using a 23 mL Teflon-lined steel autoclave. The solid was recovered by filtration and dried at 100 °C for 90 min. 0.361 g of the product was obtained as white powder. 0.348 g of the as-synthesized sample was calcined in a muffle furnace. The temperature was raised from room temperature to 600 °C under 1 °C/min of the ramping rate, and maintained at the same temperature for 2 h. Finally the sample was cooled to room temperature in ambient condition, which resulted in 0.337 g of the white calcined powder.

The **AFX**-type zeolite with slightly low-silica composition with Si/Al around 6 was synthesized by similar procedure described above. The used silica-alumina source was the **FAU**-type zeolite with Si/Al = 5.3 (Tosoh, Co., namely HSZ-350HUA) and the composition of the synthesis mixture was 1.0 SiO_2−0.094 Al_2O_3−0.10 $TEBOP^{2+}(OH^{-})_2$−0.10 NaOH−20 H_2O. The crystallization was carried out at 160 °C for 10 days statically.

4.2.2 Synthesis of conventional AFX-type zeolite using $[Dab\text{-}4]^{2+}$

1,1'-Tetramethylenebis(1-azonia-4-azabicyclo[2.2.2]octane) dibromide ($[Dab\text{-}4]^{2+}(Br^{-})_2$) was prepared as follows. 1,4-Diazabicyclo-[2.2.2]-octane (51.5 g, 450 mmol, Aldrich) was dissolved in 400 mL of acetone and 1,4-dibromobutane (17.7 g, 80.3 mmol, Wako) was added slowly at room temperature for a period of 15 min. Further 80 mL of acetone was added and the whole mixture was stirred for 37 h at room temperature. The resulted in white suspention was filtered and the white solid was washed with acetone and finally benzene. The obtained product was dried in a vacuum and the yield was 99.8% (35.7 g). The anion exchange was conducted by the similar way to convert $TEBOP^{2+}(I^{-})_2$ to $TEBOP^{2+}(OH^{-})_2$ described above. The concentration of the resulting [Dab-

4]$^{2+}$(OH^-)$_2$ aqueous solution was determined to 0.534 mmol/g and the anion exchange rate was 91%.

A conventional **AFX**-type zeolite was synthesized by a slightly modified procedure reported previously.[7,11] 31.37 g of [Dab-4]$^{2+}$(OH^-)$_2$ solution (0.574 mmol/g), 6.77 g of NaOH solution (3.68 mmol/g), 10.40 g of deionized water and 42.41 g of sodium silicate solution (SiO_2 :23.1 wt%, Na_2O :5.96 wt%, 31.37 g, prepared by dissolving colloidal silica (Ludox AS-40) into NaOH solution at 80 °C). The resultant solution was placed statically for 30 min at room temperature. 3.89 g of **FAU** crystals (Tosoh Co., namely HSZ-320HOA, Si/Al = 2.8) were added and dispersed into the solution. The molar composition of the synthesis mixture was 1.0 SiO_2−0.033 Al_2O_3−0.09 [Dab-4]$^{2+}$(OH^-)$_2$ −0.55 NaOH−20 H_2O. The mixture was transferred into a Teflon-lined 125-mL steel autoclave and settled in a convection oven at 140 °C for 43 h. The solid product was recovered by centrifugation and dried at 100 °C overnight, which resulted in 5.19 g of as-synthesized sample as white powder. 4.59 g of as-synthesized sample was calcined in a muffle furnace. The temperature was raised from room temperature to 520 °C under 1 °C/min of the ramping rate, and maintained at the same temperature for 3 h. Finally the sample was cooled to room temperature in ambient condition, which resulted in 4.35 g of the white calcined powder.

4.2.3 Characterization

The crystallinity and phase purity of the zeolite samples were examined by powder X-ray diffraction (XRD) on an Ultima-IV (Rigaku) using CuKα radiation at 40 kV and 20 mA. The Si/Al and Na/Al molar ratios in the bulk were determined by inductively coupled plasma, atomic emission spectrometer (ICP-AES, ICPE-9000, Shimadzu). Nitrogen adsorption and desorption isotherms at −196 °C were collected for the samples pretreated at 400 °C for 12 h on a BELSORP-max gas adsorption instrument (MicrotracBEL). The morphologies of zeolite samples were observed by scanning electron microscopy (SEM) on a JSM-7001F (JEOL) microscope. The organic contents included in the as-synthesized zeolite were determined by thermogravimetric and differential thermal analysis (TG-DTA, Thermo plus EVO II TG8120, Rigaku). The solid-state magic angle spinning nuclear magnetic resonance (MAS NMR) measurements were performed by using AVANCEIII 600 (Bruker) operating at 600 MHz for ^{1}H, 119.2 MHz for ^{29}Si and 156.4 MHz for ^{27}Al. All of the MAS NMR spectra were recorded at room temperature with samples in a 4 mm diameter ZrO_2 tube. The ^{29}Si chemical shifts were determined relative to hexamethylcyclotrisiloxane at −9.66 ppm. The dipolar-decoupling (DD) MAS NMR spectra were recorded by using 1024 pulses with a recycle time of 30 s at a spinning rate of 10 kHz. The ^{27}Al chemical shifts were determined by using an aqueous $Al(NO_3)_3$ solution, the resonance peak of which was adjusted to 0 ppm. The direct-excitation (DE) MAS NMR spectra were recorded by using 1024 pulses with a recycle time of 0.5 s at a spinning rate of 13 kHz. The C/N ratios of the as-synthesized samples were determined by CHN analysis (vario-EL III, elementar).

4.3 Results and discussion

4.3.1 Synthesis of AFX-type zeolite with various Si/Al ratios

We have successfully synthesized two **AFX**-type zeolites by using **FAU** zeolites with the different Si/Al compositions. Table 4.1 summarized the physicochemical properties of the obtained **AFX**-type zeolites. In Entry 1, high-silica **FAU** crystals (Si/Al = 10.3) were used as a starting material and the product Si/Al ratio was 8.4. In Entry 2, relatively low-silica **FAU** crystals (Si/Al = 5.3) were used to obtain the sample with Si/Al = 6.1. Figures 4.1a and 4.1b display the XRD patterns of as-synthesized **AFX**-type zeolites with Si/Al = 8.4 and 6.1, respectively. The **AFX** topology was confirmed and no impurity phase was observed in both samples. Figures 2c and 2d show XRD patterns of the calcined samples with Si/Al = 8.4 and 6.1, respectively. The framework structures were retained after calcination.

Figure 4.2 shows the particle morphologies of as-synthesized **AFX**-type zeolites. The sample with Si/Al = 8.4 consisted of particles with approximately 200 nm in size and both spherical and dihexahedral particles were observed. The sample with Si/Al = 6.1 consisted of dihexahedral particles with roughly 500 nm in size. This dihexahedral morphology is characteristic to our **AFX**-type zeolites and none of other **AFX**-type zeolites have such a morphology to our best knowledge.

Figure 4.3 shows the nitrogen adsorption-desorption isotherms of obtained **AFX**-type zeolites. Both samples showed the typical type-I isotherms, which promised the presence of micropores. The BET areas (S_{BET}), the external surface areas ($S_{ext.}$) and the micropore volumes (V_{micro}) were estimated and summarized in Table 4.1. S_{BET} and $S_{ext.}$ increased with decreasing particle sizes. In contrast, V_{micro} did not change significantly regardless of Si/Al ratios.

Conventional **AFX**-type zeolite was also synthesized using $[Dab\text{-}4]^{2+}$. The phase purities of as-synthesized and calcined samples were confirmed by XRD (Figure 4.4).

4.3.2 Composition analyses of obtained samples

The results from TG-DTA and ICP-AES analyses are summarized in Table 4. The amounts of Na and Al atoms per unit cell were determined by ICP-AES and the amounts of OSDA per unit cell were determined by TG-DTA. The TG and DTA curves are shown in Figure 4.5. The weight losses between 350 °C and 800 °C were assigned to combustion of OSDAs. The amount of Na increased with increasing the amount of Al. On the other hand, the amount of OSDA decreased with increasing Al. It indicates that the structure-direction of the OSDA becomes more important for the crystallization of **AFX**-type zeolites with lower Al contents. In contrast, the structure-direction of the inorganic cations probably has a significant role for the crystallization of relatively low-silica **AFX**-type zeolites due to high charge density of the alkali cations.

Calculation of the value (Na + 2 OSDA)/Al showed the balance between anionic and cationic charges. The value was almost 1 in the case of the high-silica sample (entry 1). On the other hand, the value was significantly smaller than 1 in the case of low-silica sample (entry 2). It suggests that the relatively low-silica as-synthesized sample was partly protonated.

Since the number of large **AFT** cages per unit cell is 2, the occupancies of the OSDA cation in the cages was calculated to be 85% and 78% in entry 1 and 2, respectively. These value indicated that the most of the **AFT** cages were supported by the OSDA cations.

The C/N ratios of samples 1 and 2 were 10.2 and 9.9, respectively. These values are almost consistent with the ideal value (10), indicating that the organics occluding in the as-synthesized samples were not degradated.

4.3.3 Investigation of Al states

Figure 4.6 shows ^{27}Al DE-MAS NMR spectra of the **AFX**-type zeolites with Si/Al = 8.4 and 6.1. Both the as-synthesized samples have tetrahedral Al atoms only.(Figures 4.6a and 4.6c) The chemical shifts of the peaks are almost the same. On the other hand, both the calcined samples included octahedral Al atoms and it indicated that the dealumination partly occurred by calcination.

Figure 4.7 shows ^{29}Si-MAS NMR spectra of the calcined **AFX**-type zeolites with Si/Al = 8.4 and 6.1. The high-silica sample showed three peaks on the DD-MAS spectrum at −99.9, −104.9 and −110.8 ppm, which are assigned to Q^4(0Al) ($Si(OSi)_4$), Q^4(1Al) ($Si(OAl)(OSi)_3$) and Q^4(2Al) ($Si(OAl)_2(OSi)_2$), respectively. The framework Si/Al molar ratio was determined to be 8.2 which is highly consistent with the bulk Si/Al ratio (8.4). The DD-MAS spectrum of the low-silica sample can be interpreted similarly, and the framework Si/Al ratio was calculated to be 7.0 which is slightly higher than the bulk Si/Al ratio (6.1), indicating the presence of non-framework Al. Q^3(0Al) ($Si(OSi)_3(OH)$) or other Q^3 peaks were not observed from DD and CP MAS spectra of both samples, promising the good crystallinity of obtained samples.

4.3.4. Evaluation of acid-stability

In order to evaluate acid-stability, the **AFX**-type zeolites with various Si/Al ratios were acid-treated. Figure 4.8 showed XRD patterns of the parent samples and the acid-treated samples. The comparison between the XRD peaks before and after the treatment reveals that the acid-resistance increased with increasing the parent Si/Al ratios. The sample with the highest Al amount showed considerable decrease in crystallinity as is observed on the XRD pattern (Figure 4.8d). In contrast, the sample with the lowest Al amount showed no decrease in crystallinity (Figures 4.8f).

4.3.5 Rational explanation for formation of AFX by $TEBOP^{2+}$

Discovery of the fact that $TEBOP^{2+}$ gives **AFX**-type zeolites with medium Al content can be rationally explained by guest/host relationship between the OSDA and the zeolite.

As mentioned in the introduction, flexible dicationic OSDAs are unable to give high-silica **AFX**-type zeolites with Si/Al higher than 6. The flexibility of OSDAs is likely to be disadvantage to form the **AFT** cage of the **AFX**-type zeolite and the only low-silica versions can crystallize with the aid of sodium cations which are plentiful in highly alkaline synthetic media. In contrast, a bulky and rigid monocationic OSDA (1,3-bis(1-adamantyl)imidazolium) gave a high-silica **AFX**-type zeolite with Si/Al higher than 16 due to highly hydrophobic nature of the OSDA. In terms of hydrophobicity, $TEBOP^{2+}$ has the medium character between the reported two OSDAs and it actually gave a novel **AFX**-type zeolite with the medium Al content in this work.

In addition to the bulkiness, rigidity and medium hydrophobicity, $TEBOP^{2+}$ is surprisingly sizable to the **AFT** cage of **AFX**. Figure 4.9 illustrates the **AFT** cage occluding the $TEBOP^{2+}$ cation. The size of $TEBOP^{2+}$ is 0.53 × 1.35 nm and that of the **AFT** cavity is 0.55 × 1.35 nm. The very good fitting is clearly seen from the figure. The other cage (**GME** cage, 0.33 × 0.74 nm) is not considered since it is too small to occlude large organic molecules.

By the way, an **MSE**-type zeolite is known to crystallize in the presence of $TEBOP^{2+}$.[20] The elongated **MSE** cage with 0.61 × 1.41 nm, which is slightly larger than the $TEBOP^{2+}$ cation. One of the reasons why the **MSE** phase was not observed in this work is explained by the better fitting of the OSDA to the **AFT** cage than to the **MSE** cage. Although ***BEA**[21], **MTW**[21] and **MOR**-type zeolites[22] can also crystallize in the presence of $TEBOP^{2+}$, the inhibition of these competing phases can be explained by the same reason. Another major factor for the single-phase crystallization of **AFX** is the use of **FAU** crystals as starting materials. The role of **FAU** crystals will be discussed in the following sections.

$TEBOP^{2+}$ is one of the derivatives of bicyclo[2.2.2]oct-7-ene-2,3:5,6-tetracarboxylic dianhydride (BOTD) which is commercially available. *N*,*N*'-Diisopropyl-*N*,*N*'-diethylbicyclo[2.2.2]oct-7-ene-2,3:5,6-dipyrrolidinium, which is another BOTD derivative, was known to give borosilicate **IFW**-type zeolite (SSZ-87) which has slightly larger cages than the **AFT** cage. These 3 examples (**AFX**, **MSE** and **IFW**) suggests diquaternary ammonium compounds derivated from BOTD are powerful and useful OSDAs to obtain zeolites with desired cavities.

It is noteworthy that the **AFX**-type zeolite is only aluminosilicate possessing **AFT** cages but the aluminophosphate with **AFT** topology (AlPO-52) is the other zeolitic material with **AFT** cages. Possibility for the crystallization of the aluminosilicate **AFT**-type zeolite in the presence of $TEBOP^{2+}$ is to be examined.

4.3.6 Comparison between $TEBOP^{2+}$ and $[Dab\text{-}4]^{2+}$

The bulky and rigid nature of $TEBOP^{2+}$ is expected to be advantage to form the **AFT** cage over conventional flexible diquats. The flexible OSDAs actually required alkaline-rich conditions for the syntheses of **AFX**-type zeolites, which caused the low-silica products (Si/Al < 6).[8,9] The weak structure-direction which arises from flexibility of an OSDA reasonably explains the importance of the alkaline cation as an inorganic structure-directing agent. In this work, the syntheses was carried out in dilute alkaline conditions ($NaOH/SiO_2$ = 0.1), which is firstly made possible by using the rigid OSDA.

In order to demonstrate the stronger structure-direction of $TEBOP^{2+}$ than that of a flexible diquat, $[Dab\text{-}4]^{2+}$ replaced $TEBOP^{2+}$ in our synthetic condition (input Si/Al = 5.3) and the synthetic procedures were carried out by the same way. The hydrothermal treatment at 160 °C for 6 days did not give the **AFX** phase (Figure 4.10). The synthesis mixture after hydrothermal treatment was highly yellowish and the lower stability of $[Dab\text{-}4]^{2+}$ in hydrothermal alkaline conditions probably caused the inhibition of the crystallization in addition to the weak structure direction. The investigation at lower temperature is therefore required to confirm the difference of the structure-direction between $TEBOP^{2+}$ and $[Dab\text{-}4]^{2+}$. After 15 days of treatment at 140 °C, the $[Dab\text{-}4]^{2+}$ system did not produce **AFX**-type zeolites. These investigations indicates that the rigid nature of $TEBOP^{2+}$ is one of the key factors for the strong structure-direction to the **AFX** phase.

4.3.7 Investigation of crystallization kinetics

FAU crystals have been widely used for the syntheses of **AFX**-type zeolites.[7–11] There is significant similarity between **AFX** and **FAU** which can be briefly stated that the both topologies can be constructed by *d6r* building units. This structural similarity is probably essential factor for the crystallization of **AFX** and we carried out detailed research to unveil the role of **FAU** crystals.

The use of amorphous material as silica and alumina sources instead of **FAU** crystals completely suppressed the crystallization of **AFX**. Only amorphous phase was obtained (Figure 4.11).

Figure 4.12 shows crystallization of the **AFX**-type zeolite (Entry 2 in Table 1) with time course reflected by XRD patterns. After 14 h, no **AFX** phase crystallized. After 24 h, the XRD peaks originated from **AFX** appeared, and then the crystallization rapidly proceeded. After 72 h, the crystallinity reached at about 80% (defined by the peak intensity at 2 θ = 21.8°). After 236 h, the **FAU** phase disappeared and the **AFX**-type zeolite was obtained as single phase. The crystallinity at this point was defined to be 100%. The course of crystallization was carried out in the presence of **FAU** crystals and we did not observe amorphization of the **FAU** crystals. Figure 4.13 shows the crystallization curves at 150−180 °C. Nucleation rate drastically increased with raising synthetic temperature.

Figure 4.14a shows the FE-SEM images of the starting **FAU** crystals with a wide range of sizes in

100−500 nm. Figure 4.14b shows **FAU** crystals which were recovered after 14 h. There is no significant difference between these two samples on FE-SEM images. The solid yield was almost 100% and the Si/Al ratios also did not change significantly. However, the solid NMR analyses revealed the significant difference of the state of aluminum before and after the hydrothermal treatment. Figure 4.15 displays ^{27}Al DE-MAS NMR spectra of starting **FAU** crystals and the sample recovered just before the appearance of the **AFX** phase (14 h). The starting **FAU** crystals (typical USY) showed both tetrahedral and octahedral Al. On the other hand, the sample after the hydrothermal treatment has tetrahedral Al only. Figure 4.16 shows ^{29}Si DD and CP MAS NMR spectra before and after the hydrothermal treatment. the starting **FAU** crystals have three peaks at −95.5, −101.5 and −107.2 ppm which are assigned to Q^4(2Al), Q^4(1Al) and Q^4(0Al), respectively. The framework Si/Al ratio was estimated to be 9.4 and the difference from bulk Si/Al ratio (5.2) is explained by the existence of non-framework (octahedral) Al observed on the ^{27}Al NMR spectrum. The sample after 14 h has four peaks at −89.6, −94.7, −101.6 and −106.6 ppm which are attributed to Q^4(3Al), Q^4(2Al), Q^4(1Al) and Q^4(0Al), respectively. The framework Si/Al ratio was estimated to 5.2 and this value is almost the same as the bulk Si/Al ratio (5.2), promising the absence of non-framework Al atoms as indicated by ^{27}Al NMR. This investigation suggests that the recrystallization of **FAU** crystals occurred in the crystallization inductive period of **AFX**. The recrystallized **FAU** crystals are probably better precursor for the **AFX**-type zeolite than the starting **FAU** crystals.

Figure 4.18 shows the FE-SEM images of the sample soon after the nucleation of **AFX** (with 12% of crystallinity). The characteristic dihexahedron particles were observed as aggregates with other particles. Since the pure **AFX** sample consisted of dihexahedron-based particles only, we assumed that the dihexahedron particles were **AFX** crystals and the others were **FAU** crystals. Interestingly, each **AFX** particle contacted on **FAU** crystals. For example, the right area on Figure 4.17a displays an **AFX** crystal aggregated with **FAU** crystals. The center area on Figure 4.17b displayed an **AFX** nanocrystal on an **FAU** crystal. The aggregates of **AFX** and **FAU** crystals indicated that the nucleation and crystal growth of **AFX** occurred near **FAU** surface.

As mentioned above, there is considerable structural similarity between **FAU** and **AFX**. The role of **FAU** in crystallization of **AFX** is speculated as illustrated in Figure 4.18. Dissoluted silicate species from **FAU** crystals is also thought to have structural similarity with **AFX**. Plausible silicate fragments that have partial structures of **AFX** is illustrated in the figure. This fragments probably directed or strongly promoted the nucleation of **AFX**.

Mesoscopic crystallization kinetics of **AFX** is speculated shown in Figure 4.19. As fragments of **AFX** (illustrated as blue points) which are dissolved from **FAU** crystals (already recrystallized) diffused from **FAU** surfaces, they are likely to be degradated or disordered since such fragments are thermodynamically unstable(Figure 4.19a). The concentration of the fragments of **AFX**, therefore, is

the highest on the external surface of **FAU** crystals. Nucleation of **AFX** crystals occurred near **FAU** crystals (Figure 4.19b), and the grown **AFX** crystal is likely to contact on **FAU** crystals (Figure 4.19c). This aggregate was actually observed in FE-SEM observation. Finally, pure and isolated **AFX** crystals obtained after complete dissolution of **FAU** crystals (Figure 4.19d). Although incomplete dihexahedron particles are actually observed in the samples, they were probably formed by relatively faster dissolution of **FAU** crystals (If the **FAU** crystals in Figure 4.19c rapidly dissolved, incomplete **AFX** crystals are remained.).

4.4 Conclusion

Novel **AFX**-type zeolites were successfully obtained by using $TEBOP^{2+}$, which is a bulky and rigid dicationic OSDA. The product Si/Al ratios were in the range between 6 and 9, which had never been established by conventional techniques. The dihexahedral crystals were characteristic to this **AFX** zeolites. The acid-resistance improved with increasing product Si/Al ratios, promising for applications where zeolites are exposed in acidic media. The guest/host relationship between **AFX** framework and $TEBOP^{2+}$ cation reasonably explains the strong structure-direction of $TEBOP^{2+}$. **FAU** crystals were essential for the crystallization of **AFX**. The **AFX** crystals were grown on **FAU** crystals, which suggested that the nucleation of **AFX** occurred near **FAU** surface.

Table 4.1. Physicochemical properties of **AFX**-type zeolites obtained in this work.

Entry	Input Si/Al[a]	Output Si/Al[a]	N_2 adsorption measurements			Particle size[d] [nm]
			S_{BET}[b] [m^2/g]	$S_{ext.}$[c] [m^2/g]	V_{micro}[c] [cm^3/g]	
1[e]	10.3	8.4	708	12.4	0.288	200
2[f]	5.3	6.1	632	4.5	0.252	500

a Determined by ICP-AES. All silica and alumina in the synthesis mixtures came from **FAU** crystals.
b Estimated by BET analysis.
c Estimated by *t*-plot method.
d Estimated by FE-SEM observation.
e Synthesized at 160 °C for 10 d under static conditions.
f Synthesized at 170 °C for 24 h under static conditions.

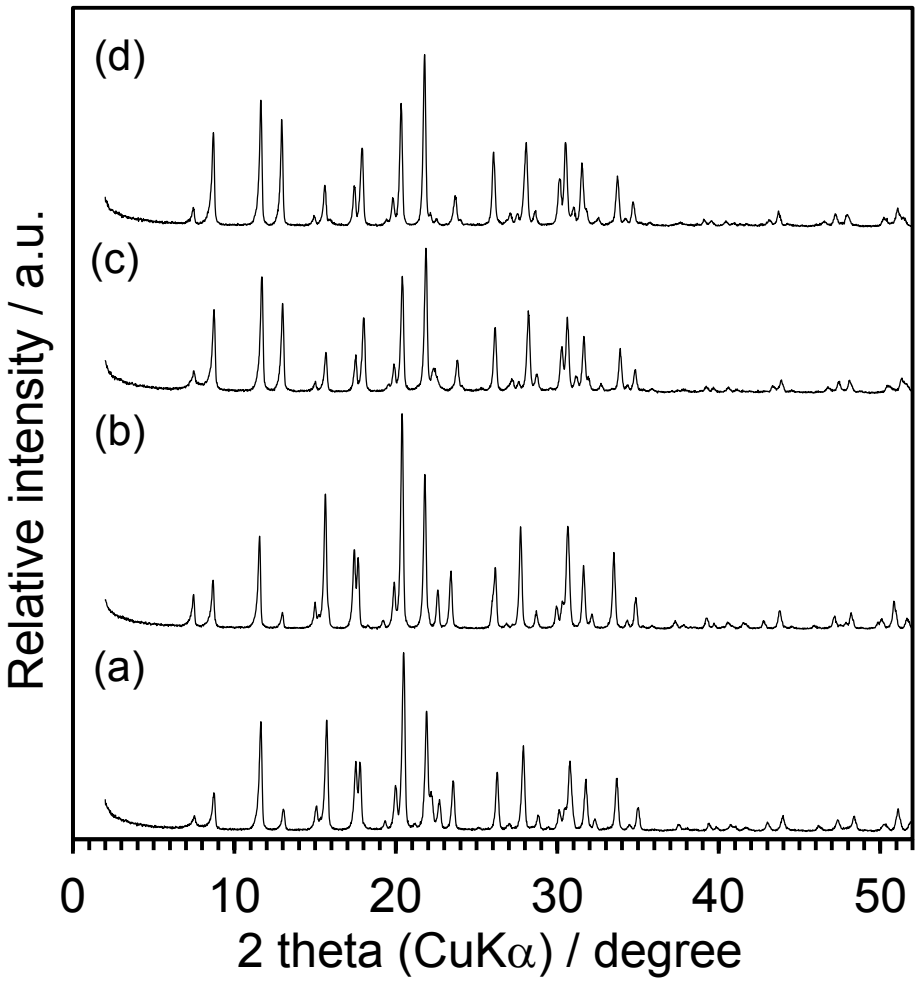

Figure 4.1. The XRD patterns of as-synthesized and calcined **AFX**-type zeolites obtained by using $TEBOP^{2+}$ as an OSDA. (a) as-synthesized, Si/Al = 8.4, (b) as-synthesized, Si/Al = 6.1, (c) calcined, Si/Al = 8.4 and (d) calcined, Si/Al = 6.1.

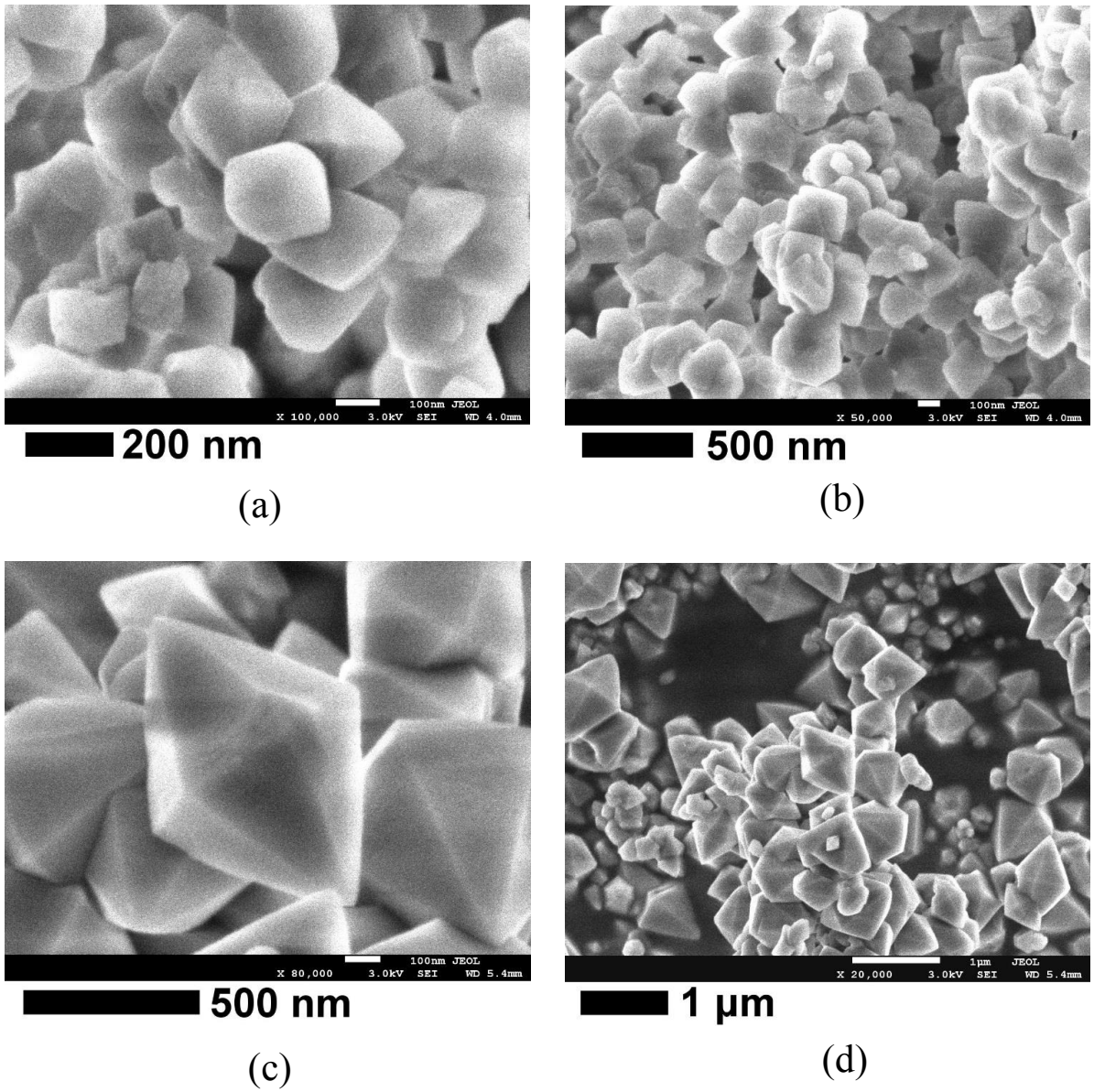

Figure 4.2. FE-SEM images of as-synthesized **AFX**-type zeolites with (a, b) Si/Al = 8.4 and (c, d) Si/Al = 6.1, respectively. These samples were synthesized by using $TEBOP^{2+}(OH^{-})_2$ as an OSDA.

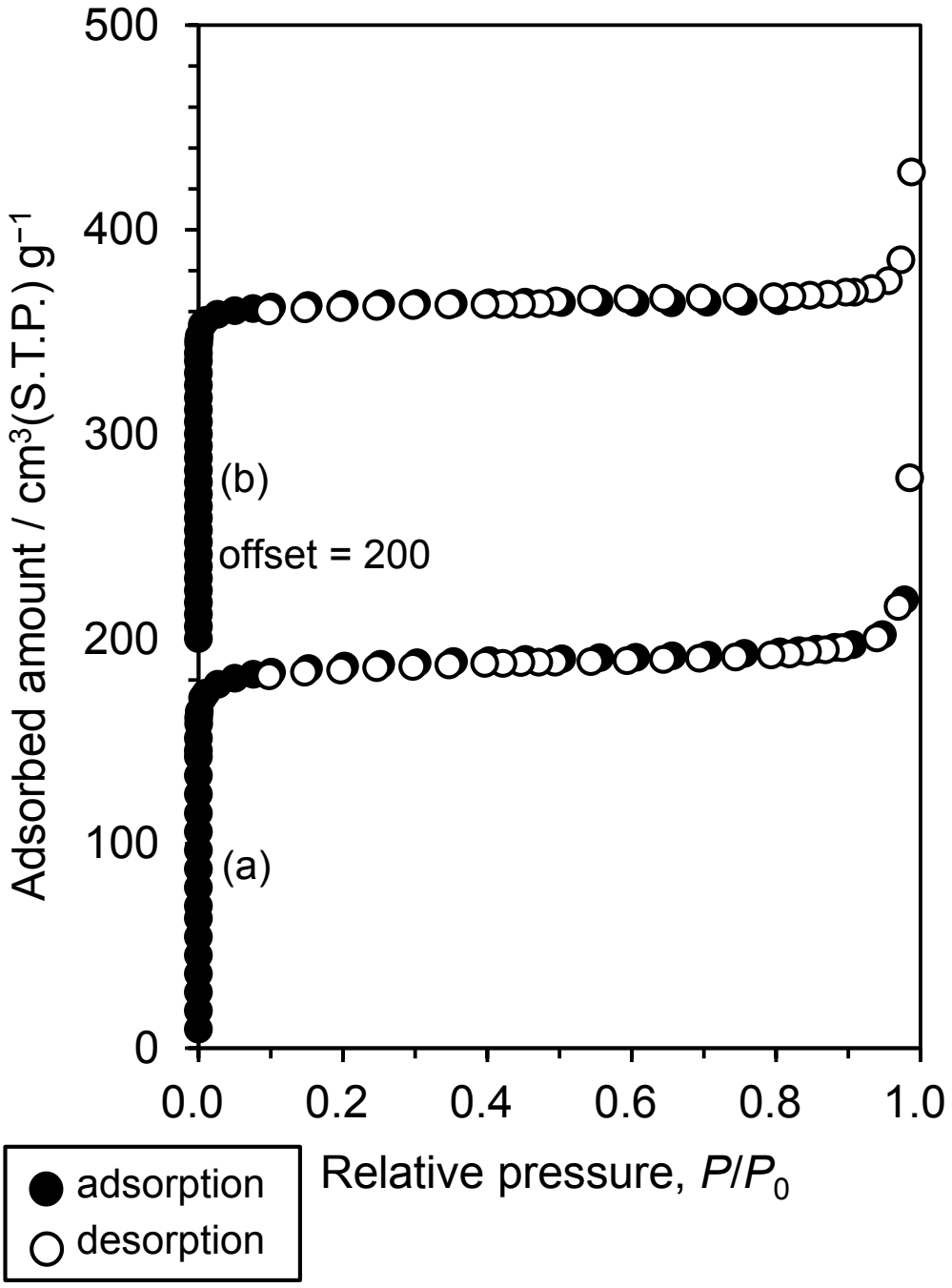

Figure 4.3. Nitrogen adsorption-desorption isotherms of **AFX**-type zeolites (a) with Si/Al = 8.4 and (b) Si/Al = 6.1, respectively.

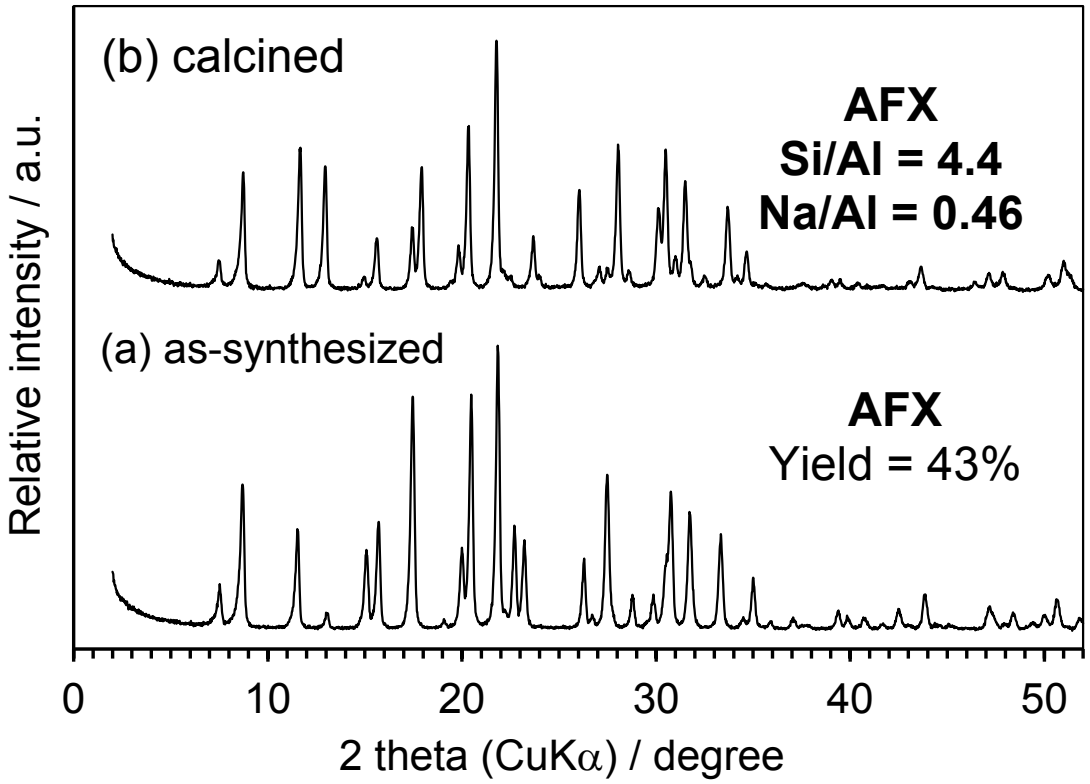

Figure 4.4. Powder XRD patterns of conventional (a) as-synthesized and (b) calcined **AFX**-type zeolites synthesized by using $[Dab\text{-}4]^{2+}$ as an OSDA.

Table 4.2. Amounts of Al, Na and OSDA in **AFX**-type zeolites.

Entry	Number per unit cell			(Na + 2 OSDA)
	Al [a]	Na [a]	OSDA [b]	/Al
1	5.11	1.69	1.71	1.00
2	6.76	2.57	1.57	0.84

[a]Determined by ICP-AES.

[b]Determined from the weight loss from 350−800 °C in TG curve.

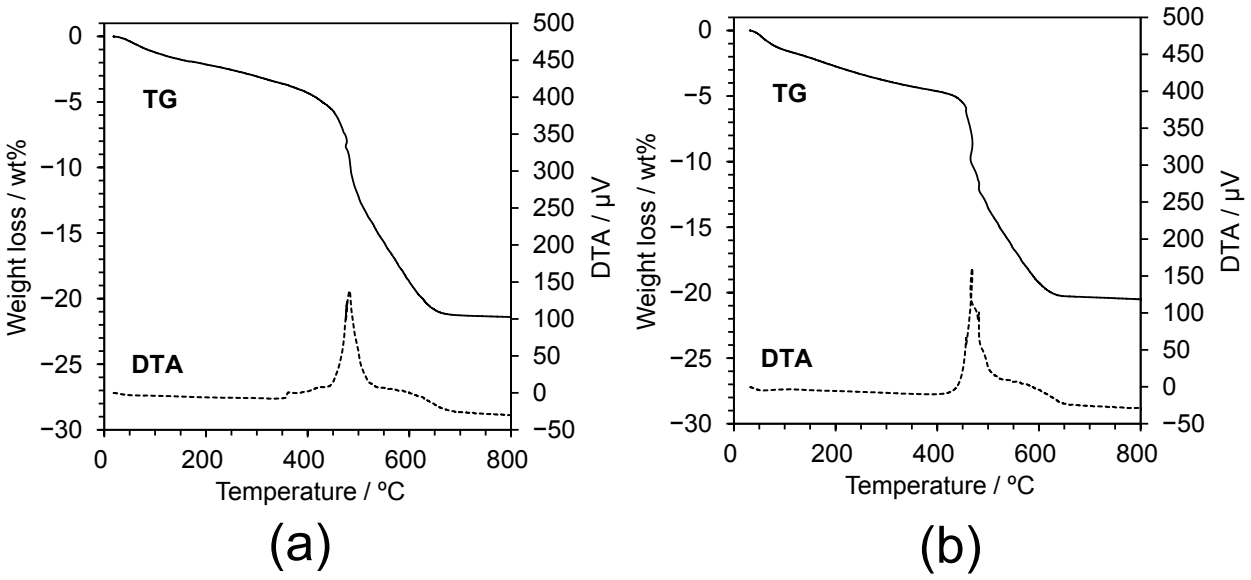

Figure 4.5. TG and DTA curves of as-synthesized **AFX**-type zeolite (a) with Si/Al = 8.4 (b) and Si/Al = 6.1.

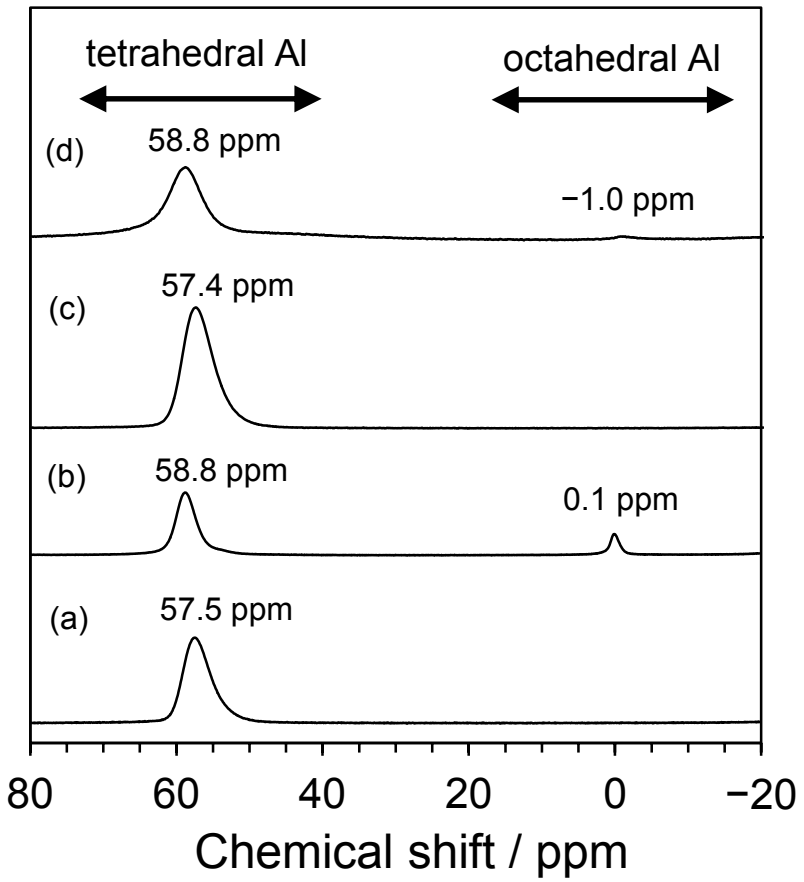

Figure 4.6. ^{27}Al DE-MAS NMR spectra of **AFX**-type zeolites. (a) as-synthesized, Si/Al = 8.4, (b) calcined, Si/Al = 8.4, (c) as-synthesized, Si/Al = 6.1 and (d) calcined Si/Al = 6.1, respectively.

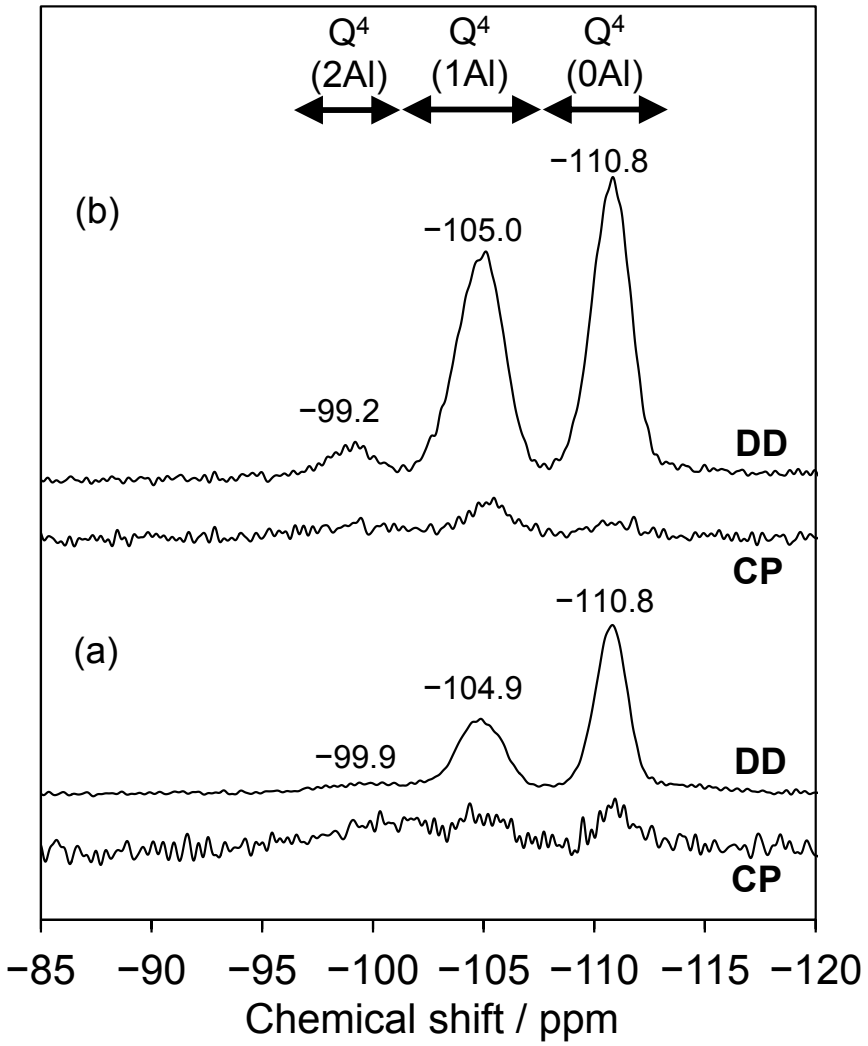

Figure 4.7. ^{29}Si MAS NMR spectra of **AFX**-type zeolites. (a) bulk Si/Al = 8.4, framework Si/Al = 8.2 and (b) bulk Si/Al = 6.1, framework Si/Al = 7.0), respectively.

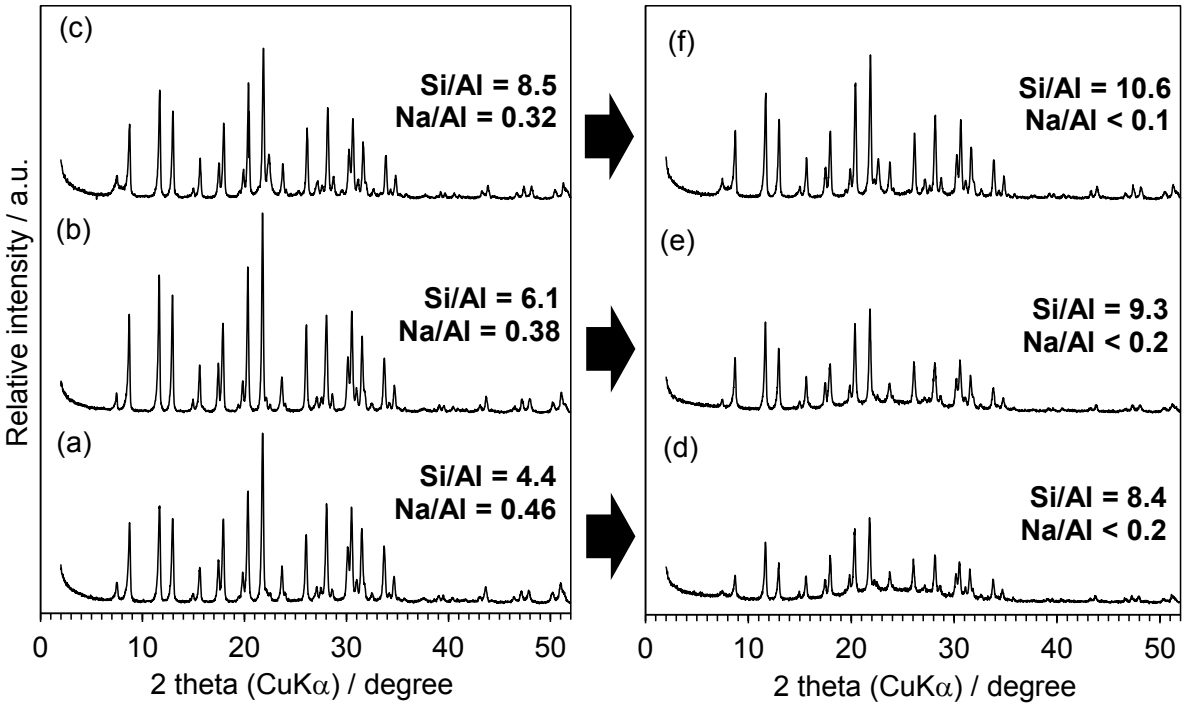

Figure 4.8. Acid-treatments of the **AFX**-type zeolites with various Si/Al ratios. Parent samples (a) with Si/Al = 4.4, (b) Si/Al = 6.1 and (c) Si/Al = 8.5, respectively. Acid-treated samples of (d) sample a, (e) sample b and (f) sample c, respectively.

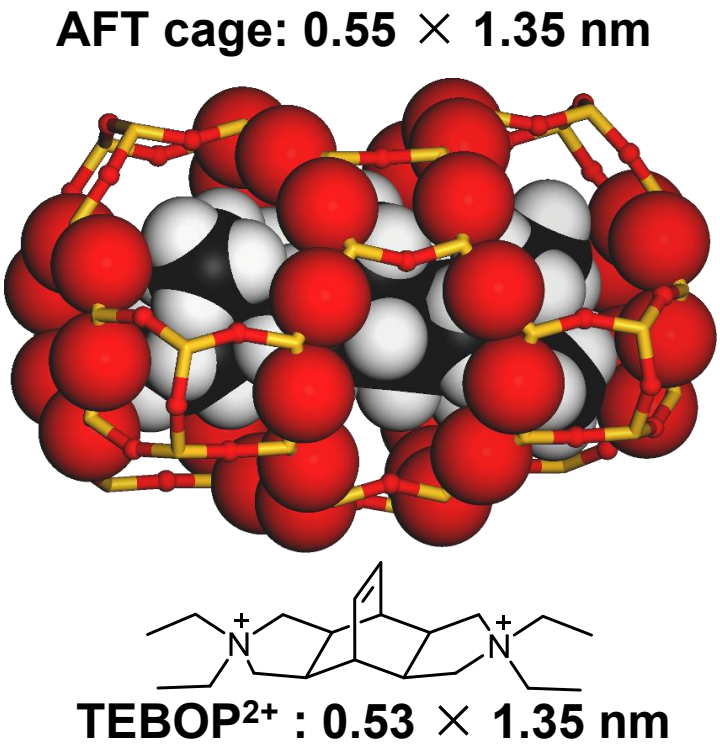

Figure 4.9. Illustration of the **AFT** cage occluding one $TEBOP^{2+}$ cation. Some oxygen atoms of the **AFT** cage and the $TEBOP^{2+}$ cation were drawn by CPK model to confirm the fitting visually.

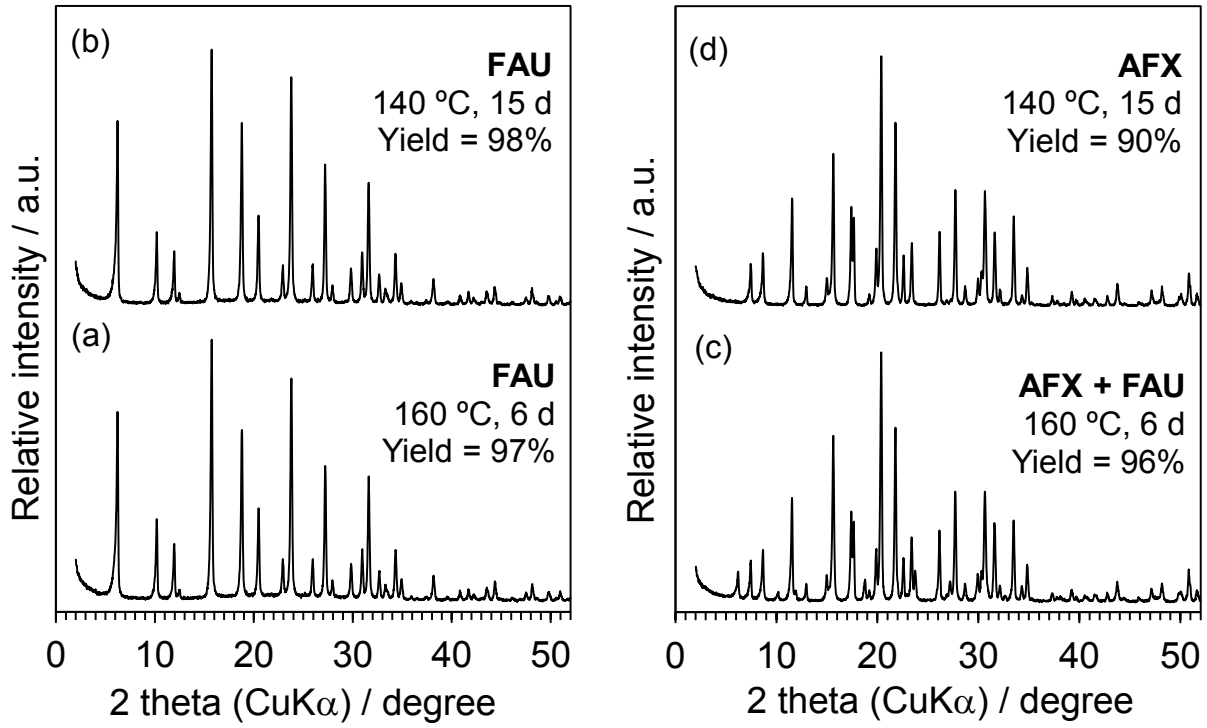

Figure 4.10. XRD patterns of samples obtained by using (a, b) $[Dab\text{-}4]^{2+}$ and (c, d) $TEBOP^{2+}$, respectively. The flexible $[Dab\text{-}4]^{2+}$ did not give any **AFX** phases. On the other hand, $TEBOP^{2+}$ gives **AFX** phases in wide synthetic temperatures.

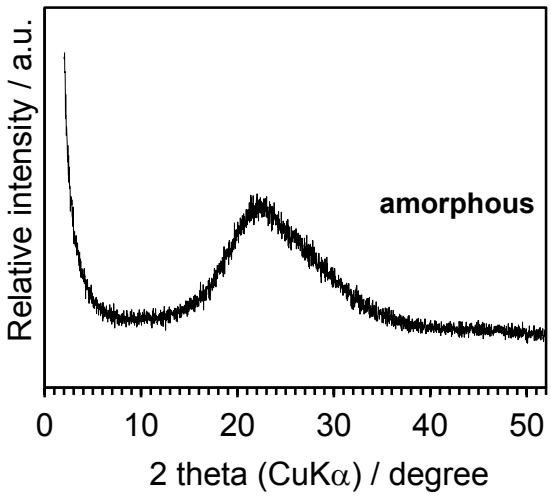

Figure 4.11. The product obtained from amorphous silica (Ludox AS-40) and sodium aluminate used as starting materials. The composition of the synthesis mixture was the same as Entry 2 in Table 1 and the synthesis was carried out at 170 °C for 7 days under static conditions.

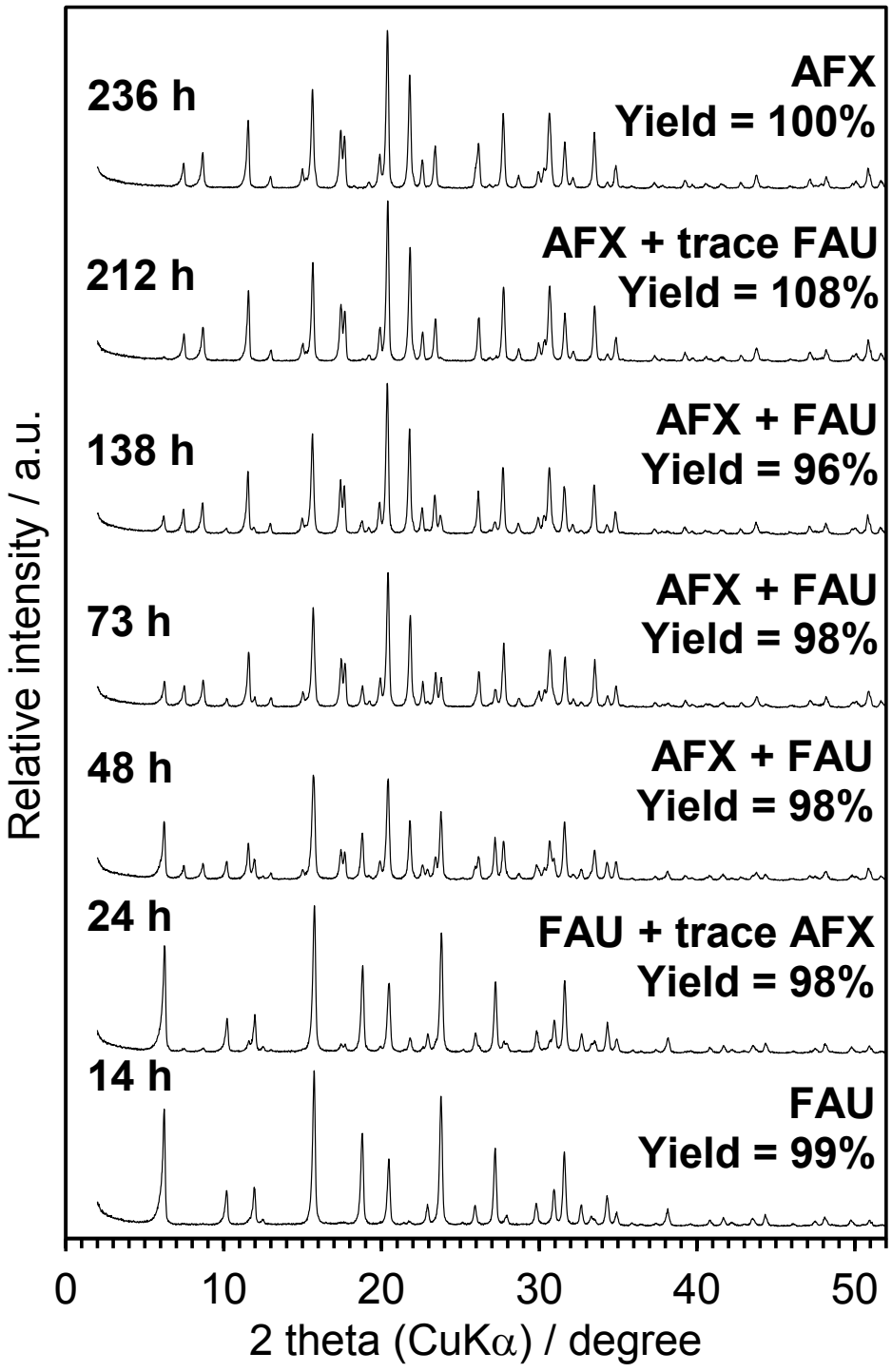

Figure 4.12. Time-course crystallization of the **AFX**-type zeolite at 160 °C as reflected in the powder XRD patterns of the as-synthesized samples. The Si/Al ratio of used **FAU** is 5.3.

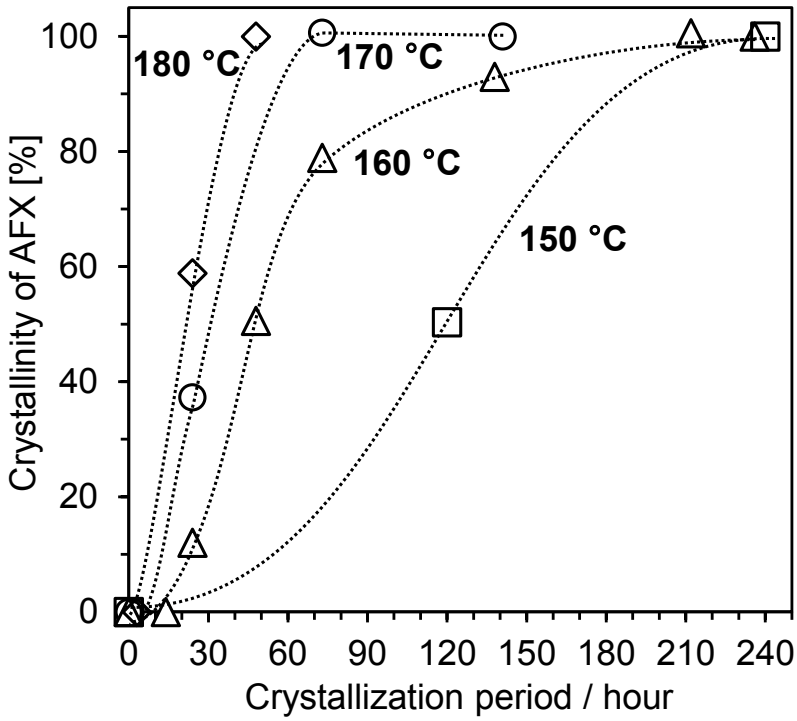

Figure 4.13. Crystallization curves of **AFX**-type zeolite at 150−180 °C. (Crystallinity was defined as the relative intensity at 2 θ =21.8°)

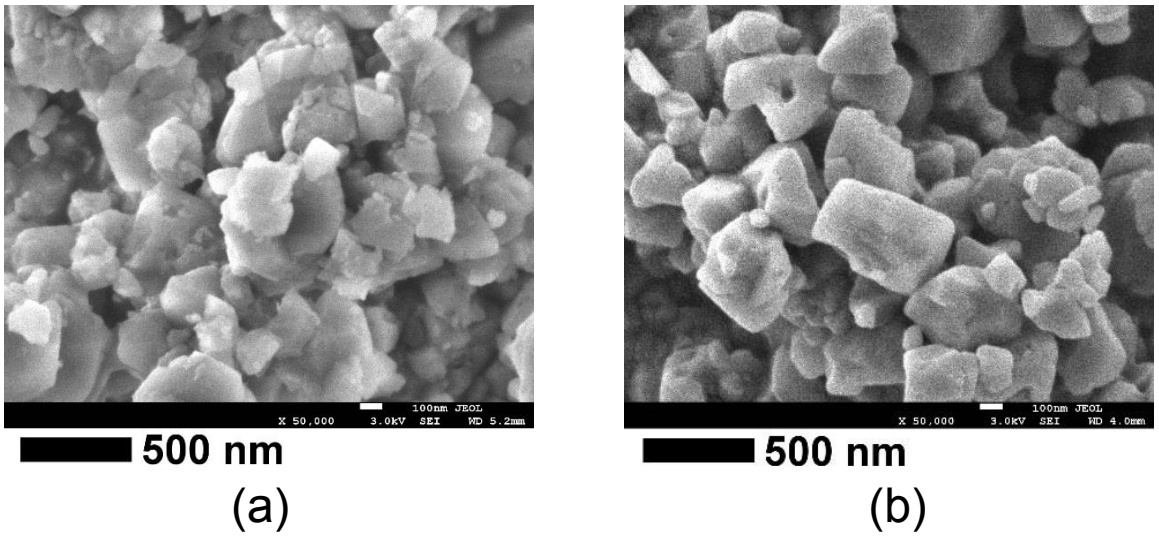

Figure 4.14. FE-SEM images of (a) starting **FAU** crystals and (b) **FAU** crystals obtained after 14 h.

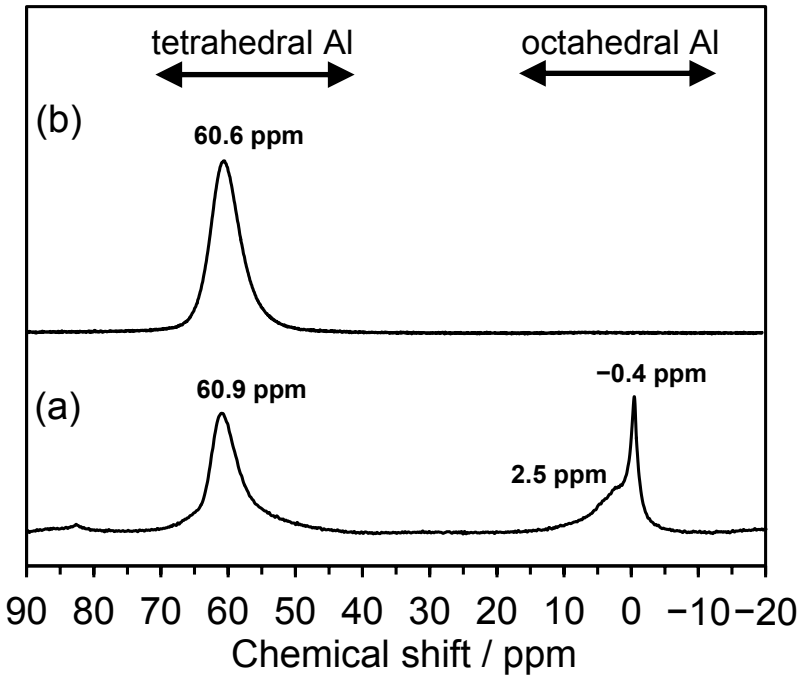

Figure 4.15. ^{27}Al DE-MAS NMR spectra of (a) starting **FAU** with Si/Al = 5.3 and (b) **FAU** with Si/Al = 5.2 recovered after 14 h.

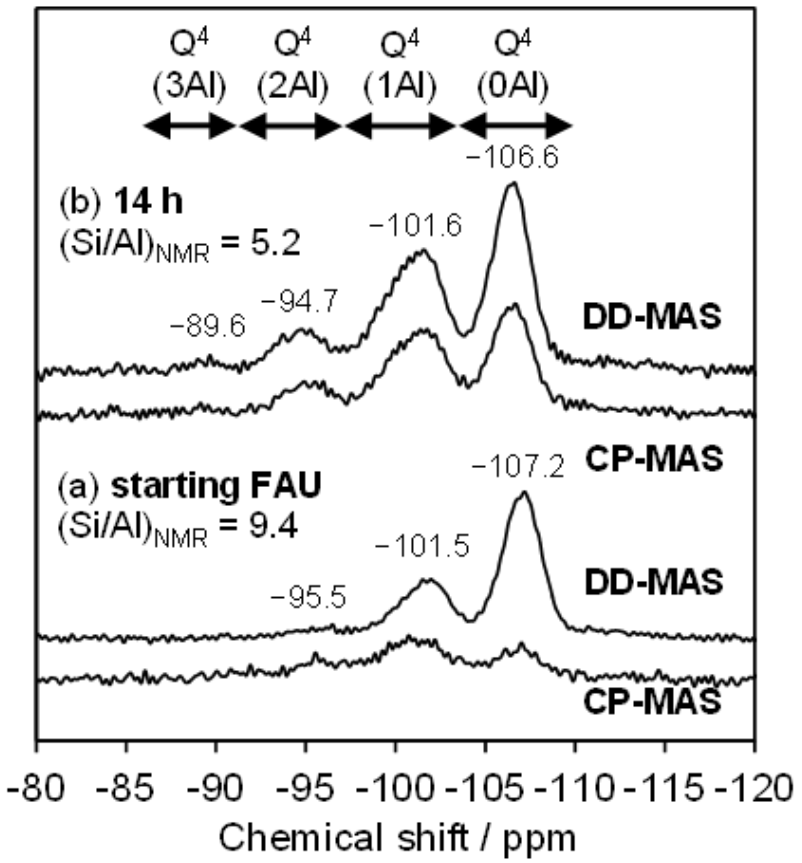

Figure 4.16. ^{29}Si MAS NMR spectra of (a) starting **FAU** crystals and (b) **FAU** crystals recovered after 14 h.

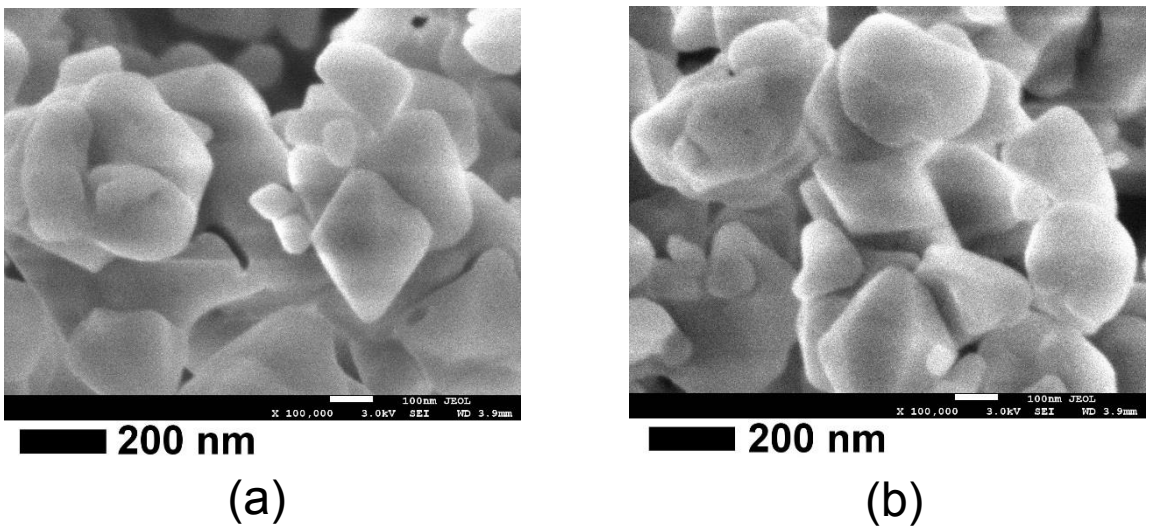

Figure 4.17. FE-SEM images of the sample recovered after 24 h (mixture of **FAU** and **AFX** crystals). Dihexahedral **AFX** crystals were observed as aggregates with **FAU** crystals.

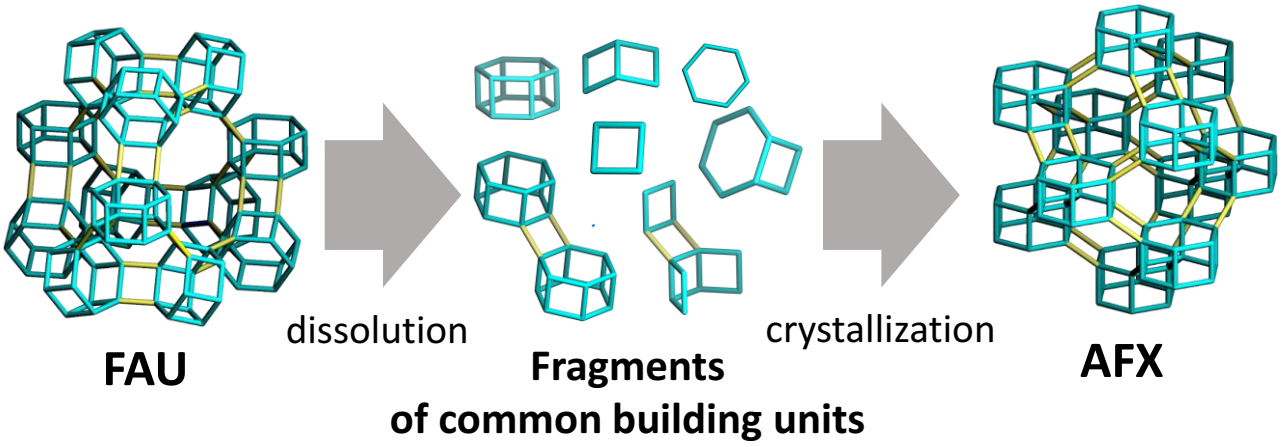

Figure 4.18. Microscopic illustration of the hydrothermal conversion of **FAU** into **AFX**.

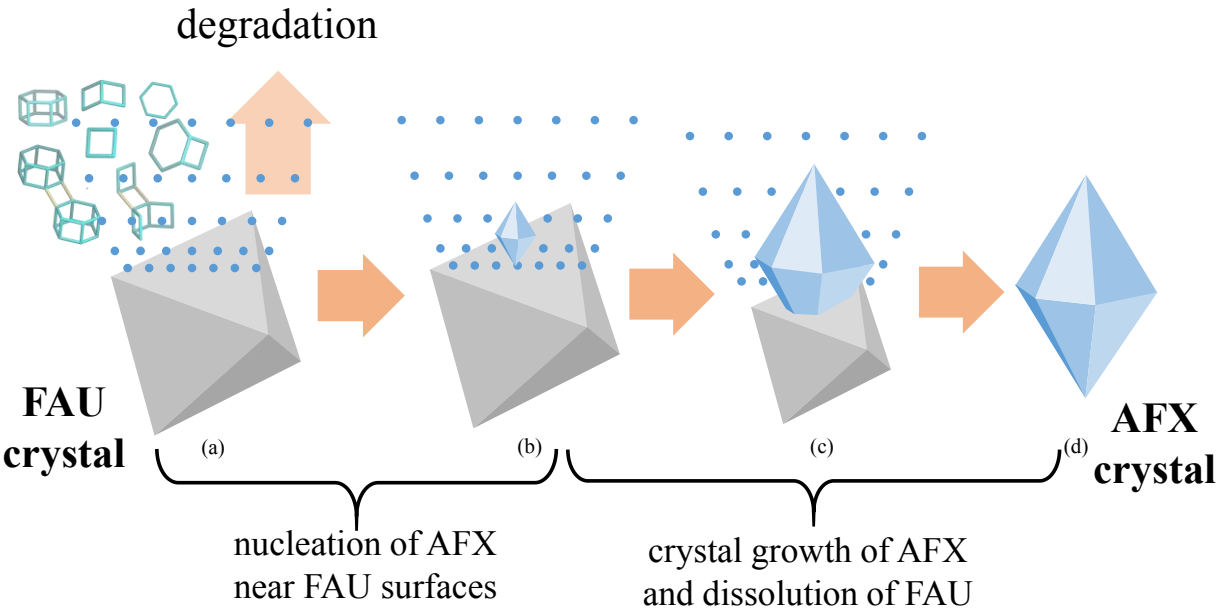

Figure 4.19. Mesoscopic illustration of crystallization of **AFX**-type zeolite on **FAU**-type zeolite crystals.

4.5 References

(1) Bull, I.; Boorse, R. S.; Jaglowski, W. M.; Koermer, G. S.; Moini, A.;Patchett, J. A.; Xue, W. M.; Burk, P.; Dettling, J. C.; Caudle, M. T. U.S. Patent 0,226,545, 2008.

(2) Olsbye, U.; Svelle, S.; Bjørgen, M.; Beato, P.; Janssens, T. V. W.; Joensen, F.; Bordiga, S.; Lillerud, K. P. *Angew. Chem., Int. Ed.* 2012, *51*, 5810.

(3) Vora, B.V.; Marker, T. L.; Barger, P. T.; Nielsen, H. R.; Kvisle, S.; Fuglerud, T. *Stud. Surf. Sci. Catal.* 1997, *107*, 87

(4) Moliner, M.; Martínez, C.; Corma, A. *Chem. Mater.* 2014, *26*, 246

(5) Zones, S. I. U.S. Patent 4,508,837, 1985

(6) Zones, S. I. Van Nordstrand, R. A.; *Zeolites* 1988, *8*, 409

(7) Zones, S. I., U.S. Patent 5,194,235 (1993).

(8) Lobo, R. F.; Zones, S. I.; Medrud, R. C. *Chem. Mater.* 1996, *8*, 2409

(9) Jackowski, A.; Zones, S. I.; Hwang, S. -J.; Burton, A. W. *J. Am. Chem. Soc.* 2009, *131*, 1092

(10) Archer, R. H.; Zones, S. I.; Davis, M. E., *Micropor. Mesopor. Mater.* 2010*, 130*, 255

(11) Fickel, D. W.; D'Addio, E.; Lauterbach, J. A.; Lobo, R. F., *Appl. Catal., B: Environ*. 2011, *102*, 411

(12) Moliner, M.; Franch, C; Palomares, E.; Grill, M.; Corma, A. *Chem. Commun.* 2012, *48*, 8264

(13) Davis, M. E.; Lobo, R. F., *Chem. Mater.* 1992, *4*,756

(14) Zones, S. I.; Van Nordstrand, R. A., *Zeolites* 1988, *8*, 166

(15) Wagner, P; Nakagawa, Y; Lee, G. S.; Davis, M. E.; Elomari, S; Medrud, R. C; Zones, S. I., *J. Am. Chem. Soc.* 2000, *122,* 263

(16) Moini, A.; Schmitt, K. D.; Valyocsik, E. W.; Polomski, R. F., *Zeolites* 1994*, 14*, 504

(17) Smeets, S.; McCusker, L. B.; Baerlocher, C.; Xie, D.; Chen, C. -Y.; Zones, S. I. *J. Am. Chem. Soc.* 2015, *137*, 2015

(18) Koyama, Y; Ikeda, T; Tatsumi, T; Kubota, Y. *Angew. Chem. Int. Ed.* 2008, *47*, 1042

(19) Xie, D.; McCusker, L. B.; Baerlocher, C.; Zones, S. I.; Wan, W; Zou, Xiaodong, *J. Am. Chem. Soc.* 2013, *135*, 10519

(20) Calabro, D. C.; Cheng, J. C.; Crane Jr, R. A.; Kresge , C. T.; Dhingra, S. S.; Steckel, M. A.; Stern, D. L.; Weston S. C. U.S. Patent 6,049,018, 2000

(21) Shibata, T.; Suzuki, S.; Kawagoe, H.; Komura, K.; Kubota, Y.; Sugi, Y.; Kim, J.-H.; Seo, G. *Micropor. Mesopor. Mater.* 2008, *116*, 216

(22) Inagaki, S.; Watanabe, Y.; Nishita, Y; Kubota, Y. *Chem. Lett.* 2013, *42*, 186

Chapter Five

$Me_2Pr_2N^+$を用いた新規骨格ゼオライトYNU-5の合成

Synthesis of YNU-5 with novel framework structure by using $Me_2Pr_2N^+$ as an organic structure-directing agent

We report synthesis and preparation procedures of YNU-5 zeolite catalyst, which is a novel aluminosilicate zeolite characterized with the unique 12-12-8-ring channel system. Synthesis was hydrothermally conducted using dimethyldipropylammonium as an organic structure-directing agent (OSDA). Although several competing phases such as **MOR**, **MFI** *and* ***BEA** *were observed, single-phase crystallization was established by careful tuning water content in the synthesis mixture. We found a good correlation between the water content during synthesis and the framework density of crystalline product, which may have been reflected by the degree of hydrophobic interaction between silicate and OSDA. YNU-5 was obtained both under static and tumbling conditions and the crystallization time was shorter under tumbling. Acid-treatment with tuned concentration and temperature gave YNU-5 catalyst with a desired Si/Al ratio. The Si/Al ratios of YNU-5 were in the range from 9 to 350 according to concentration and/or temperature of the acids.*

5.1 Introduction

Zeolite is crystalline aluminosilicate composed of TO_4 (T = Si or Al) tetrahedral units that share the corner oxygens. The materials with large or extra-large, multi-dimensional pores are especially promising from the viewpoint of catalytic application and/or separation, because such large pores are capable of adsorbing bulky molecules and allowing them to diffuse inside pores.

The use of organic structure-directing agents (OSDAs) have contributed the discoveries of new zeolites.[1)] In the meantime, the correlation between pore systems and OSDA structure has become clearer.[2)] Hydrophobicity of OSDAs were also found to be a crucial factor for the syntheses of high-silica molecular sieves.[3)]

Although a hydrophilic OSDA ($C/N^+ < 10$) tended to have narrow synthesis window especially in terms of Si/Al composition (SSZ-39 (**AEI**)[4,5)], SSZ-16 (**AFX**)[6,7)] and MCM-68 (**MSE**)[8)]), we developed new synthesis method to obtain SSZ-39 in wider composition range.[9)] The method may be effective to withdraw the potential of relatively hydrophilic OSDAs.

In this situation, we have been successful in the synthesis of new aluminosilicate zeolite with 12-12-8-ring (+ independent 8-ring) pore system by using dimethyldipropylammonium ($Me_2Pr_2N^+$), one of the simple hydrophilic tetraalkylammonium-type compound, as the OSDA. The new zeolite, YNU-5, crystallizes with a favorable chemical composition (Si/Al = 9) and the aluminum content is controllable through dealumination by means of appropriate acid-treatment. We report herein the synthesis and detailed structure of YNU-5. In addition, dimethyl ether (DME)-to-olefin (DTO) reaction was investigated by using YNU-5 as a catalyst.

5.2 Experimental

5.2.1. Synthesis of YNU-5 by adjustment of water amount with evaporation technique

The YNU-5 zeolite was synthesized as follows. Aqueous $Me_2Pr_2N^+OH^-$ solution (2.097 mmol g^{-1}, 16.21 g, 34.0 mmol), aqueous NaOH solution (3.200 mmol g^{-1}, 9.37 g, 30.0 mmol), aqueous KOH solution (3.153 mmol g^{-1}, 9.53 g, 30.0 mmol), and 21.39 g of colloidal silica (Ludox AS-40, DuPont, 41.3 wt% SiO_2, 8.83 g-SiO_2, 147.0 mmol-SiO_2) were mixed in a 150 mL Teflon beaker and stirred for 3 h on a hot plate with maintaining the mixture at 60 °C, which allowed for 20.26 g of water to evaporate. The 20.26 g of water included 4.41 g of rinsing water used during the procedure. This evaporation procedure is not required if more concentrated solutions of hydroxides are used and the use of excess rinsing water is avoided. Nevertheless, heating on a hot plate to obtain clear solution is essential. After cooling down to room temperature, 4.99 g of **FAU**-type zeolite (Tosoh HSZ-350HUA, Si/Al = 5.3) was added, and the mixture was stirred for 10 min. It should be noted that the **FAU**-type zeolite adsorbs considerable water (ca. 20−26 wt%) when stored under atmospheric conditions in our laboratory. Therefore, we usually estimate the water content by TG analysis just before use. For this example, the SiO_2, Al_2O_3, and H_2O contents were estimated to be 63.9 wt%, 10.2 wt%, and 25.9 wt%, respectively. The resulting mixture, with a final weight of 45.64 g and a molar composition of $0.265SiO_2$ (from **FAU**) – $0.735SiO_2$ (from colloidal silica) – $0.025Al_2O_3$ (from **FAU**) – $0.17Me_2Pr_2N^+OH^-$ – 0.15NaOH – 0.15KOH – $7.0H_2O$, was placed in a 125-mL Teflon-lined stainless-steel autoclave within a convection oven and maintained at 160 °C for 165 h. After cooling the autoclave to room temperature, the obtained solid was separated by filtration, washed several times with de-ionized water and dried overnight. The as-synthesized YNU-5 zeolite was obtained as a white powder (6.84 g). To remove the OSDA occluded in the pores, the as-synthesized YNU-5 (5.02 g) was

heated in a muffle furnace with the temperature raised from ambient to 550 °C at a rate of 1.5 °C min^{-1} and held for 6 h. Finally, the sample was cooled to room temperature to give the calcined product (6.84 g) as a white powder (Si/Al = 9).

5.2.2 Synthesis by adjustment of water amount without using evaporation technique

Aqueous $Me_2Pr_2N^+OH^-$ solution (Sachem Inc., 2.706 mmol g^{-1}, 12.57 g, 34.0 mmol), aqueous NaOH solution (12.75 mmol g^{-1}, 2.357 g, 30.0 mmol), aqueous KOH solution (8.996 mmol g^{-1}, 3.340 g, 30.0 mmol), 21.20 g of colloidal silica (Ludox AS-40, DuPont, 41.3 wt% SiO_2, 8.75 g-SiO_2, 145.7 mmol-SiO_2), and pure water (Milli-Q, 1.346 g, 74.7 mmol) were mixed in a 150-mL Teflon beaker. The entire mixture was maintained at at 60 °C on a hot plate and stirred for 2 h, which is essential to obtain the clear solution. The molar composition is $1.0SiO_2$ – $0.233Me_2Pr_2N^+OH^-$ – 0.206NaOH – 0.206KOH – $9.20H_2O$. To this solution (solution A), 4.85 g of **FAU**-type zeolite similar to that used in the previous section was added (the weight ratio of the solution and the **FAU**-type zeolite is 89.2 : 10.9). The mixture was well stirred manually using a Teflon spatula in a 125-mL Teflon liner, which was then installed in a stainless-steel Parr autoclave and rotated at 20 rpm in a convection oven at 160°C for 4 days. This is an example of the scale of 400 mmol SiO_2 and the molar composition of the final mixture just before heating is $0.265SiO_2$ (from **FAU**) – $0.735SiO_2$ (from solution A) – $0.025Al_2O_3$ (from **FAU**) – $0.17Me_2Pr_2N^+OH^-$ – 0.15NaOH – 0.15KOH – $7.1H_2O$. The calcination procedure used to remove the OSDA was the same as the previous section.

5.2.3. Synthesis of YNU-5 starting from dealuminated FAU-type zeolites

The use of dealuminated **FAU**-type zeolite as SiO_2 and Al_2O_3 sources was effective for the reproducible synthesis of highly pure YNU-5. In a 200 mL round-bottom flask, **FAU**-type zeolite (Tosoh, HSZ-350HUA, #35UA3Y02, Si/Al=5.5, typically 10 g) was suspended in 0.15 and 0.25 mol L^{-1} HNO_3 solution (60 mL $(g\text{-sample})^{-1}$) and stirred at room temperature for 24 h to give dealuminated samples (in >95 wt% recovery) with Si/Al ratios of 6.85 and 8.70, respectively. The same procedure as that described in Section 2.3.1 was then performed using the dealuminated sample. The starting molar compositions were $0.343SiO_2$ (from **FAU** with Si/Al 6.85) – $0.657SiO_2$ (from colloidal silica)

– $0.025Al_2O_3$ (from **FAU**) – $0.17Me_2Pr_2N^+OH^-$ – 0.15NaOH – 0.15KOH – $7.0H_2O$ and $0.435SiO_2$ (from **FAU** with Si/Al 8.70) – $0.565SiO_2$ (from colloidal silica) – $0.025Al_2O_3$ (from **FAU**) – $0.17Me_2Pr_2N^+OH^-$ – 0.15NaOH – 0.15KOH – $7.0H_2O$. YNU-5 with high purity was obtained in both cases.

5.2.4 Post-synthesis modification

To convert the calcined sample to its proton form, some different procedures of acid-treatments were applied to the calcined YNU-5 samples. Direct dealumination of the calcined YNU-5 was preliminary conducted by treatment with x mol L^{-1} HNO_3 solution (60 mL (g-sample)$^{-1}$) in a 200 mL round bottom flask at 80 °C for 2 h where x was 2.0, 0.5, 1.0, 2.0, 3.0, 4.0, 5.0, 6.0, or 13.4. To stabilize the framework, more favorable treatment with aqueous HNO_3 solution was performed at the same liquid/solid ratio under reflux conditions in a 130 °C oil bath for 24 h.

To obtain the proton form with minimal dealumination, ion-exchange of the calcined samples to the NH_4^+-form was performed using NH_4NO_3 solution followed by calcination at 550 °C as a common procedure.[10)]

5.2.5 Characterization

The crystallinity and phase purity of the zeolite catalysts were examined using powder X-ray diffraction (XRD; Ultima-IV, Rigaku) with Cu Kα radiation at 40 kV and 20 mA. The Si/Al molar ratios in the bulk were measured by inductively coupled plasma, atomic emission spectroscopy (ICP-AES; ICPE-9000, Shimadzu). Nitrogen (–196°C) and argon (–186°C) adsorption-desorption isotherms were measured for samples (ca. 100 mg) pre-treated at 400°C for 12 h on a gas adsorption instrument (BELMAX, MicrotracBEL). The morphologies of the zeolite catalysts were observed by means of field emission scanning electron microscopy (FE-SEM; JSM-7001F, JEOL). Solid-state magic angle spinning nuclear magnetic resonance (MAS NMR) measurements were performed using a spectrometer (AVANCEIII 600, Bruker) operated at 600 MHz for ^1H and 119.2 MHz for ^{29}Si. All MAS NMR spectra were recorded at room temperature with a 4 mm diameter ZrO_2 tube. The ^{29}Si chemical shifts were determined based on that of hexamethylcyclotrisiloxane at –9.66 ppm. Dipolar-decoupling (DD) MAS NMR measurements were conducted using 1024 pulses with a recycle time of 30 s at a spinning rate of 10 kHz. Thermogravimetric/differential thermal analyses (TG-DTA)

were performed on a Thermo plus EVO II TG8120 (Rigaku) instrument for as-synthesized sample and TG-DTA2000SA (BrukerAXS) for calcined sample. The as-synthesized sample (ca. 10 mg) was heated from room temperature to 800 °C at 10 °C min^{-1} in a dry air flow at 30 mL min^{-1}. The calcined sample was heated from room temperature to 210 °C at 10 °C min^{-1} in a dry air flow at 50 mL min^{-1}.

5.3 Results and Discussion

5.3.1 Effect of water content on structure-direction

First, the effect of the H_2O/SiO_2 ratios in the synthesis mixtures on the product phases was investigated, and the results are shown in Figure 5.1. When the H_2O/SiO_2 ratio was 10, i.e., under relatively water-rich conditions, the **MFI** phase crystallized. When the ratio was 7, YNU-5 crystallized as a pure form, which did not appear at the ratio of 4, but **MSE** phase crystalized instead. The formation of **MSE**-type zeolite using $Me_2Pr_2N^+$ is not peculiar, because the product is known as UZM-35.[11] When the H_2O/SiO_2 ratio was 3, the ***BEA** phase appeared. To the best of our knowledge, this is the first beta zeolite obtained with only $Me_2Pr_2N^+$ as the OSDA. Tetraethylammonium with the same molecular weight and C/N^+ molar ratio is known to crystallize the ***BEA** phase in a very wide synthesis window, whereas the ***BEA** phase is relatively difficult to crystallize when $Me_2Pr_2N^+$ is used. Overall, the significant effect of a slight deviation of the H_2O/SiO_2 ratios on the phase selections was unexpected.

We found a good correlation between the starting H_2O/SiO_2 ratio and the framework density. The FD_{Si} value (T/nm^3)[12] can be used as a representative value for the FD. The (H_2O/SiO_2 ratio, FD_{Si}) values for the **MFI**, **MSE** and ***BEA** phases are (18.4, 10), (16.4, 4), and (15.3, 3), respectively. The FD of the main product phase thus decreases as the amount of water in the synthesis mixture decreases. A higher H_2O/SiO_2 ratio in the synthesis mixture promoted crystallization of a zeolitic phase with a higher FD, which probably reflects the degree of interaction between the OSDA and silicate. In a concentrated starting mixture, silicate species and OSDA interact more efficiently, so that more OSDA is incorporated. As another result, regions were found where the hydrophobic interaction was so favorable that the new large-pore zeolite YNU-5 crystallized by the use of a simple OSDA. The

structure-direction by inorganic as well as organic species seems to be essential for the crystallization of YNU-5. The isolated 8-ring straight channels of YNU-5 were filled with K^+ [33] because organic species cannot enter the isolated channels. The OSDAs are occluded in the 12-ring channel and probably play a role in accumulating the building blocks including the isolated 8-rings.

When the input molar ratio of H_2O/SiO_2 was 7, reproducible crystallization of pure YNU-5 was observed; however, when the ratio was slightly greater or smaller than 7 (for example, 8 or 6), trace amounts of **MFI** or a dense phase were present as contaminants, respectively (Figure 5.2). The present case is not common because the typical H_2O/SiO_2 ratios in the typical alkaline media are 30–50.

Figures 5.3a, 5.3b show powder XRD patterns of the YNU-5 zeolite in the as-synthesized and calcined forms, respectively. The framework structure remains noticeably stable after calcination. The Si/Al ratio of the solid was lower than that used in the synthesis mixture (9 vs. 20), which explains the non-quantitative yield (ca. 50%) of the product.

It should be noted that YNU-5 can be synthesized under both static and rotation conditions, although there were no differences between the products, based on powder XRD patterns (not shown) and FE-SEM images (Figure 5.4).

5.3.2 Time-course of crystallization

Figure 5.5 shows a time-course of crystallization under static conditions. Almost only **FAU** as the starting material was found after 16 h, and a slight trace of an amorphous halo was observed. The bulk Si/Al ratio was increased slightly to 7.2. At this point, the Na/Al and K/Al ratios were 0.25 and 0.39, respectively, which indicates that K was already being preferentially taken up. After 28 h, a mixture of **FAU** and YNU-5 was obtained without any amorphous phase, which suggest that crystallization of YNU-5 proceeded in coexistence with **FAU**. After 45 h, the crystallization of YNU-5 was complete, at which point the Si/Al, Na/Al, and K/Al ratios were 9.5, 0.11 and 0.55, respectively. The single phase of YNU-5 remained with no impurities even though the crystallization time was extended to 165 h. However, the heating period should not be as long as 240 h due to a tendency for slight contamination with impurity phases.

5.3.3 Control of Si/Al molar ratio by acid-treatment

During dealumination with nitric acid over a wide range of concentration (0.1–13.4 mol/L), the framework structure was retained. Figure 5.6 shows that the Si/Al molar ratios of dealuminated samples varied from 30 to 250, according to the acid concentration. Although tunable dealumination by simple acid treatment is difficult in some cases, YNU-5 was readily dealuminated as with other pentasil zeolites such as ***BEA** and **MSE**, and the Si/Al ratios were flexibly controlled. There was a temperature-dependence, where treatment at higher temperature resulted in a higher degree of dealumination. Alkali cations were exchanged to protons during these treatments.

Dealumination of zeolites typically produces defect sites that would lower the framework stability. Therefore, the thermal stability of dealuminated samples was investigated. Figure 5.7 shows powder XRD patterns of dealuminated samples before and after thermal treatment at 650 °C. Figures 5.7a–5.7d show XRD patterns of samples dealuminated under various conditions. The highest Si/Al value among the obtained samples was 350 and a desired Si/Al ratio in the range from 9 to 350 was realized without decrease in crystallinity by tuning the acid concentration. Dealumination is generally accompanied by the formation of defect sites; therefore, the samples were heated at 650 °C to investigate their thermal stability (Figures 5.7a'–5.7d'). The non-dealuminated sample possessed sufficient thermal stability (Figure 5.7a'). The sample treated at 80 °C showed a considerable decrease in crystallinity, which suggests the presence of site defects (Figure 5.7b'). Interestingly, the sample treated under reflux conditions exhibited high thermal stability (Figures 5.7c' and 5.7d'). These results can be summarized as follows. The crystallinity of the samples dealuminated at 80 °C was considerably decreased after the thermal treatment. In contrast, the samples dealuminated at >100 °C possessed higher thermal stability and no loss of crystallinity was observed after the thermal treatment at 650 °C. Based on our previous investigations, Si-migration is considered to play some role in the framework stabilization.[13,14)]

5.3.4 Solid NMR investigation

The amount of defect sites was clearly estimated by ^{29}Si MAS NMR as shown in Figure 5.8. Before the acid-treatment, no Q^3 peak was observed. In the spectrum of the sample that was treated under milder conditions, there was a large Q^3(0Al) peak. The Q^3/Q^4 peak area ratio was 31/69. In contrast, the sample treated under severer conditions showed a much smaller Q^3 peak. The Q^3/Q^4 ratio was

19/81, which indicates that some defect sites were diminished under the severer conditions.

These results are consistent with the assumed Si migration we reported as the cause of the framework stabilization.[13,14] Framework stabilization by Si-migration under such mild conditions compared to our previous techniques such as steaming at >500 °C was unexpected. The mechanism for the diminishment of defect sites could be explained as follows. First, neighboring Si atoms are hydrolyzed with the aid of acid and the resultant monosilicic acid species move to site defects (= silanol nests) via condensations. This corresponds to the apparent movement of site defects to adjacent sites as illustrated in Figure 5.9. After repeating this process many times, the defect sites can finally reach the outer surface of the crystal. Although a similar stabilization process has been classically considered in the steaming process,[15] the results here indicate that Si-migration also occurs during acid-treatment at temperatures as low as 100 °C in aqueous acid solution.

The ^{27}Al MAS NMR spectra of parent YNU-5 (YNU-5 just calcined), YNU-5 with Si/Al = 39 (treated with 2 molL^{-1} nitric acid at 80 °C for 2 h), YNU-5 with Si/Al = 57 (treated with 3 molL^{-1} nitric acid at 80 °C for 2 h), and YNU-5 with Si/Al = 350 (or 304) (treated with 13.4 molL^{-1} nitric acid using 130 °C oil bath for 24 h) are shown in Figure 5.10. Figures 5.10a−c clearly shows major peaks in the region of 50−60 ppm, which correspond to tetrahedral aluminum and indicate that most of the aluminum in the parent and dealuminated samples is incorporated into the framework. Although there is a minor signal attributed to extra-framework Al (octahedral Al) at around 0 ppm, here we discuss only the peaks at around 50−60 ppm. It should be noted that the samples other than highly dealuminated YNU-5 exhibit a shoulder peak at around 53 ppm accompanied by a major peak at around 56 ppm. On the spectrum of highly dealuminated sample, relative intensity was inverted and the peak around 53 ppm became a single peak, which indicates that the framework aluminum atoms inside isolated 8-ring channels are more difficult to remove by acidic hydrolysis. It can be assumed that the diffusion of water molecules into the isolated 8-ring straight channels is significantly restricted and dealumination from the 8-ring channels is relatively difficult. According to the literature [40], chemical shift is a function of the T−O−T angle (T = Al or Si) in the framework and the higher-field resonance (right peak) in the ^{27}Al MAS NMR spectrum corresponds to a wider T−O−T angle. For T1 and T5 located only inside the isolated 8-ring straight channel, the T−O−T angles are wider than other T sites based on the crystallographic data [33] (The numbering of T sites is also

based on Ref. 33). Therefore, this factor is also consistent with the NMR peak assignment based on the accessibility of water molecule (oxonium ion) to 12-ring channels compared with that to isolated 8-ring channels for.

5.3.5 Enhancement of the framework regularity with thermal treatment at 550 °C

Important results were obtained regarding the behavior of YNU-5 during the thermal treatment at 550 °C that is the pretreatment temperature before performing the catalytic reaction. Before and after the thermal treatment, the change of powder XRD patterns was consistent with that can be seen in Figures 5.11d and 5.11d'. A prominent effect was observed on ^{29}Si and ^{27}Al MAS NMR spectra of stabilized YNU-5(57) as shown in Figures 5.12 and 5.13, respectively. Whereas the ^{29}Si and ^{27}Al MAS NMR peaks are broad for unstabilized YNU-5(60), the peaks became remarkably sharp for stabilized YNU-5(57) after treatment at 550 °C. This may be due to the enhancement of the regularity of **YFI** framework. The well-resolved peaks should be helpful for the differentiation of T-sites and, in turn, site-specific introduction of heteroatoms.

5.4 Acknowledgment

This work was financially supported in part by the Japan Science and Technology Agency (JST) for the project of Creation of Innovative Functional Materials with Advanced Properties by Hyper-nano-space Design in the CREST program (Project code: JPMJCR1423). We thank Dr. Takuji Ikeda (AIST) for technical support for conducting structural analysis of YNU-5.

5.5 Conclusion

An unconventional hydrothermal synthesis of high-silica zeolite starting from a highly concentrated silicate solution was examined. There has been an unexplored area between conventional hydrothermal synthesis and the dry-gel conversion technique using dry-gel. As a result, the novel zeolite YNU-5 (**YFI**), which has a 12-12-8-ring pore system and isolated 8-ring straight channels, was successfully synthesized. The OSDA employed was dimethyldipropylammonium, one of the simplest tetraalkylammonium compounds. Even though YNU-5 has a large cavity at the intersection of two 12-ring channels, it crystallizes in the presence of such a simple OSDA. The use of concentrated silicate solution may have caused efficient interaction between silicate species and organic species.

Although several competing phases such as mordenite (**MOR**), ZSM-5 (**MFI**) and beta (***BEA**) were observed during the investigation, YNU-5 (**YFI**) was obtained as a pure form within a narrow synthesis window. The SiO_2/H_2O molar ratio in the synthesis mixture strongly influenced the framework density of the product phase. Controlled dealumination for tuning of the Si/Al ratio in the range from 9 to >200 by acid-treatment was also possible. The thermal stability of the **YFI** framework was low when dealumination was conducted under milder conditions, whereas the framework was well-stabilized under severer acid-treatment conditions. Tunable Si/Al ratios and framework stabilization are important factors for the utilization of YNU-5 as a solid acid catalyst.

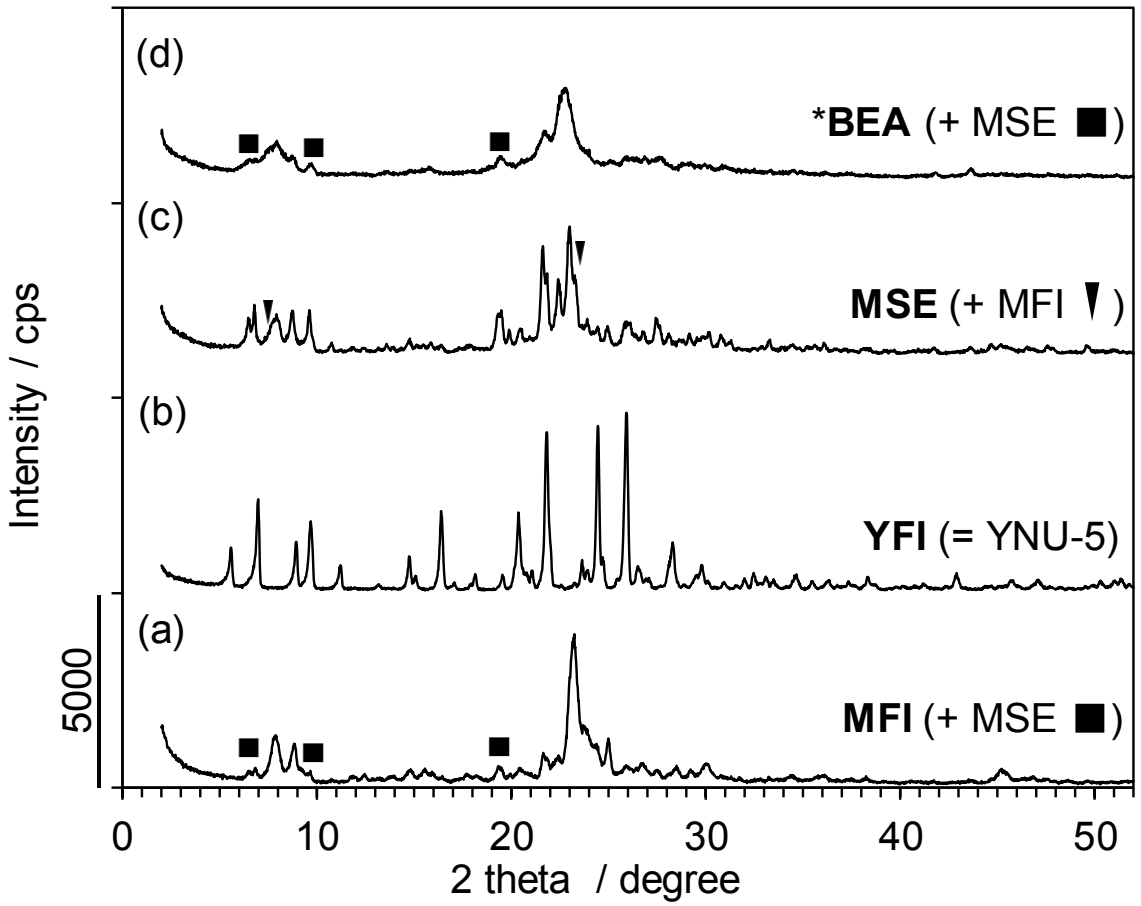

Figure 5.1 Powder XRD patterns of as-synthesized samples crystallized under the conditions with (a) $x = 10$, (b) $x = 7$, (c) $x = 4$, and (d) $x = 3$, where x is H_2O/SiO_2 molar ratio. Hydrothermal synthesis was performed in a 20 mmol SiO_2 scale using a 23 mLTeflon-lined stailess-steel autoclave at 160°C. Starting molar composition is 0.265 $(SiO_2)_{FAU}$−0.735 $(SiO_2)_{Ludox}$−0.025 $(Al_2O_3)_{FAU}$−0.17 Q^+OH^- −0.15 NaOH−0.15 KOH−x H_2O, where $(SiO_2)_{FAU}$ and $(SiO_2)_{Ludox}$ indicate silica coming from **FAU**-type zeolite and colloidal silica, respectively. Crystallization times are (a) 7 d, (b) 7 d, (c) 3 d, and (d) 3 d, respectively.

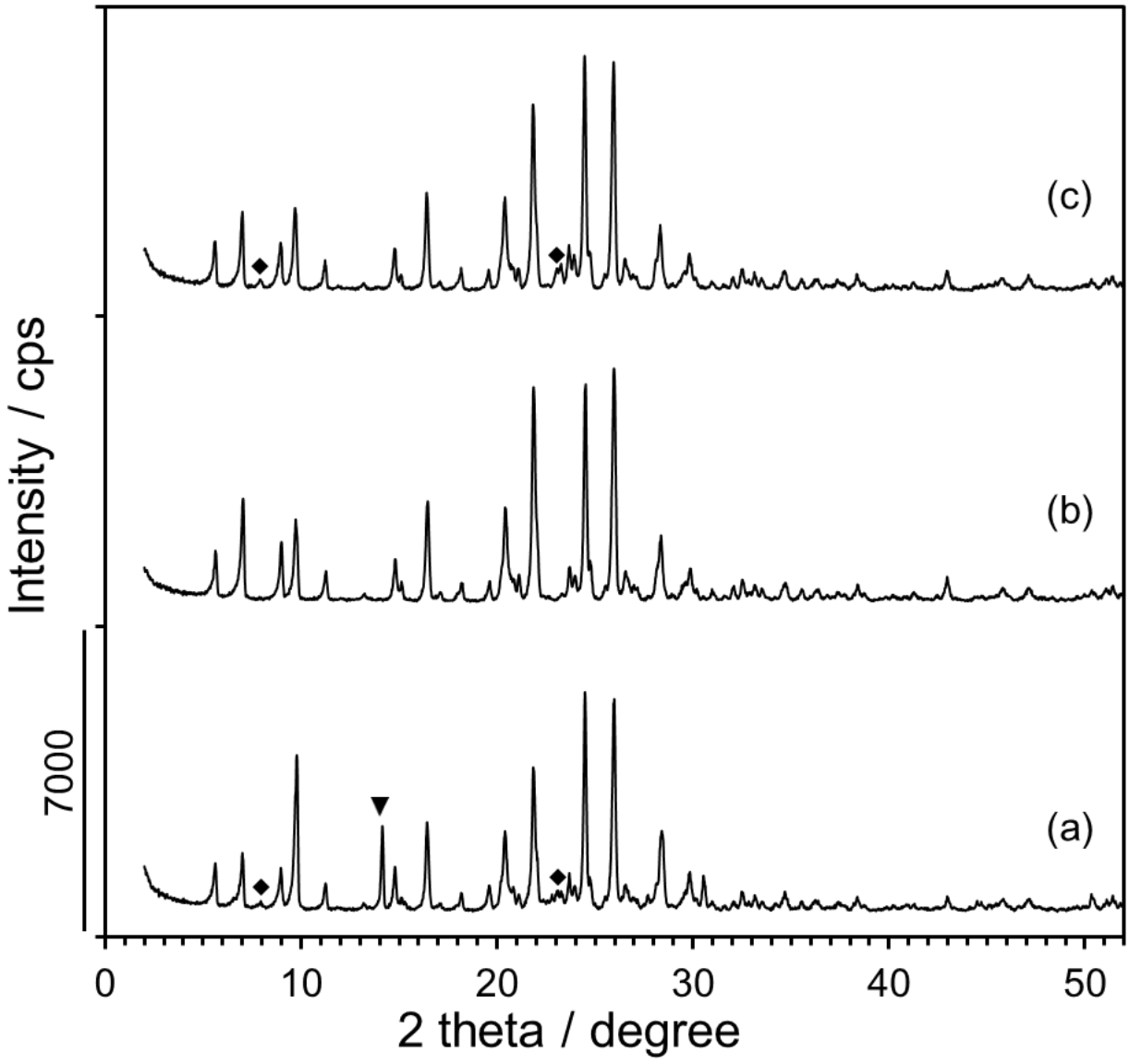

Figure 5.2 Powder XRD patterns of as-synthesized samples synthesized under the conditions with H_2O/SiO_2 molar ratios (a) 6, (b) 7 and (c) 8, respectively. Diamond symbols refer to **MFI** phase and triangle symbol refer to unknown impurity.

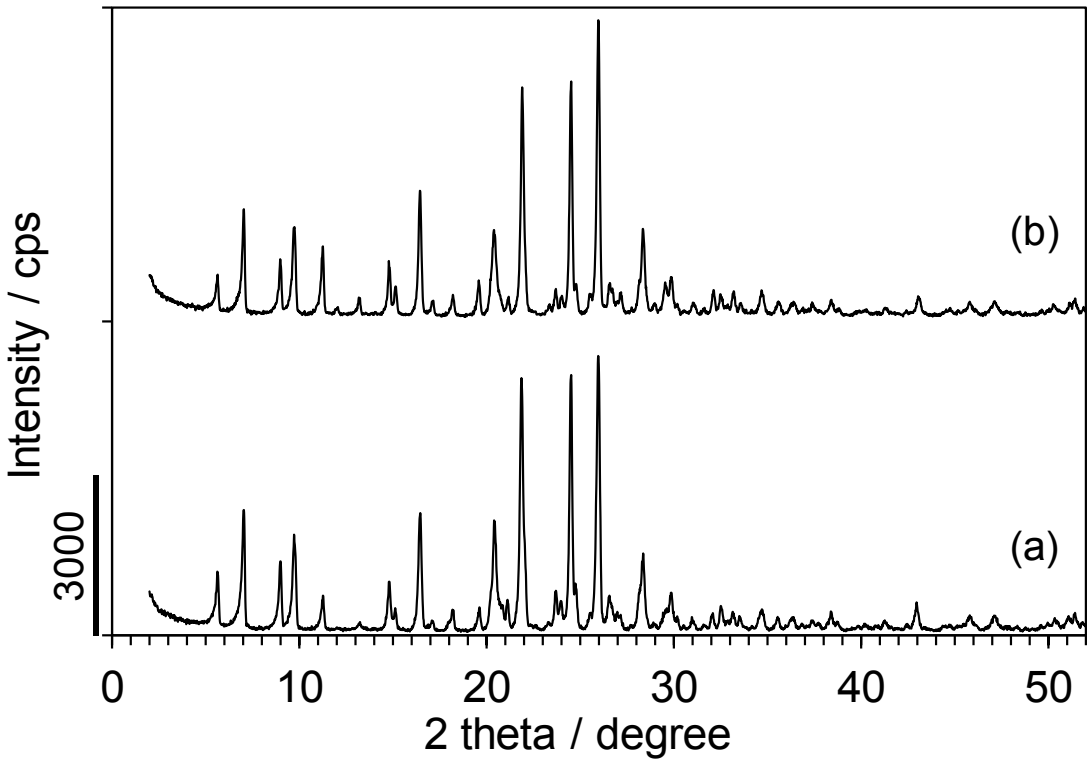

Figure 5.3 Powder XRD patterns of (a) as-synthesized and (b) calcined YNU-5 zeolites

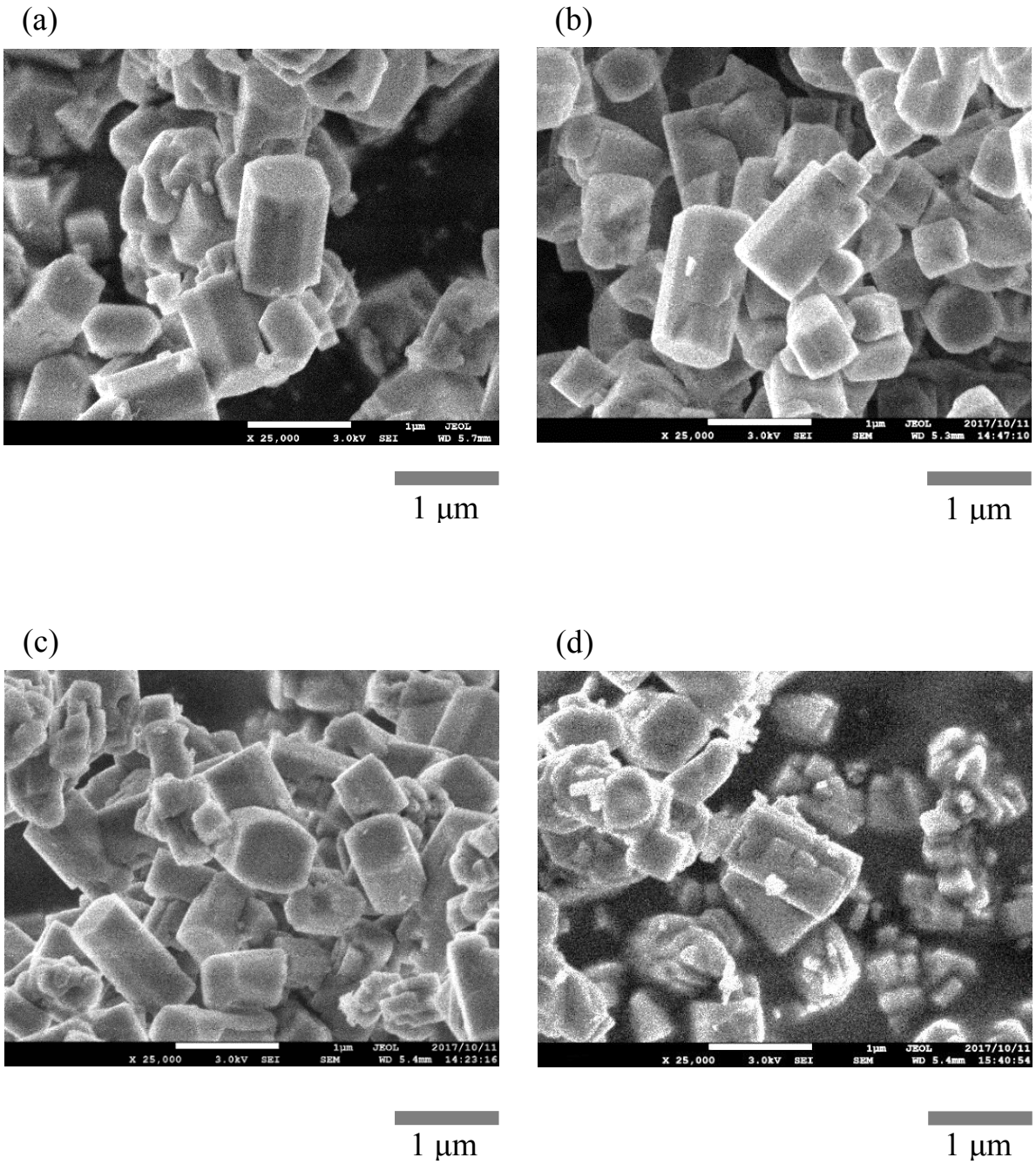

Figure 5.4　FE-SEM images showing the effect of synthetic conditions on the crystal size and morphology. The representative image of the product obtained by heating for (a) 4 d without rotation, (b) 7 d without rotation, (c) 4 d with rotation at 20 rpm, and (d) 7 d with rotation at 20 rpm.

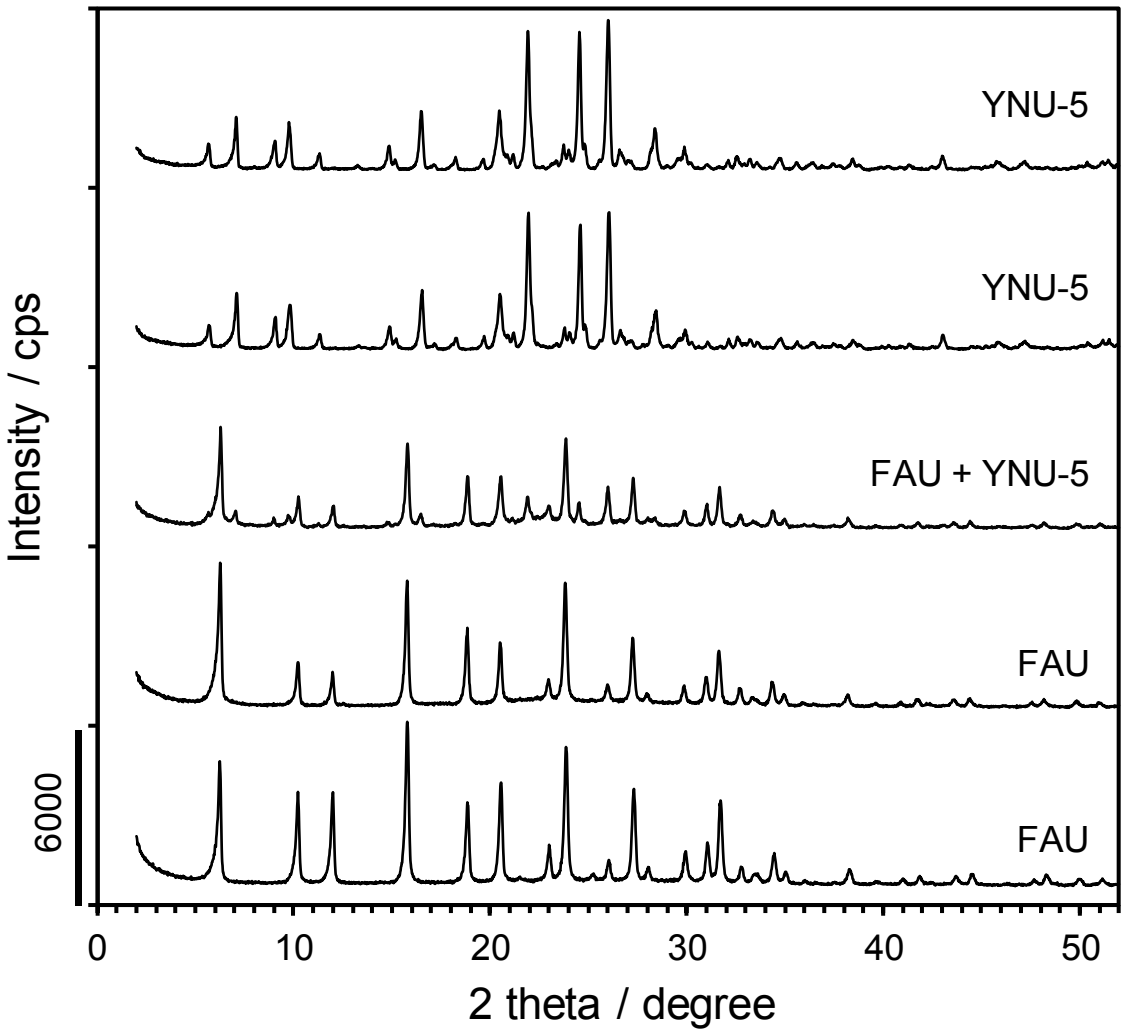

Figure 5.5 Time-course of crystallization of YNU-5 (**YFI**) starting from **FAU**-type zeolite as a starting material. Powder XRD patterns of (a) starting **FAU** and recovered solid after heating for (b) 16 h, (c) 28 h, (d) 45 h, and (e) 165 h.

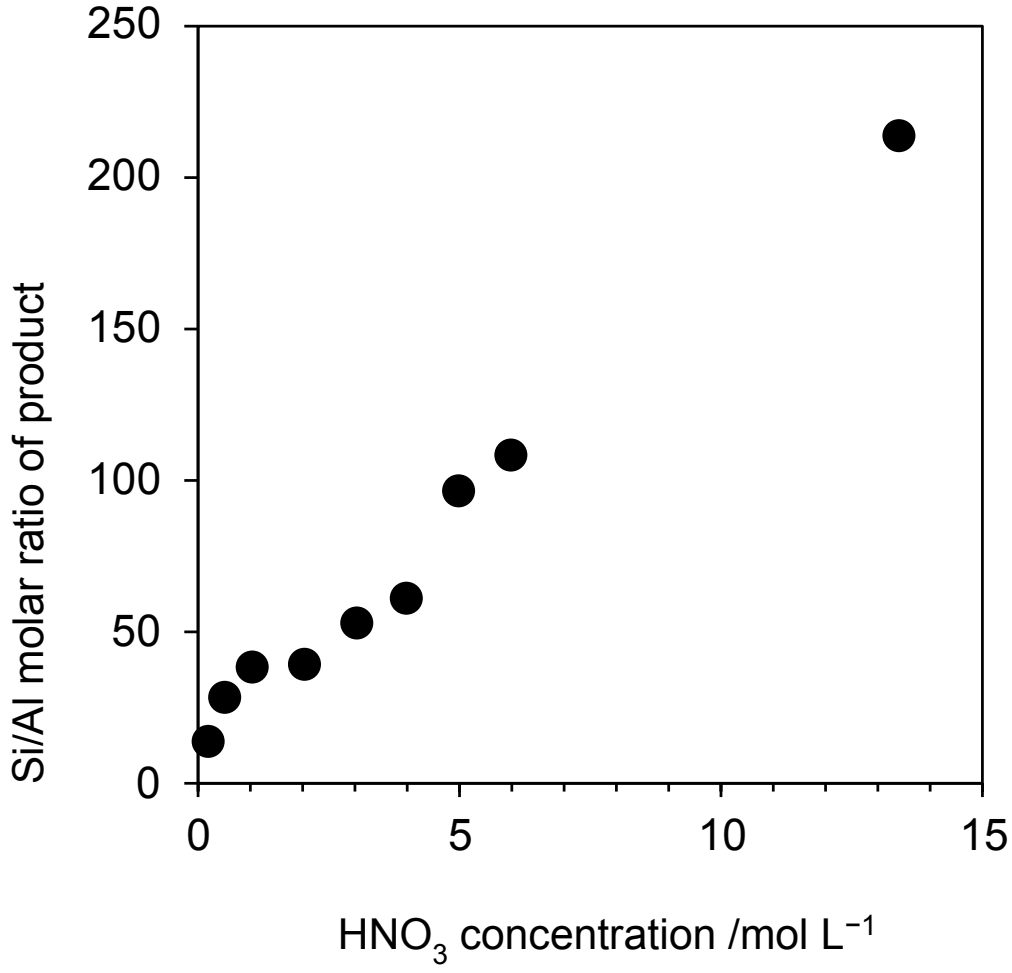

Figure 5.6 Relationship between concentration of nitric acid used for acid treatment of calcined YNU-5 (Si/Al = 9) at 80 °C for 2 h and the Si/Al molar ratio of the product determined by ICP analysis.

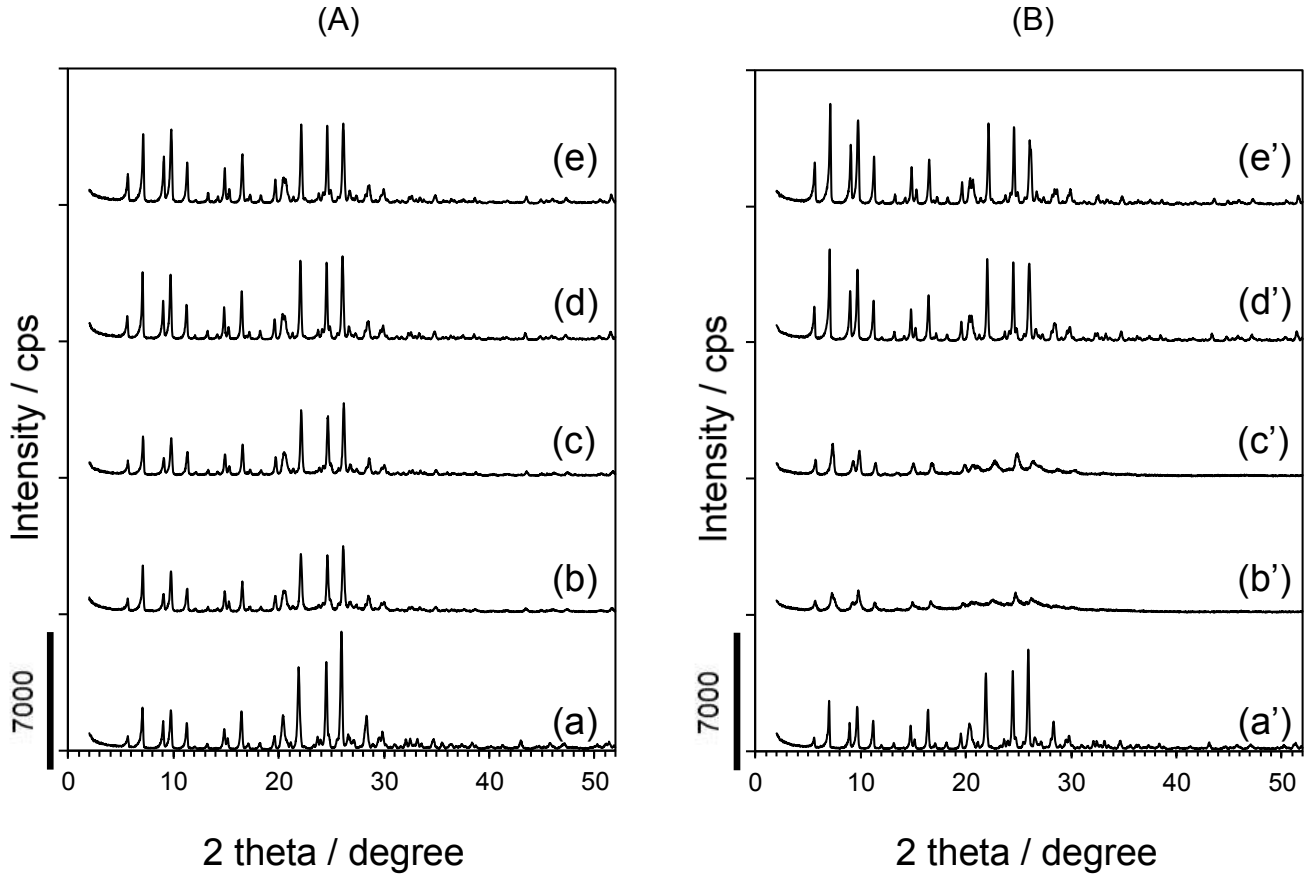

Figure 5.7 Powder XRD patterns of (a, a') NH_4^+-YNU-5 with Si/Al = 9, (b, b') dealuminated YNU-5 with Si/Al = 39 treated at 80 °C for 2 h using 2 mol/L HNO_3 solution, (c, c') dealuminated YNU-5 with Si/Al = 60 treated at 80 °C for 2 h using 3 mol/L HNO_3 solution, (d, d') dealuminated YNU-5 with Si/Al = 57 treated under reflux conditions for 24 h using 2 mol/L HNO_3 solution, (e, e') dealuminated YNU-5 with Si/Al = 350 treated under reflux conditions for 24 h using 13.4 mol/L HNO_3 solution (A) before and (B) after thermal treatment at 650 °C for 1 h.

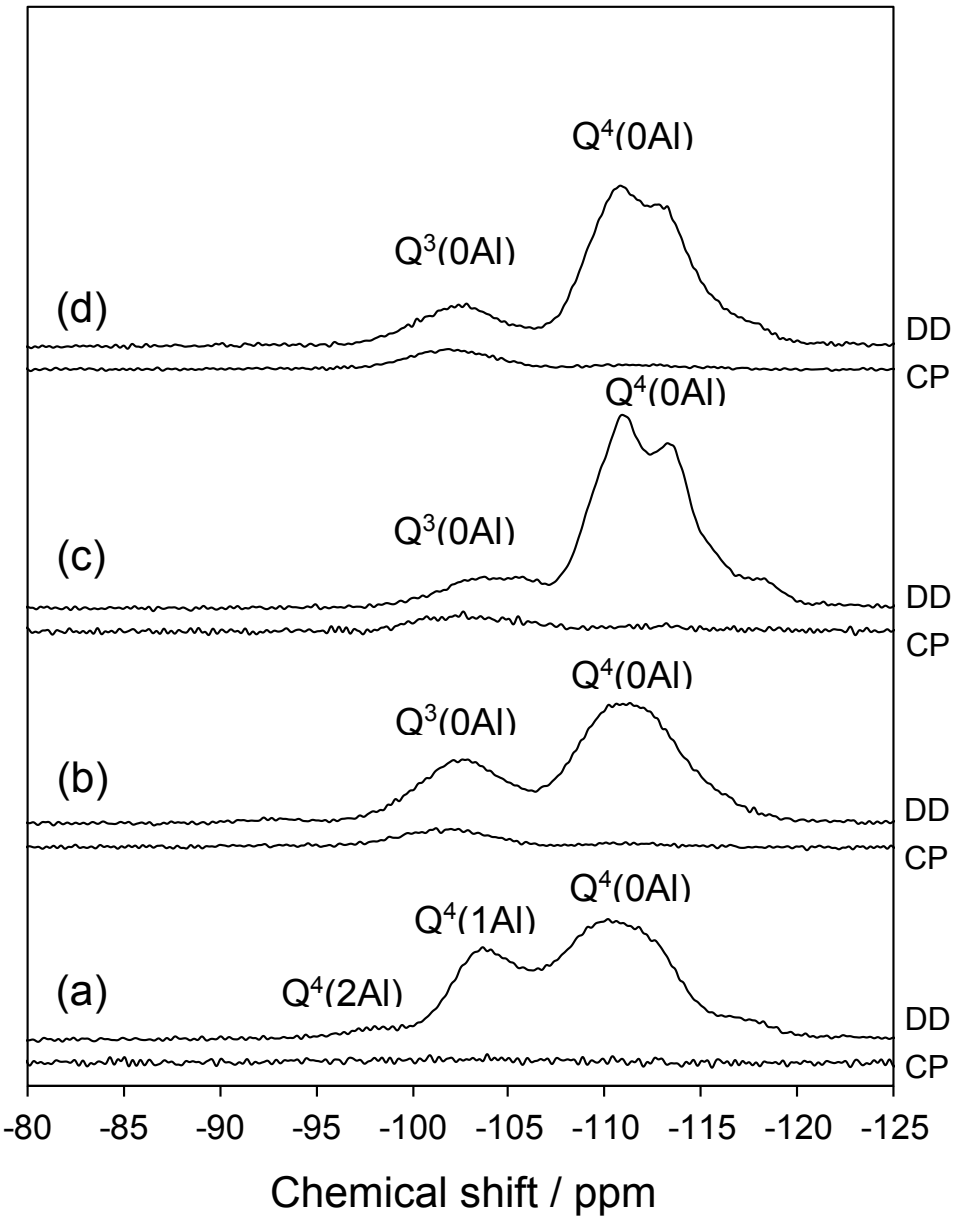

Figure 5.8 ^{29}Si MAS NMR spectra of (a) calcined YNU-5 before dealumination (Si/Al = 9) and dealuminated samples treated with (b) 2 mol/L HNO_3 solution at 80 °C for 2 h (Si/Al = 39), (c) 2 mol/L HNO_3 solution under reflux conditions for 24 h (Si/Al = 57), and (d) 13.4 mol/L HNO_3 solution under reflux conditions for 24 h (Si/Al = 350). DD and CP indicate dipolar-decoupling and cross polarization, respectively.

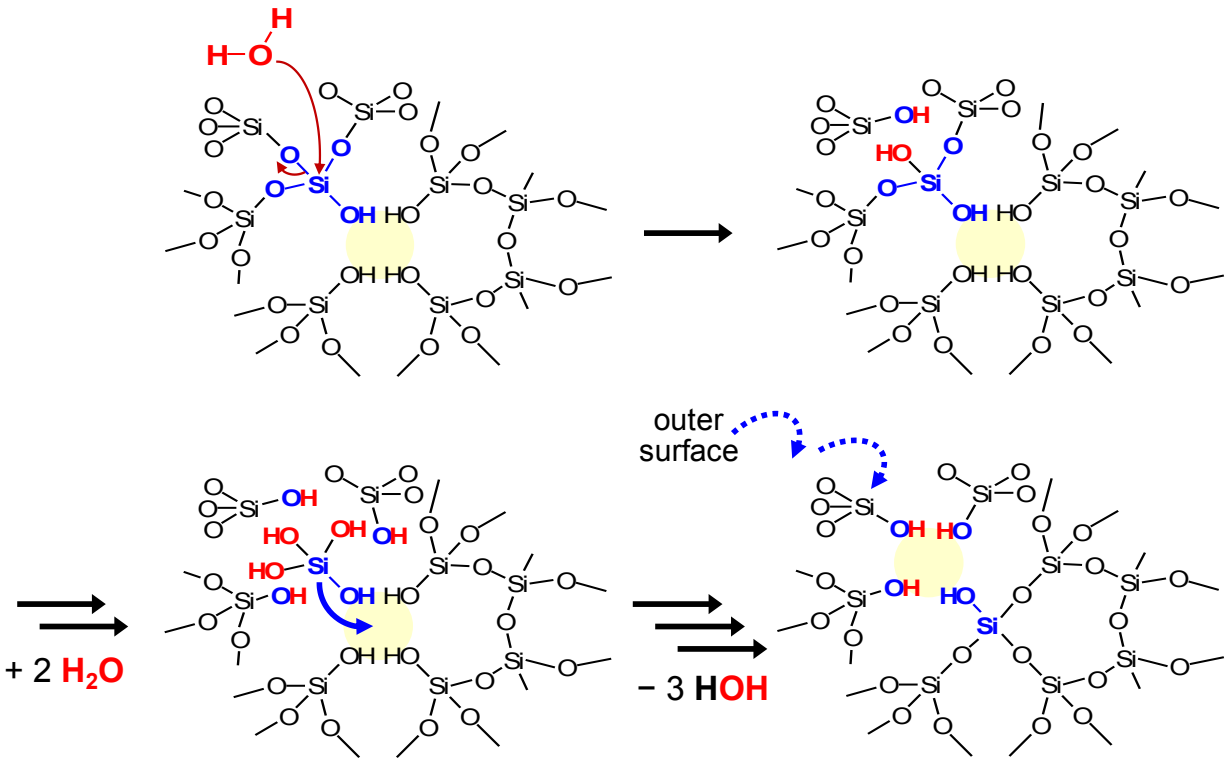

Figure 5.9 Mechanistic speculation of Si-migration in molecular level.

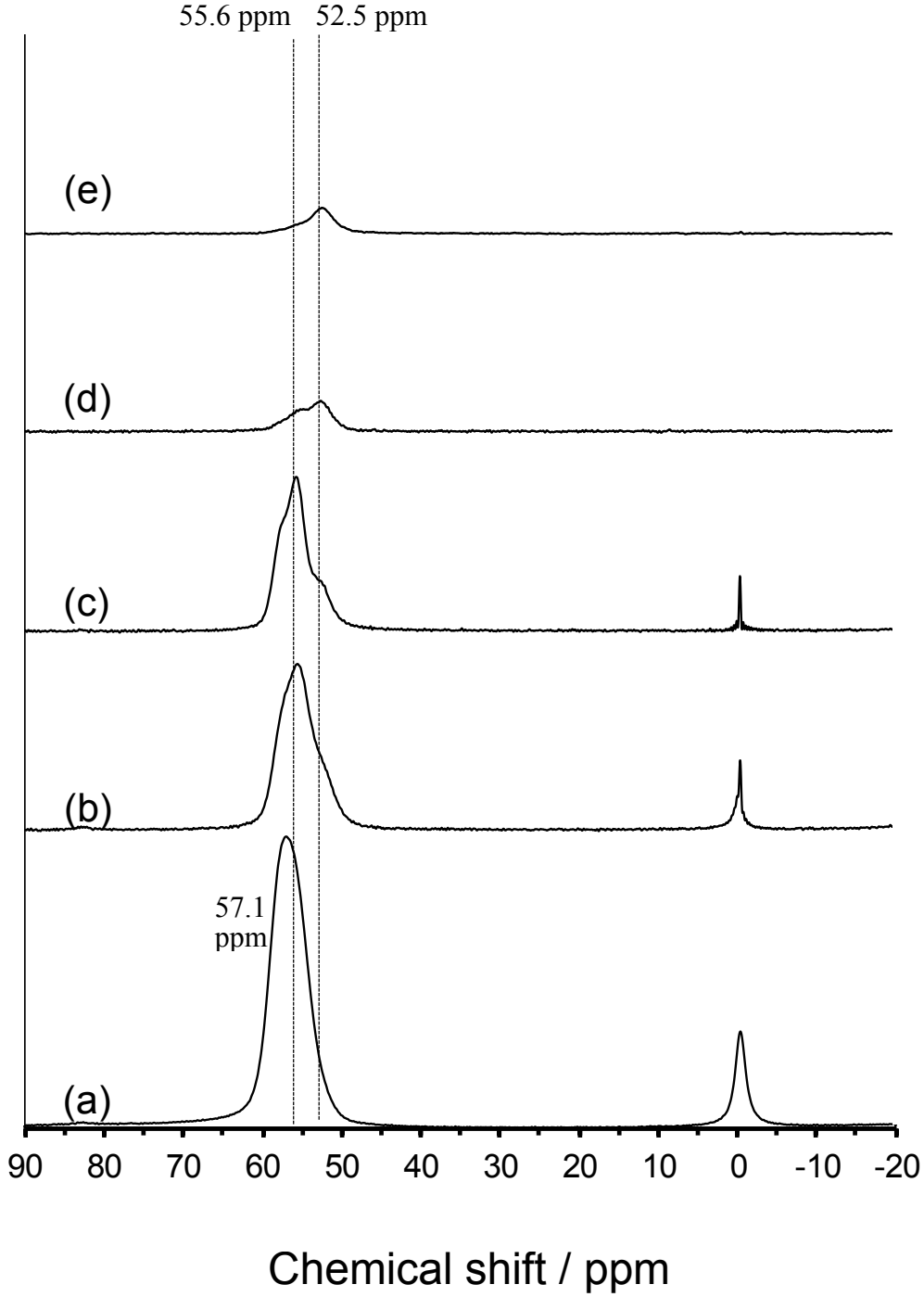

Figure 5.10 ^{27}Al DE MAS NMR spectra of (a) calcined YNU-5 before dealumination (Si/Al = 9) and dealuminated samples treated with (b) 2 mol/L HNO_3 solution at 80 °C for 2 h (Si/Al = 39), (c) 2 mol/L HNO_3 solution under reflux conditions for 24 h (Si/Al = 57), (d) 13.4 mol/L HNO_3 solution under reflux conditions for 24 h (Si/Al = 350), and (d) 13.4 mol/L HNO_3 solution under reflux conditions for 24 h (Si/Al = 304). Y-axis of spectrum (a) is contracted to 1/2 of original one. The shoulder peak at 54.8 ppm on the spectrum (d) is due to very minor impurity and it does not appear on the spectrum of highly pure sample (e).

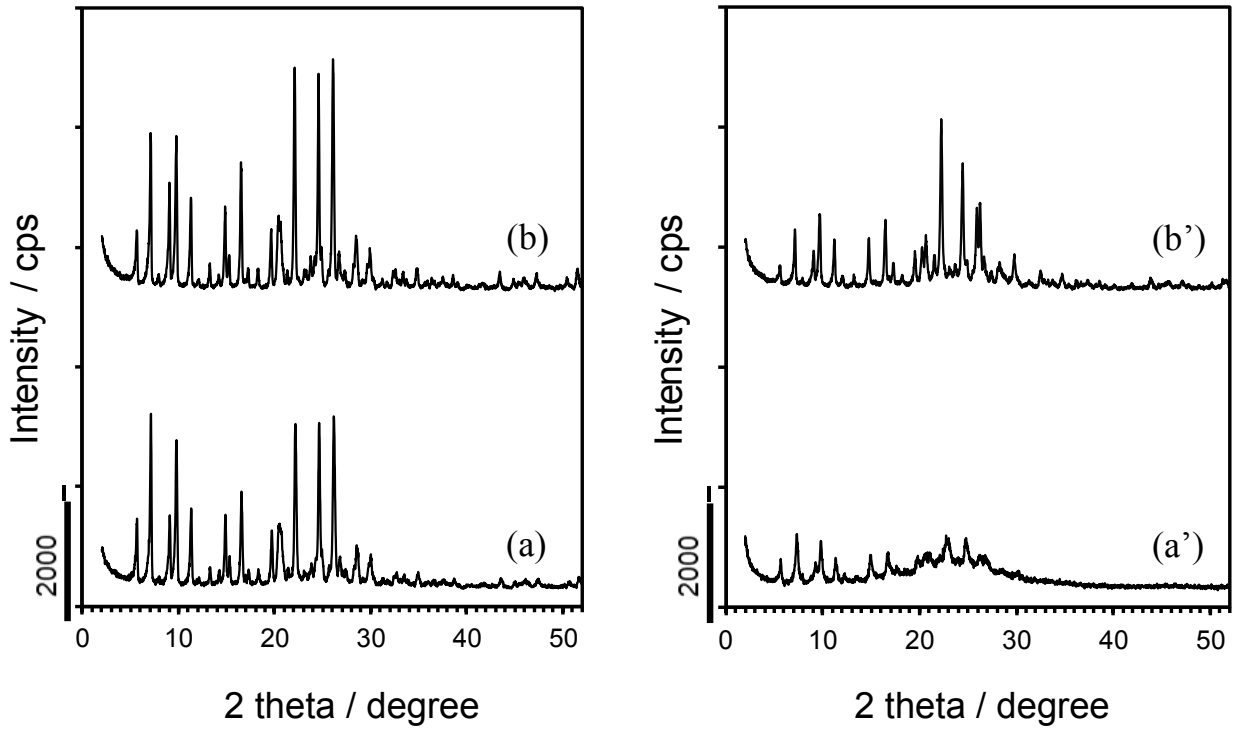

Figure 5.11 Powder XRD patterns of the (a) unstabilized and (b) stabilized catalysts (a, b) before and (a', b') after reaction indicating the significant effect of the framework stabilization.

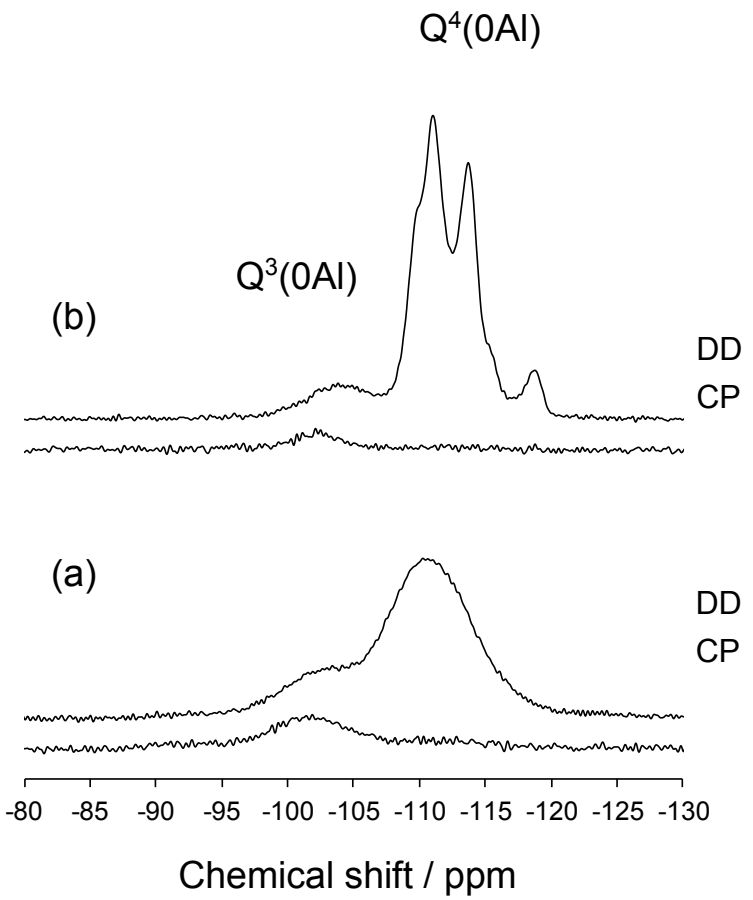

Figure 5.12 ^{29}Si MAS NMR spectra of dealuminated YNU-5 treated with (a) 3 mol/L HNO_3 solution at 80 °C for 2 h (Si/Al = 60, unstabilized) and (b) 2 mol/L HNO_3 solution under reflux conditions for 24 h (Si/Al = 57, stabilized). DD and CP indicate dipolar-decoupling and cross polarization, respectively.

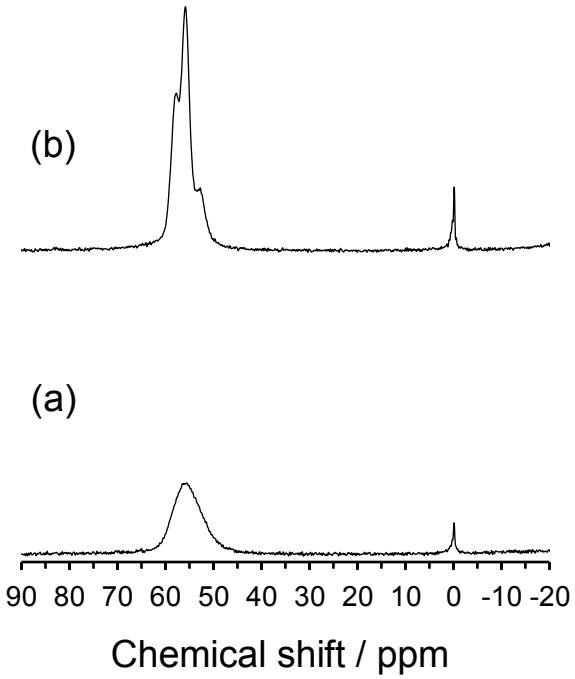

Figure 5.13 ^{27}Al DE MAS NMR spectra of dealuminated YNU-5 treated with (a) 3 mol/L HNO_3 solution at 80 °C for 2 h (Si/Al = 60, unstabilized) and (b) 2 mol/L HNO_3 solution under reflux conditions for 24 h (Si/Al = 57, stabilized).

5.6 References

1) M.E. Davis, *Catal. Today*, **19**, 1 (1994).

2) P. Wagner, M. Yoshikawa, M. Lovallo, K. Tsuji, M. Tsapatsis, M.E. Davis, *Chem. Commun.* 2179 (1997).

3) Y. Kubota, M.M. Helmkamp, S.I. Zones, M.E. Davis, *Micropor. Mater.*, **6**, 213 (1996).

4) P. Wagner,Y. Nakagawa,G.S. Lee, M.E. Davis,S. Elomari,R.C. Medrud, S.I. Zones, *J. Am. Chem. Soc.*, **122**, 263 (2000).

5) M. Moliner, C. Franch, E. Palomares,M. Grill, A. Corma, *Chem. Commun.*, **48**, 8264 (2012).

6) R.F. Lobo, S.I. Zones, R.C. Medrud, *Chem. Mater.*, **8**, 2409 (1996).

7) D.W. Fickel, E. D'Addio, J.A. Lauterbach, R.F. Lobo, *Appl. Catal. B: Environ.*, **102**, 441 (2011).

8) T. Shibata, S. Suzuki, H. Kawagoe, K. Komura, Y. Kubota,Y. Sugi, J.-H. Kim, G. Seo, *Micropor. Mesopor. Mater.*, **116**, 216 (2008).

9) N. Nakazawa, S. Inagaki, Y. Kubota, *Chem. Lett.*, **45**, 919 (2016).

10) Y. Sun, W. Lu, Y. Li, *Appl. Phys. Lett*., **105** (2014).

11) W. J. Roth, P. Nachtigall, R. E. Morris, J. Čejka, *Chem. Rev.*, **114**, 4807 (2014).

12) Ch. Baerlocher, L.B. McCusker, D.H. Olson, Atlas of Zeolite Framework Types, 6th ed., Elsevier, Amsterdam (2007); see also: http://www.iza-structure.org/databases/.

13) T. Ikeda, S. Inagaki, T. Hanaoka, Y. Kubota, *J. Phys. Chem. C*, **114**, 19641 (2010).

14) Y. Kubota, K. Itabashi, S. Inagaki, Y. Nishita, R. Komatsu, Y. Tsuboi, S. Shinoda, T. Okubo, *Chem. Mater.*, **26**, 1250 (2014).

15) J. Klinowski, J.M. Thomas, C.A. Fyfe, G.C. Gobbi, Nature **296**, 533 (1982).

Conclusions

In this work, novel zeolites with ***STO**, **AEI**, **GME**, **AFX** and **YFI** topologies have been successfully synthesized by using zeolites as starting materials or precursors. Novel ***STO**-type zeolites are given by pure-silica beta seed crystals. Only 5wt% seeding enabled the whole crystallization processes. Seed crystals significantly assisted the nucleation which is the rate determining step for the crystallization. The high-silica **AEI**-type zeolite (SSZ-39) is synthesized from **FAU**-type zeolite in addition to colloidal silica. This work shows the possibility to obtained novel zeolites from known OSDAs by careful tuning of other inorganic components influencing on syntheses. A novel fault-free **GME**-type zeolite is also obtained from **FAU** crystals. The novel **AFX**-type zeolite with medium Al contents is synthesized from **FAU**-type zeolites and is highly desired since it has excellent hydrothermal stability and ion-exchange capacity, especially in terms of application for NOx SCR. The **YFI**-type zeolite is especially noteworthy because **YFI** is a new framework code. The first novel zeolite, YNU-5, can be synthesized using $Me_2Pr_2N^+$ which is an inexpensive and feasible OSDA. It is surprising that there has been a remaining new zeolite synthesized by simple tetraalkylammonium. Since the famous industrially important **MFI** and ***BEA**-type zeolites are synthesized by tetrapropylammonium and tetraethylammonium respectively, **YFI** zeolites should possess industrial feasibity.

Although the crystallization kinetic is still unclear, it can be said that the crystallization process is clearly reflected in the structural similarities between starting materials and products. Dissolving aluminosilicate species occur near precursor crystals probably play a significant role on nucleation stage and/or strongly assist to construct crystal nuclei.